NJ-2016-002-2

Design and Fabrication of Orthotropic Deck Details

FINAL REPORT
Vol. II
February 2016

Submitted by

Sougata Roy, Ph.D.
Former Principal Research Scientist
ATLSS Center
Lehigh University

Soham Mukherjee
Former Research Assistant
ATLSS Center
Lehigh University

NJDOT Research Project Manager
Ms. Priscilla Ukpah

In cooperation with

New Jersey
Department of Transportation
Bureau of Research

DISCLAIMER

“The contents of this report reflect the views of the authors who are responsible for the facts and the accuracy of the data presented herein. The contents do not necessarily reflect the official views or policies of the New Jersey Department of Transportation. This report does not constitute a standard, specification, or regulation. “

TECHNICAL REPORT
STANDARD TITLE PAGE

1. Report No. NJ-2016-002-2	2.Government Accession No.	3. Recipient's Catalog No.
4. Design and Fabrication of Orthotropic Deck Details FINAL REPORT Vol. II of VII Volumes		5. Report Date February 2016 6. Performing Organization Code
7. Author(s) Roy, Sougata Ph.D. and Soham Mukherjee		8. Performing Organization Report No.
9. Performing Organization Name and Address Advanced Technology for Large Structural Systems (ATLSS) Engineering Research Center, Lehigh University 117 ATLSS Drive Bethlehem, PA 18015		10. Work Unit No. 11. Contract or Grant No.
12. Sponsoring Agency Name and Address New Jersey Department of Transportation PO 600 Trenton, NJ 08625		13. Type of Report and Period Covered 14. Sponsoring Agency Code

15. Supplementary Notes
Volume 2 has 111 pages. All seven volumes total 804 pages.

16. Abstract
The objectives of the research were to verify the design and fabrication of the orthotropic deck details proposed for the lift bridge, for infinite fatigue life. Multi-level 3D finite element analyses (FEA) of the proposed deck were performed to determine the critical stresses at the connections, the corresponding load position, and the deck specimen. To develop cost-effective connection details, three variations of rib-to-floor beam and rib-to-deck plate connection details, including the influence of different fabrication parameters, were explored in full-scale small size mockups. Subsequently, the infinite life fatigue performance of the connection details were evaluated by laboratory testing of a full-scale prototype. The fatigue testing was conducted under simulated rear tandem axle loading of the AASHTO fatigue truck with adequate boundary condition. The prototype testing was runout after 8 million cycles, verifying the infinite life fatigue performance of the deck design.

17. Key Words	18. Distribution Statement
Lift Span, Orthotropic Deck, Rounded Bottom Ribs, Infinite Fatigue Life, Full-Scale Prototype, Fatigue Testing, AASHTO, Run-Out, Cost-Effective, Fabrication.	

19. Security Classif (of this report)	20. Security Classif. (of this page)	21. No of Pages	22. Price
Unclassified	Unclassified	111	

Form DOT F 1700.7 (8-69)

ACKNOWLEDGEMENTS

The authors wish to acknowledge the efforts of the New Jersey Department of Transportation (NJDOT) including the Project Manager Ms. Priscilla Ukpah and Ms. Camille Crichton-Sumners, Manager of the Bureau of Research. The authors thank the Research Selection and Implementation Panel members that included the following NJDOT employees: Ms. Xiaohua Hannah Cheng, Mr. Eddy Germain, Mr. Fred Lovett, Mr. Mahesh Patel, Mr. David Lambert, Mr. Nat Kasbekar, Mr. Eric Kraehenbuehl, Mr. Jayant Dalal, Mr. Vijaykumar Thaker, Ms. Kiranben Patel and Mr. Javier Estradal. These individuals offered valuable comments and suggestions on the research project resulting in an improved product.

Editing of the final report was performed by Dr. Richard Sause, Director of the ATLSS Center.

The research was performed with the assistance of Mr. Xudong Zhao, Mr. Philipp Keller, Mr. Frank Artmont, Mr. Yeun Chul Park and Mr. Juan Tzoc, and the support staff of ATLSS Engineering Research Center and Fritz Engineering Laboratory for their help with successful execution of the project.

The authors would also like to specially thank Mr. Ronnie Medlock, Vice President of Technical Services of High Steel Structures for valuable input on fabrication of this deck and to Dr. John W. Fisher for sharing his vast experience regarding orthotropic decks.

CONTENTS (VOLUME I)

CONTENTS (VOLUME II)

CONTENTS (VOLUME III)

CONTENTS (VOLUME IV)

CONTENTS (VOLUME V)

CONTENTS (VOLUME VI)

CONTENTS (VOLUME VII)

LIST OF FIGURES (VOLUME II)

LIST OF TABLES (VOLUME II)

4. EVALUATION OF MOCKUP TEST RESULTS

The activities undertaken under Task 4 of the research project related to the evaluation of the mockup test results are reported in this chapter. Two types of tests were conducted on the mockup specimens: static tests and fatigue tests. The static tests results showed a good correlation with the FEA and verified the accuracy of the FE model. The static test results also provided stresses at the critical locations and helped in assessing the change in state of the specimens with the gradual progression of the fatigue test. The fatigue tests revealed a unique failure mode of the rib-to-floor beam connection in all the specimens, where fatigue cracks initiated from the LOF at the weld root and propagated in the floor beam web and rib wall at planes normal to the principal stress direction. No fatigue damage was observed at any of the other welded connections in any of the specimens.

4.1 Static Test Results

Prior to initiating fatigue tests, static tests were conducted on each mockup specimen by using Amsler pulsators and actuators, to determine the stresses at the gauge locations. The results of the static tests were compared with the analytical prediction and then the dynamic load ranges and the stress limits at the control gauges were determined from that. Three static tests were conducted on each specimen to shakedown the residual stress effects and to determine the repeatability of the tests. Static tests were conducted on MU1 on October 17, 2012 for load ranges of 58.2 kip, 27.9 kip and 28.4 kip at the middle, the east and the west actuators respectively. Static tests were conducted on MU2 on November 7, 2012 for load ranges of 59.5 kip, 28.5 kip and 28.9 kip at the middle, the east and the west actuators respectively. Static tests were conducted on MU3 on November 15, 2012 for load ranges of 58.4 kip, 27.9 kip and 28.5 kip at the middle, the east and the west actuators respectively.

During fatigue testing, intermittent static tests were performed after holes were drilled to arrest the growth of any fatigue crack which was reported, to evaluate the change in the state of the structure. For MU1, static tests were conducted on October 24, 2012 after fatigue crack was reported at the rib-to-floor beam connection to the south side of the rib. Later on, static tests were conducted on October 26, 2012 after fatigue crack was reported at the rib-to-floor beam connection to the north side of the rib. For MU2, static tests were conducted on November 13, 2012 after fatigue cracks were reported at the rib-to-floor beam connection to the north and the south sides of the rib. For MU3, static tests were conducted on November 19, 2012 after fatigue crack was reported at the rib-to-floor beam connection to the south side of the rib. Later on, static tests were conducted on November 21, 2012 after the crack on the south side propagated through the hole and appeared from the edge of the drilled hole.

During the static tests 54 uni-axial gauges of ¼ in. gauge length, 34 uni-axial gauges of 1 mm gauge length, 4 strip gauges with 5 elements of 1 mm gauge length, 4 rosette, 3 load cells and 1 LVDT were installed, involving a total of 124 data channels. All measurements were conducted within the nominal elastic range of the material. The strains measured at the gauges were converted to stresses by multiplying with the

universally accepted modulus of elasticity for steel of 29,000 ksi ($2x10^5$ MPa). For the rosette gauges, the strains measured at the rosette arms were used to determine the principal and the directional stresses at the rosette location. The results of the static tests are provided as Appendix A, contained in Volume VII.

4.1.1 Global Response of the Prototype Deck

The global response of the prototype deck is discussed in this section in terms of the measurements at strain gauges on the top and the underside of the deck plate, the floor beam and beam fixture flanges and the displacement measurement at the LVDT. These gauges were away from the load pads and the effect of the localized behavior of the deck elements was insignificant. Gauges on the top of the deck plate were oriented in the transverse direction while gauges on the soffit of the rib were oriented in the longitudinal direction of the deck. Gauges on the floor beam and beam fixture flanges (recall beam fixture provided the continuity for floor beam) were oriented in the transverse direction of the deck. The gauges are identified in the following sections and the detail location of the gauges can be obtained from section 3.6.3, contained in Volume I.

The static test results are presented as plots of strain gauge or LVDT measurements against the applied static loads. Results are plotted both for the loading and the unloading phases during the static tests to check the linearity of the data and the presence of residual stresses if any. The measured quantities (stresses or displacements) are presented on the Y-axis as ordinate and the applied load in the middle actuator along the X-axis as the abscissa. The location of strain gauges and the direction of stresses are shown as inset in each figure. The downward displacements measured at the LVDT are presented as –ve, and the tensile stresses measured at the stain gauges are presented as +ve. The FEA result is marked as a red dot on the plots since FEA was done only for the maximum load levels.

Response of Deck Plate and Rib

The global response of the deck and the rib is discussed in respect of the measurements at the strain gauges TDP_WEB_Avg installed on the deck plate along the centerline of the floor beam near the splice connection with the beam fixture flange, (E/W)TDP_3 installed on the top of deck plate in between the load pads and oriented along the centerline of the east and the west loading pads respectively and (E/W)R_0_3 installed on the soffit of the rib along the 0° line where the degree is measured from the centerline of the rib soffit. The gauges on the soffit of the rib were significantly away from the rib-to-floor beam connection and stress measured at the gauges were unaffected by the local behavior of the connection.

The measurements at some of the gauges for the three trials are plotted in Figure 116 to Figure 118 with FEA results shown as red dots. It is evident from the plots that the results of the static tests for each specimen were repeatable, and were generally linear elastic and agreed well with the FEA results. There were almost no residual stresses at the gauges for MU-1. However for MU-3 there were about 0.6 ksi residual stresses at

(E/W)R_0_3_Avg at the end of first static trial which was later eliminated by subsequent trials.

The measurements of the three specimens are compared in the Figures 119 and 120. The results for the three specimens match well for most of the gauges indicating the same global behavior of the deck in all specimens as it was expected. Tensile stress was recorded at TDP_WEB_Avg for all the specimens as the deck experienced global tensile and compressive stresses at the top and bottom due to flexural deformation in the transverse direction. The stresses measured at the gauges on the soffit of the rib were compressive which indicated the cantilever bending of the rib in the longitudinal direction and the gauges were unaffected from the local behavior of the rib-to-floor beam connection. The measured stresses at WR_0_3_Avg were slightly higher than that at ER_0_3_Avg because the load applied by the west actuator was slight greater than the load applied by the east actuator. However this difference was within the range of the acceptable variability of manual application of load and since this difference was so small that it did not contribute to the variation in fatigue performance of the specimens.

The measurements at the gauges during the static test at the onset of fatigue testing and the last static test on the cracked specimen are plotted in Figures 121 and 122. No significant change in stresses was noted at these gauges, indicating that no significant change occurred in the global response of the deck. The effects of fatigue cracking were local, and did not influence the global response characteristics of the deck.

Response of Floor Beam

The global response of the floor beam is discussed in respect of the measurements at the strain gauges BDP_WEB_Avg installed on the bottom flange near the splice connection with the beam fixture flange, TF_1_Avg & BF_1_Avg installed on the top and bottom flanges of the beam fixture respectively near the connection with Column A and TF_2_Avg & BF_2_Avg installed on the top and bottom flanges of the beam fixture respectively, near the connection with Column B. The gauges were oriented in the transverse direction of the deck and aligned along the centerline of the floor beam. A LVDT channel (DISPL_Avg) was also provided at the tip of floor beam web plate to measure the global displacement.

The measurements at the LVDT for the three trials for each specimen are plotted in Figures 123 to 125 with FEA results shown as red dots. The measured displacements in the three specimens were higher than the FEA result. One of the reasons for this deviation between the analytical and the experimental results could be that the connection between Column B and beam fixture was not modelled in detail during FEA and in doing so the fact that Column B was very flexible as compared to the beam was ignored. So the rotation of the beam at the connection was less than the actual rotation of the specimen which caused reduced displacement in the FEA model. In addition, FE models are generally more rigid than the actual specimen. The measurements at some of the gauges for three trials for each specimen are plotted in Figure 126 to Figure 128 with FEA results shown as red dots. It is evident from the plots that the results of the

static tests for each specimen were repeatable, and were generally linear elastic and agreed well with the FEA results, except for BF_1_Avg. The stress measured at channel BF_1_Avg was less than the FEA value. One of the reasons for this deviation could be the difference in locations of the proposed and as-installed gauge. But these deviations didn't affect the local behavior at the fatigue sensitive locations. There were almost no residual stresses at the gauges.

The measurements of the three specimens are compared in the Figures 129 to 131. The results for the three specimens match well indicating the same global behavior of the deck in all specimens as it was expected. Stresses were tensile on the top flange and compressive on the bottom flange as the floor beam experienced global tensile and compressive stresses at the top and bottom flanges due to flexural deformation in the transverse direction. The magnitude of the tensile stress at TDP_WEB_Avg was less than the magnitude of the compressive stress at the BDP_WEB_Avg due to the composite action of the deck plate and the floor beam. Since the load pads were significantly away from these gauges, these gauges did not experience any local deformation. The maximum displacement matched well for the three specimens and was about 0.21 in. (Figure 129).

The measurements at the gauges measured during the static test at the onset of fatigue testing and the last static test on the cracked specimen are plotted in Figures 132 to 134. No significant change in stresses was noted at these gauges, indicating that no significant change occurred in the global response of the deck. The effects of fatigue cracking were local, and did not influence the global response characteristics of the deck.

4.1.2 Response of the Floor Beam-to-Deck Plate Connection

Response of floor beam-to-deck plate connection is discussed in terms of the stresses measured at the uniaxial gauges installed on the bottom of the deck plate at the intersection with the floor beam (EDPFB_1_Avg and WDPFB_1_Avg) and the back-to-back gauges installed on the floor beam web (EDPFB_2_Avg and WDPFB_2_Avg) with the section coinciding with the centerline of the middle load pad. The gauges on the bottom of the deck plate were oriented in the longitudinal direction of the deck and normal to the floor beam-to-deck plate weld and the gauges on the floor beam were oriented in the depth direction of the web (vertical direction) and normal to the floor beam-to-deck plate weld.

The measurements at some of the gauges for three trials are plotted in Figures 135 and 136 with FEA results shown as red dots. It is evident from the plots that the results of the static tests for each specimen were repeatable, and were generally linear elastic. Residual stresses were close to zero at most of the gauge locations. However, high residual stresses were observed for MU3 at EDPFB_2_Avg (Figure 135) after the first static trial, which were later eliminated by subsequent trials. The measured compressive stress at the deck plate in the longitudinal direction was significantly less than the analytical prediction. It appears that due to the relatively larger stiffness of the floor beam compared to the deck plate, larger contact pressure developed on the deck plate

above the floor beam, which caused less longitudinal bending of the of the deck plate. In a high stress gradient that was predicted in FEA at this location, a small change in installed gauge location could also cause this large variation.

The measurements of the three specimens are compared in the Figures 137 and 138. As seen from the figure, the measurements for the three specimens are comparable. The results show similar trend as FEA and were generally compressive as predicted from FEA. However, the measure compressive stress at the gauges on the east face of the floor beam web were closer to the analytical prediction as compared to the measurements at the gauges on the west face , but even the stresses on the east side was higher than the FEA results. One of the reasons for this deviation between the analytical and the experimental results could be the difference in locations of the proposed and as-installed gauge. In a high stress gradient field that was predicted at this location, a small change in location of the strain gauge could cause significant variation in measured stress. The measured compressive stress on the west face of the floor beam was significantly higher than the analytical prediction. Though no out-of-plane bending was predicted from FEA, the difference in stress between the east and the west face was due to the flexural deformation in out-of-plane of the floor beam web. This was caused due to the difference in loads at the east and the west actuators; however no fatigue crack was reported in any of the specimen. The measured stresses on the bottom of the deck plate in the east and the west sides were different which indicates unequal bending of the deck plate on either side of the floor beam web, the reason for which has been discussed earlier.

The change in stresses at these gauges during the fatigue tests is shown in Figures 139 and 140 with respect to the maximum stress measured during the static test at the onset of the fatigue testing and the maximum stress measured during the last static test on the cracked specimen. The dates for these tests are given earlier in section 3.6.5. No significant change was noted these gauges, except in MU2 for the gauges on the floor beam web. However, no fatigue damage was detected at the connection.

4.1.3 Response of Rib-to-Deck Plate Connection

Response of rib-to-deck plate connection is discussed in terms of the stresses measured at the uniaxial gauges installed on the rib wall and the top and bottom surfaces of the deck plate, symmetrically on the east and the west side with the sections coinciding with the center lines of the east and the wets load pads respectively. The gauges on the top ((W/E)TDP_1_Avg & (W/E)_TDP_2_Avg) and the bottom ((W/E)BDP_I1_Avg & (W/E)BDP_I2_Avg and (W/E)BDP_E1_Avg & (W/E)BDP_E2_Avg) surfaces of the deck plate were oriented in the transverse direction of the deck and normal to the rib-to-deck plate weld. The gauges on the rib wall was installed in back-to-back configuration and oriented along the rib, normal to the rib-to-deck plate weld. The gauge channels were (W/E)RIB_I1_Avg & (W/E)RIB_I2_Avg and (W/E)RIB_E1_Avg & (W/E)RIB_E2_Avg on the inner and the outer surfaces of the rib wall respectively.

The measurements at some of the gauges for the three trials are plotted in Figures 140 to 144 with FEA results shown as red dots. The measured stresses were linear elastic and agreed well with the FEA results, except at the gauges on the top of the deck for MU3. These gauges followed an opposite trend to that of FEA. One of the reasons for this deviation between the analytical and experimental results could be due to mal-functioning of these gauges, as they might got damaged due to pounding of the load pads. Residual stresses were close to zero at the gauge locations.

The measurements of the three specimens are compared in the Figures 145 and 146. As it is evident from the figure, the results for the three specimens showed similar trend as of FEA and the measurements matched well for the three specimens. As expected from FEA, the stresses were tensile and compressive on the top and the bottom surfaces of the deck plate respectively at the connection, as the rib-to-deck plate connection experienced local out of plane bending under the wheel loads. As predicted from FEA, the stresses on the outer and inner faces of the rib wall were tensile and compressive respectively, both to the east and the west side suggesting large flexural deformation in out of plane of the rib wall. However the magnitude of the stresses on the inner and outer faces of the rib was not same, indicating presence of axial stresses in the rib wall.

4.1.4 Response of Rib-to-Floor Beam connection

The response of the rib-to-floor beam connection is presented in terms of the stresses measured at the gauges on the floor beam web and the rib wall at the rib-to-floor beam connection. The specimens were extensively instrumented at the rib-to-floor beam connection. All the gauges on the floor beam web at the rib-to-floor beam connection were installed symmetrically on the north and south sides of the rib, and on each side the gauges were placed back-to-back on the east and west faces of the floor beam web to measure the in-plane membrane and the out of plane stress components. The gauges on the rib wall were installed symmetrically on the on the north and the south walls of the rib wall as well as to the east and the west sides of the rib.

The measurements at the gauges for the three trials for each specimen are plotted in Figures 147 to 151 with FEA results shown as red dots. It is evident from the plots that the results of the static tests for each specimen were repeatable, and were generally linear elastic. Residual stresses were close to zero at most of the gauge locations. However, high residual stresses were observed for some of the gages after the first static trial, which were later eliminated by subsequent trials. The results show similar trend as FEA and were comparable with the analytical predictions (see discussions later).

The FEA results had indicated a higher stress normal to the weld toe on the rib wall at about 60 degrees from the rib-soffit, and therefore back-to-back rosette gauges were installed on the floor beam web at this location both on the north and the south sides of the rib. The principal stresses determined from the rosette gages are tabulated in Table 2 to Table 5. The layout of the rosette gauges and the direction of the principal stresses are also shown in the respective tables. Tensile stresses are defined as +ve. The

direction of principal stresses is presented for either of the principal stresses with respect to the vertical axis passing through the center of the rosette. The angle is defined +ve in the counter clockwise direction. During the fatigue tests, cracks initiated from the weld root, subjected to the maximum principal stress field. However, with the available technology it was not possible to measure the principal stress at the weld root. The principal stresses at the weld root were obtained from FEA and were compared to the available measurements from the rosettes near the weld toe and are shown in Figures 152 to 155. Tensile stress developed towards the north side of the connection, and compressive stress developed towards the south side or the loading side of the connection. The principal stresses on the west face of the floor beam were less than that of the east face indicating some out-of-plane bending of the floor beam web. One of the reason for this difference was that the load level in west actuator was slightly higher than the east actuator in all the three specimens causing out-of-plane bending of the floor beam web. The magnitude of the measured principal stresses were comparable to the FEA results, and the orientation of the principal stresses matched well with the FEA results except for the south-west rosette (Figure 155). The reason for the anomaly at the south-west rosette gage can be due to the installation of the rosette at the incorrect location. Being an area with high stress gradient, a slight shift in position of the gage would change the result by a significant amount. The orientation of the principal stresses were almost tangential to the rib-to-floor beam connection. The distribution of principal stresses was consistent with the transfer of simulated wheel loads from the deck to the box girder section by shear in the floor beam web. Shear force was developed in the shear span between the distributed loads and the nearest support section (in this case the simulated box girder section at Support Col. B). In this shear span, a diagonal tension field developed in the floor beam web from the bottom (tension) flange to the top corner. The diagonal tensile field deviated around the rib rounding due to discontinuity in the floor beam web causing stress concentration at the rib-to-floor beam connection around the rib rounding. The diagonal tension field being tangential to the connection, the maximum principal stress was about tangential to the rib-to-floor beam connection.

The measured principal stresses and their orientation was used to calculate the stress along the rosette arms, one of which was aligned normal to the rib-to-floor beam weld toe. Fatigue cracking at the weld toe is primarily attributed to the crack growth from the micro discontinuities subject to the stress range normal to the weld toe. Figures 156 to 159 show the variation of stresses normal to the weld toe on the floor beam web along radial lines as determined from the rosette measurements and the uniaxial gages installed along the radial lines. The FEA results are also plotted for comparison. The measured stresses showed similar trend as of FEA with largest magnitude of stress observed at the first gage (closest to the weld toe) and then stresses progressively reducing at the subsequent gages. Similar trend was also observed for the stresses normal to the weld toe on the rib wall as is shown in Figures 160 to 163.

4.2 Fatigue Test Results

4.2.1 Fatigue Cracking in MU1

The first crack was detected after 734,126 cycles at the floor beam to rib connection to the south (compression side) of the rib at about 30 degrees from the rib soffit. The crack was detected on October 21, 2012 during the 12:00 PM inspection. The crack grew through the weld throat and propagated into the floor beam and the ribs on both side of the floor beam (Figure 164). The crack progressed about 0.8 in. (25 mm) into the floor beam web and about 0.7 in. (18 mm) into the rib wall. Similar crack was observed after 858,304 cycles in the floor beam to rib connection to the north side (tension side) of the rib at about 26 degrees from the rib soffit (Figure 165). The crack was detected on October 24, 2012 during the 8:00 PM inspection. This crack also grew through the weld throat and propagated into the floor beam and the rib. The crack progressed about 0.3 in. (8 mm) into the floor beam web and about 0.4 in. (10 mm) into the rib wall. A schematic of the cracks is shown in Figure 166. The fatigue test was terminated on October 27, 2012 after 1144818 cycles when the crack in the floor beam on the north side of the rib propagated through the hole and appeared at the edge of the drilled hole.

Uniaxial strain gauges were provided on the floor beam web and the rib wall at 30 degrees from the rib soffit, near the crack origins, oriented normal to the rib-to-floor beam weld toes. The FEA results had indicated a higher stress normal to the weld toe at about 60 degrees from the rib-soffit, and therefore back-to-back rosette gauges were installed on the floor beam web at this location both on the north and the south sides of the rib. However, the fatigue cracks developed from the weld root, where measurement of stresses was not possible. As such, the critical stresses normal to the crack path were determined from FEA results that were verified against available measurements.

The contours of maximum and principal stresses in the floor beam as obtained from FEA results are presented in Figure 167 and Figure 168. Also marked on the figures are the crack paths. Significant stress concentrations were noted at the rib-to-floor beam weld toe near the crack origins. The larger (in magnitude) principal stress to the north and the south were tensile and compressive respectively. Direction of principal stresses on sections along the crack paths are shown in Figure 169 and Figure 170. Note that the sections have been extended to the edge of the specimen model, although in physical structure the crack length at the time of the test termination was much less. As is seen, the principal stresses were nearly normal to the crack path. Hence, it may be concluded that the fatigue cracks grew normal to the principal stresses, and the principal stresses were responsible for the observed fatigue cracking. It should be noted that although the south side welded connection was subjected to nominal compressive stress range, the local stress range at the weld was tensile in presence of high tensile residual stress in the order of yield strength of the material. As such, fatigue cracking was observed under compressive stress field at this location.

Figure 171 shows the distribution of the circumferential stresses along the weld root (tangential to the rib soffit) of the rib-to-floor beam connection. The circumferential stress is critical for crack growth from volumetric discontinuities at the weld root. As is

evident, the maximum tensile circumferential stress at the weld root was about 24.6 ksi and occurred at about 52 degrees from the rib soffit. The maximum compressive circumferential stress at the weld root was 31 ksi and occurred at about 58 degrees from the rib soffit. The circumferential stresses at the weld root at about 25 to 30 degrees from the rib soffit were estimated to be about 22 ksi compressive and 18 ksi tensile. These stresses would explain the observed fatigue cracking from the weld root on the south and the north sides.

Fatigue test results of the rib-to-floor beam welded detail in MU1 are presented in Figure 172 against the AASHTO fatigue design curves of the AASHTO LRFD Bridge Design Specifications. The fatigue life of the connection detail at the first observation of the cracks is plotted against the principal stresses at the weld root (origin of the fatigue cracks) as obtained from the FEA results. The detail exhibited a fatigue resistance exceeding AASHTO Category B'. It should be noted that the AASHTO detail classifications are based on nominal stresses; whereas the test results for the rib-to-floor beam welded connection is plotted based on local stress at the weld root, considering the gross weld geometry but without any consideration of the LOF at the weld root. Due to the complex distribution of stresses, it is not possible to assess the nominal stresses at the welded connections for orthotropic decks, and the conventional local stress based methodologies (such as hot spot stress approach) is not applicable to root cracking. Moreover, with the currently available technology it is not possible to measure the stresses at the weld root. Thus, the assessment of the fatigue performance of the rib-to-floor beam welded connection presented here is subjective. Nevertheless, the rib-to-floor beam welded details in MU1 exhibited similar fatigue resistance against root cracking as welded beams developing fatigue cracks from the web-to-flange weld.

4.2.2 Fatigue Cracking in MU2

After 1,168,940 cycles two sets of cracks were detected at the floor beam to rib connection. The cracks were detected on November 10, 2012 during the 8:00 PM inspection. One set of cracks initiated on the north side from the weld root at about 8 degrees from the rib soffit (Figure 173) while the other set of cracks initiated on the south side from the weld root at about 30 degrees from the rib soffit (Figure 174). The cracks grew through the weld throat and propagated into the floor beam and the ribs on both side of the floor beam. The crack on the north side progressed about 0.4 in. (10 mm) into the floor beam web and about 0.6 in. (15 mm) into the rib wall, while the crack on the south side progressed about 0.3 in. (8 mm) into the floor beam web and about 0.7 in. (18 mm) into the rib wall. A schematic of the cracks is shown Figure 175. The fatigue test was terminated on November 13, 2012 after 1,296,259 cycles when the cracks propagated through the holes in both north and south sides and appeared at the edge of the drilled holes.

Similar to MU1, the critical stresses normal to the crack path were determined from FEA results that were verified against available measurements. The contours of maximum and principal stresses in the floor beam as obtained from FEA results are presented in Figure 176 and Figure 177. Also marked on the figures are the crack paths. Significant stress concentrations were noted at the rib-to-floor beam weld toe near the crack

origins. The larger (in magnitude) principal stress to the north and the south were tensile and compressive respectively. Direction of principal stresses on sections along the crack paths are shown in Figure 178 and Figure 179. Note that the sections have been extended to the edge of the specimen model, although in physical structure the crack length at the time of the test termination was much less. Similar to MU1, the principal stresses were nearly normal to the crack path. Hence, it may be concluded that the fatigue cracks grew normal to the principal stresses, and the principal stresses were responsible for the observed fatigue cracking as it was also noted in case of MU1. It should be noted that although the south side welded connection was subjected to nominal compressive stress range, the local stress range at the weld was tensile in presence of high tensile residual stress in the order of yield strength of the material. As such, fatigue cracking was observed under compressive stress field at this location.

Figure 180 shows the distribution of the circumferential stresses along the weld root (tangential to the rib soffit) of the rib-to-floor beam connection. As is evident, the maximum tensile circumferential stress at the weld root was about 25 ksi and occurred at about 52 degrees from the rib soffit. The maximum compressive circumferential stress at the weld root was 31.8 ksi and occurred at about 56 degrees from the rib soffit. The circumferential stresses at the weld root at about 30 degrees from the rib soffit were estimated to be about 23 ksi compressive and 20 ksi tensile. These stresses would explain the observed fatigue cracking from the weld root on the south side.

Fatigue test results of the rib-to-floor beam welded detail in MU2 are presented in Figure 181 against the AASHTO fatigue design curves of the AASHTO LRFD Bridge Design Specifications. The fatigue test results are presented here in the similar manner as in MU1. The detail on the south side exhibited a fatigue resistance exceeding AASHTO Category B; however the detail on the north side exhibited a fatigue resistance exceeding AASHTO Category E. The reason for the poor fatigue resistance exhibited by the north detail in MU2 is not clear. Visual examination of the fracture surface did not reveal any unusual flaw that would explain the performance. The assessment of the fatigue performance of the rib-to-floor beam welded connection presented here is subjective, the reason for which is already discussed in section 4.2.1. Nevertheless, the rib-to-floor beam welded details (except the north detail) in MU2 exhibited similar fatigue resistance against root cracking as welded beams developing fatigue cracks from the web-to-flange weld.

4.2.3 Fatigue Cracking in MU3

After 762,860 cycles two sets of cracks were detected at the floor beam to rib connection on the south side of the rib. The cracks were detected on November 17, 2012 during 8:00 PM inspection. One crack initiated from the weld root at about 60 degrees from the rib soffit and the other crack initiated from the weld root at about 35 degrees from the rib soffit (Figure 182). The 60 degree crack progressed about 0.3 in. (8 mm) into the floor beam web and about 0.4 in. (10 mm) into the rib wall, while the 35 degree crack was detected when it grew though the weld throat and appeared on the surface of the weld. The cracks grew through the weld throat and propagated into the floor beam and the ribs on both side of the floor beam. Fatigue crack initiated on the

north side after 1,716,160 cycles from the weld root at 29 degrees from the rib soffit (Figure 183). The cracks grew through the weld throat and propagated into the floor beam and the ribs on both side of the floor beam (Figure 183). The test was terminated by this crack since the crack grew significantly into the floor beam and the rib wall. A schematic of the cracks is shown Figure 184.

Similar to the other mockup specimens, the critical stresses normal to the crack path were determined from FEA results that were verified against available measurements. The contours of maximum and principal stresses in the floor beam as obtained from FEA results are presented in Figure 185 and Figure 186and . Also marked on the figures are the crack paths. Significant stress concentrations were noted at the rib-to-floor beam weld toe near the crack origins. The larger (in magnitude) principal stress to the north and the south were tensile and compressive respectively. Direction of principal stresses on sections along the crack paths are shown in Figure 187, Figure 188 and Figure 189. Note that the sections have been extended to the edge of the specimen model, although in physical structure the crack length at the time of the test termination was much less. Similar to the other two mockup specimens, the principal stresses were nearly normal to the crack path. Hence, it may be concluded that the fatigue cracks grew normal to the principal stresses, and the principal stresses were responsible for the observed fatigue cracking as it was also noted in case of other specimens. It should be noted that although the south side welded connection was subjected to nominal compressive stress range, the local stress range at the weld was tensile in presence of high tensile residual stress in the order of yield strength of the material. As such, fatigue cracking was observed under compressive stress field at this location.

Figure 190 shows the distribution of the circumferential stresses along the weld root (tangential to the rib soffit) of the rib-to-floor beam connection. As is evident, the maximum tensile circumferential stress at the weld root was about 24.8 ksi and occurred at about 52 degrees from the rib soffit. The maximum compressive circumferential stress at the weld root was 31.1 ksi and occurred at about 56 degrees from the rib soffit. The circumferential stresses at the weld root at about 30 to 35 degrees from the rib soffit were estimated to be about 26 ksi compressive and 22 ksi tensile. These stresses would explain the observed fatigue cracking from the weld root on the south and the north sides.

Fatigue test results of the rib-to-floor beam welded detail in MU3 are presented in Figure 191 against the AASHTO fatigue design curves of the AASHTO LRFD Bridge Design Specifications. The fatigue test results are presented here in the similar manner as reported for other specimens. The detail exhibited a fatigue resistance exceeding AASHTO Category B. The assessment of the fatigue performance of the rib-to-floor beam welded connection presented here is subjective, the reason for which is already discussed in section 4.2.1. Nevertheless, the rib-to-floor beam welded details in MU3 exhibited similar fatigue resistance against root cracking as welded beams developing fatigue cracks from the web-to-flange weld.

Fatigue testing of the mock-up specimens identified a failure mode of the rib-to-floor beam welded connection by crack growth from the LOF at the weld root, when the

fatigue cracking from the weld toe or through the weld throat was suppressed. This failure mode was not identified in the existing literature. Fatigue results of the rib-to-floor beam welded details for MU1, MU2 and MU3 are presented in Figure 192 against the AASHTO fatigue design curves. Excluding the fatigue performance of the north detail in MU2, which demonstrated a significantly lesser fatigue resistance, the fatigue resistance of the connection detail exceeded AASHTO Category B'. The data points were apparently within the usual scatter of the subject connection detail. Nevertheless, the adequately fabricated PJP rib-to-floor beam weld detail in MU3 exhibited better performance than the corresponding fillet welded details.

It should be noted that the AASHTO fatigue design curves are developed based on fatigue test results on full scale beam specimens under constant amplitude loading and represent 95% confidence on 95% probability of survival fatigue life. Due to inherent variability, welded connections are expected to exhibit scatter in their fatigue performance. The limited test data for the subject deck was inadequate to evaluate this scatter and draw any statistically significant conclusion. In that respect the fatigue test results from this study should be considered as indicative.

4.2.4 Evaluation of Intermittent Static Test Results

Based on the above findings, it was realized that the gauges installed on the floor beam web and the rib wall adjacent to the cracked regions of the rib-to-floor beam connection would show deviation from stresses during undamaged state of these connections. Holes were drilled ahead of the crack tip to prevent the further growth of the crack. Nevertheless, it was decided to continue the fatigue testing as per the original target of maximum of $8x10^6$ cycles or re-initiation of crack on the edge of the holes whichever is earlier, to produce data for the other critical details of the deck such as rib-to-deck plate welds. However to monitor and correlate the fatigue crack growth at the rib-to-floor beam connection by monitoring the change in stresses at these gauges adjacent to the cracks, it was decided to conduct static tests each time after a hole is drilled and a fatigue test is reinitiated. For the chronological sequence of the events during the fatigue tests, refer to section 3.6.5, contained in Volume I. The measurements at those gauges during the different static tests are compared in this section.

Static Tests in MU1

The location of gauges on the floor beam web and the rib wall adjacent to the rib-to-floor beam connection is discussed in section 3.6.3, contained in Volume I. Significant change in stresses was noted at the gauges adjacent to the fatigue cracks during fatigue testing. Figure 193 to Figure 196 show the change in stresses during the entire fatigue test. The results of the static tests performed during the execution of the fatigue test, including the tests performed prior to initiating the fatigue test are plotted as discrete points. The analytical prediction is shown as a continuous line. For the chronological sequence of the static tests refer to section 3.6.5, contained in Volume I.

Figure 193 shows the history of maximum stresses recorded at the uniaxial gauges installed on the west face of the floor beam web along a path at 30 degrees from the rib

soffit to the south of the rib. Compressive stresses of 15.6 ksi and 11.3 ksi were measured at these gauges at the onset of fatigue testing. Reduction in compressive stresses by about 14 ksi was noted at the gauges during the static test on October 24, 2012, following the fatigue crack to the south of the rib. The gauges malfunctioned when the fatigue test was reinitiated after this static test.

Figure 194 shows the change in the maximum stresses recorded at the uniaxial gauges installed on the outer face of the rib wall along a path at 30 degrees south from the rib soffit to the east of floor beam. Compressive stresses of 19.5 ksi and 1.6 ksi were measured at these gauges at the onset of fatigue testing. Reduction in compressive stresses by about 5 ksi was noted at the gauge abutting the weld toe on the rib during the static test on October 24, 2012, following the fatigue crack to the south of the rib.

Figure 195 shows the history of maximum stresses recorded at the uniaxial gauges installed on the east face of the floor beam web along a path at 30 degrees from the rib soffit to the north of the rib. Tensile stresses of 7.2 ksi and 6 ksi were measured at these gauges at the onset of fatigue testing. Reduction in tensile stresses by about 2 ksi and 1 ksi respectively, was noted during the static test on October 24, 2012 following the fatigue crack to the south of the rib. However, no fatigue cracking was visible on the north side. The fatigue cracking to the south of the rib affected the stress field to the north side which resulted in this reduction of stresses. Following the fatigue crack to the north of the rib, static test was conducted on October 26, 2012. Reduction in tensile stresses by about 5.5 ksi was noted at the gauges.

Figure 196 shows the change in the maximum stresses recorded at the uniaxial gauges installed on the outer face of the rib wall along a path at 30 degrees north from the rib soffit to the west of floor beam. Compressive stresses of 2.3 ksi and 8.7 ksi were measured at these gauges at the onset of fatigue testing. Increase in compressive stresses by about 3 ksi was noted during the static test on October 24, 2012 following the fatigue crack to the south of the rib. However, no fatigue cracking was visible on the north side. The fatigue cracking to the south of the rib affected the stress field to the north side which resulted in reduction of stresses. The gauges malfunctioned when the fatigue test was reinitiated after this static test.

Static Tests in MU2

Similar to MU1, significant change in stresses was noted at the gauges adjacent to the fatigue cracks during fatigue testing. Figure 197 to Figure 199 show the change in stresses during the entire fatigue test. These plots are presented in the same manner as in MU1. For the chronological sequence of the static tests refer to section 3.6.5, contained in Volume I.

Figure 197 shows the change in the stress recorded at the uniaxial gauge installed on the east face of the floor beam web along a path at 0 degrees from the rib soffit. Tensile stress of 6.5 ksi was measured at the gauge at the onset of fatigue testing. Reduction in tensile stress by about 1.2 ksi was noted during the static test on November 13, 2012 following the fatigue crack to the north and the south of the rib.

Figure 198 shows the history of maximum stresses recorded at uniaxial gauges installed on the rib soffit along a path to the west of floor beam. Compressive stresses of 17.5 ksi, 6.3 ksi and 6.4 ksi were measured at these gauges at the onset of fatigue testing. Increase in compressive stresses by about 8 ksi and 3 ksi was noted at the first two gauges during the static test on November 13, 2012 following the fatigue crack to the north and the south of the rib. The third gauge or the gauge farthest from the rib-to-floor beam weld toe on the rib didn't see much effect due to the crack growth because the fatigue test was terminated before the crack could have grown to that extent.

Figure 199 shows the change in stresses recorded at uniaxial gauges installed on the west face of the floor beam along a path at 30 degrees from the rib soffit to the south of the rib. Compressive stresses of 10 ksi and 5 ksi were measured at these gauges at the onset of fatigue testing. Reduction in compressive stresses by about 6.5 ksi and 5.5 ksi was noted during the static test on November 13, 2012 following the fatigue crack to the north and the south of the rib.

Static Tests in MU3

Similar to the other specimens, significant change in stresses was noted at the gauges adjacent to the fatigue cracks during fatigue testing. Figure 200 to Figure 202 show the change in stresses during the entire fatigue test. These plots are presented in the same manner as the other specimens. For the chronological sequence of the static tests refer to section 3.6.5, contained in Volume I. However, the effect of the 60° crack to the south of the rib on the adjacent gauges could not be studied because of the fact that due to the fatigue cracks and the drilled holes to prevent crack, the rosette and the strip gauges on the floor beam web and the gauges on the outer face of the rib wall at that location got damaged. And also, no static test was conducted on the specimen after the detection of the fatigue crack to the north of the rib, as this crack had grown significantly into the floor beam web and the rib wall and the test was terminated.

Figure 200 shows the change in stresses recorded at uniaxial gauges installed on the west face of the floor beam along a path at 30 degrees from the rib soffit to the south of the rib. Compressive stresses of 7.5 ksi and 5.7 ksi were measured at these gauges at the onset of fatigue testing. Reduction in compressive stresses by about 10 ksi was noted during the static test on November 19, 2012 following the fatigue cracks to the south of the rib.

Figure 201 shows the change in maximum stresses recorded at the uniaxial gauges installed on the east face of the floor beam web along a path at 30 degrees from the rib soffit to the north of the rib. Tensile stresses of 5.7 ksi and 2.1 ksi were measured at these gauges at the onset of fatigue testing. Reduction in tensile stresses by about 3.5 ksi and 1.6 ksi respectively, was noted during the static test on November 19, 2012 following the fatigue cracks to the south of the rib. However, no fatigue cracking was visible on the north side. The fatigue cracking to the south of the rib affected the stress field to the north side which resulted in this reduction of stresses.

Figure 202 shows the change in the maximum stresses recorded at the uniaxial gauges installed on the outer face of the rib wall along a path at 30 degrees north from the rib soffit to the east of floor beam. Tensile and compressive stresses of 3.0 ksi and 8.5 ksi were measured at these gauges at the onset of fatigue testing. Decrease in tensile stresses by about 4 ksi and increase in compressive stress by about 3.5 ksi were noted during the static test on November 19, 2012 following the fatigue crack to the south of the rib. However, no fatigue cracking was visible on the north side. The fatigue cracking to the south of the rib affected the stress field to the north side which resulted in this reduction of stresses.

Table 2 - Principal Stress in Floor Beam to the North of the Rib

		Measurements		Computed Principal Stresses[a] and Directions			
Face	Specimen Number	Channel ID	Stress[a] (ksi[b])	Maximum σ_p (ksi[b])	Maximum σ_q (ksi[b])	Direction[c] ϕ (degrees)	Illustration
East	MU1	NEFB_R1_Avg	17.0	22.7	16.8	32.1	
		NEFB_R2_Avg	11.7				
		NEFB_R3_Avg	10.7				
	MU2	NEFB_R1_Avg	15.3	22.0	17.9	45.3	
		NEFB_R2_Avg	11.6				
		NEFB_R3_Avg	12.6				
	MU3	NEFB_R1_Avg	14.9	21.1	15.6	42.0	
		NEFB_R2_Avg	9.9				
		NEFB_R3_Avg	10.7				

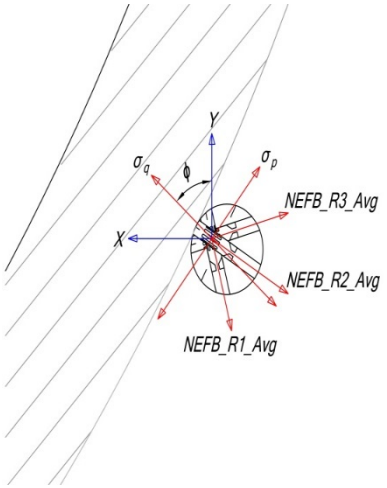

Notes:
[a] Tensile stresses are positive.
[b] 1 ksi = 6.91 MPa.
[c] Counter clockwise angles are positive, measured from the vertical axis (Y) passing through the center of rosette.

Table 3 - Principal Stress in Floor Beam to the North of the Rib

		Measurements		Computed Principal Stresses[a] and Directions			
Face	Specimen Number	Channel ID	Stress[a] (ksi[b])	Maximum σ_p (ksi[b])	Maximum σ_q (ksi[b])	Direction[c] ϕ (degrees)	Illustration
West	MU1	NWFB_R1_Avg	10.5	14.5	4.6	48.5	
		NWFB_R2_Avg	1.5				
		NWFB_R3_Avg	2.8				
	MU2	NWFB_R1_Avg	8.4	15.8	1.3	37.6	
		NWFB_R2_Avg	-3.1				
		NWFB_R3_Avg	3.5				
	MU3	NWFB_R1_Avg	8.1	15.5	2.6	35.9	
		NWFB_R2_Avg	-1.9				
		NWFB_R3_Avg	4.6				

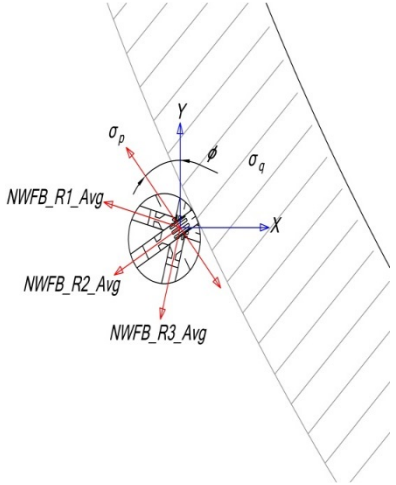

Notes:
[a] Tensile stresses are positive.
[b] 1 ksi = 6.91 MPa.
[c] Counter clockwise angles are positive, measured from the vertical axis (Y) passing through the center of rosette.

Table 4 - Principal Stress in Floor Beam to the South of the Rib

		Measurements		Computed Principal Stresses[a] and Directions			
Face	Specimen Number	Channel ID	Stress[a] (ksi[b])	Maximum σ_p (ksi[b])	Maximum σ_q (ksi[b])	Direction[c] ϕ (degrees)	Illustration
East	MU1	SEFB_R1_Avg	-4.0	-9.5	-24.9	93.1	
		SEFB_R2_Avg	-6.2				
		SEFB_R3_Avg	-20.1				
	MU2	SEFB_R1_Avg	0.1	-6.1	-20.8	72.2	
		SEFB_R2_Avg	-10.3				
		SEFB_R3_Avg	-18.9				
	MU3	SEFB_R1_Avg	-2.4	-6.6	-23.1	95.9	
		SEFB_R2_Avg	-3.2				
		SEFB_R3_Avg	-18.4				

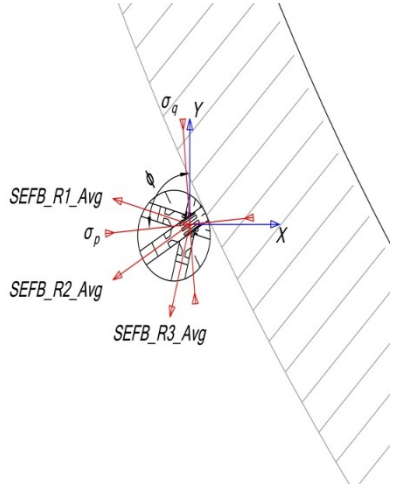

Notes:
[a] Tensile stresses are positive.
[b] 1 ksi = 6.91 MPa.
[c] Counter clockwise angles are positive, measured from the vertical axis (Y) passing through the center of rosette.

Table 5 - Principal Stress in Floor Beam to the South of the Rib

		Measurements		Computed Principal Stresses[a] and Directions			
Face	Specimen Number	Channel ID	Stress[a] (ksi)[b]	Maximum σ_p (ksi[b])	Maximum σ_q (ksi[b])	Direction[c] ϕ (degrees)	Illustration
West	MU1	SWFB_R1_Avg	-6.4	-10.8	-19.1	35.6	
		SWFB_R2_Avg	-14.1				
		SWFB_R3_Avg	-14.6				
	MU2	SWFB_R1_Avg	-6.4	-16.8	-35.0	18.2	
		SWFB_R2_Avg	-19.4				
		SWFB_R3_Avg	-29.9				
	MU3	SWFB_R1_Avg	-6.5	-11.7	-24.4	-6.0	
		SWFB_R2_Avg	-7.1				
		SWFB_R3_Avg	-18.7				

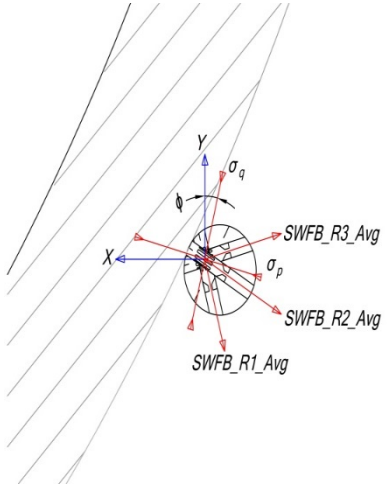

Notes:
[a] Tensile stresses are positive.
[b] 1 ksi = 6.91 MPa.
[c] Counter clockwise angles are positive, measured from the vertical axis (Y) passing through the center of rosette.

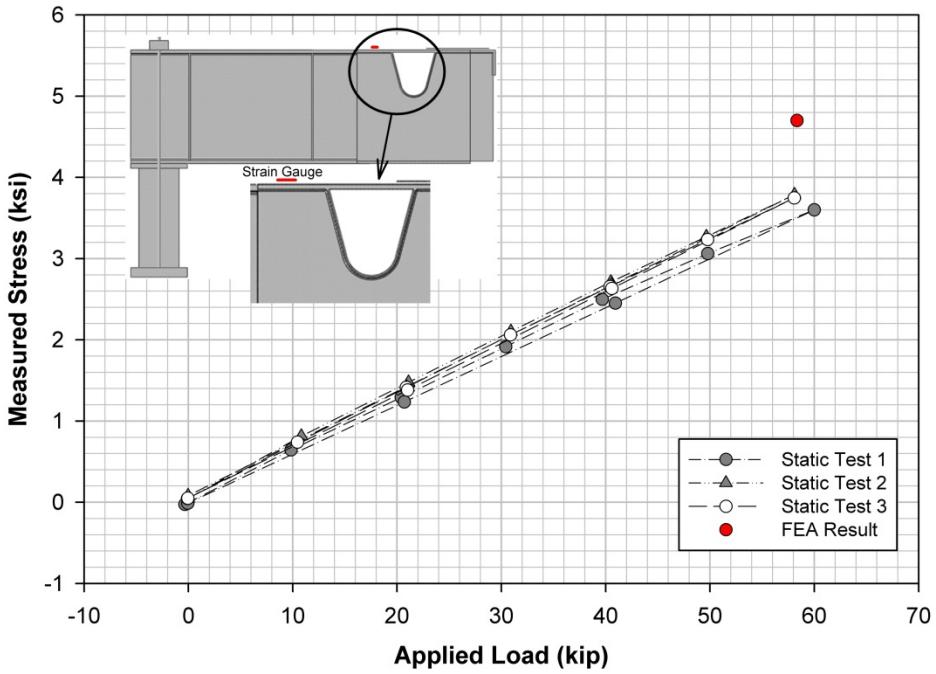

Figure 116. Measurements at strain gauge TDP_WEB_Avg in MU1

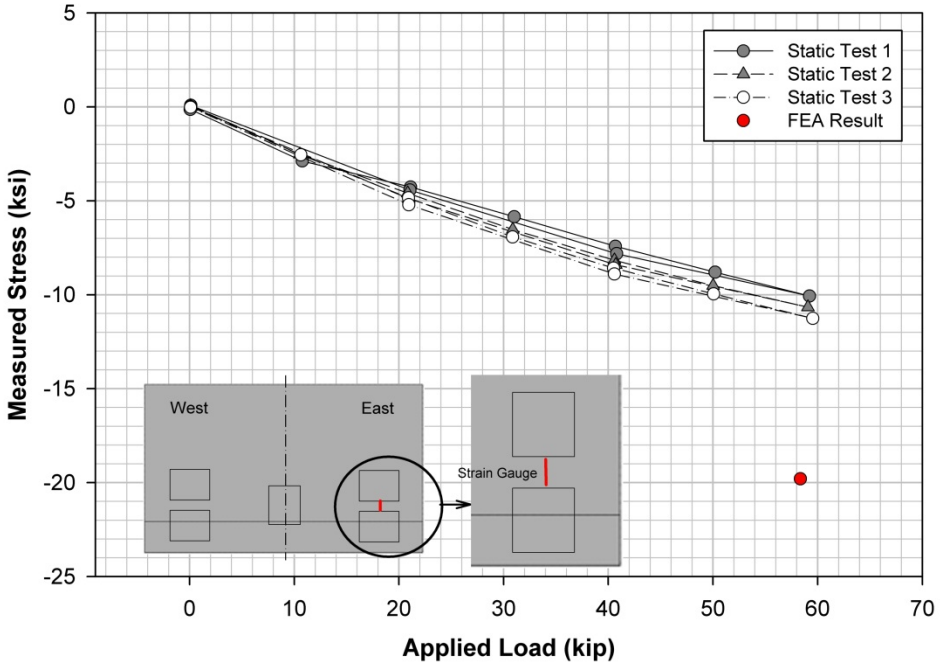

Figure 117. Measurements at strain gauge ETDP_3_Avg in MU2

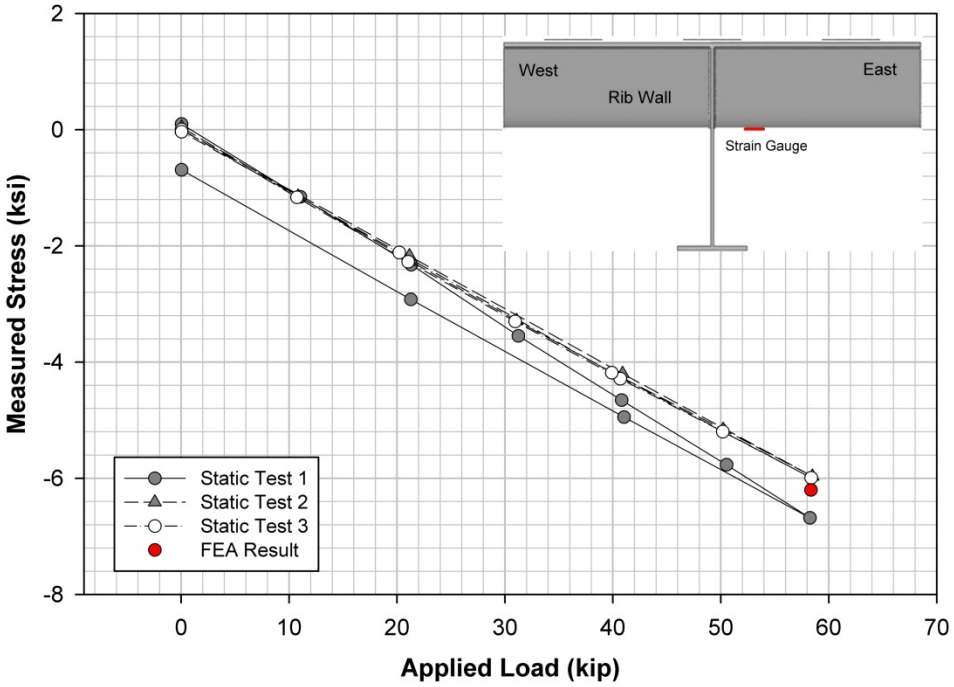

Figure 118. Measurements at strain gauge ER_0_3_Avg in MU3

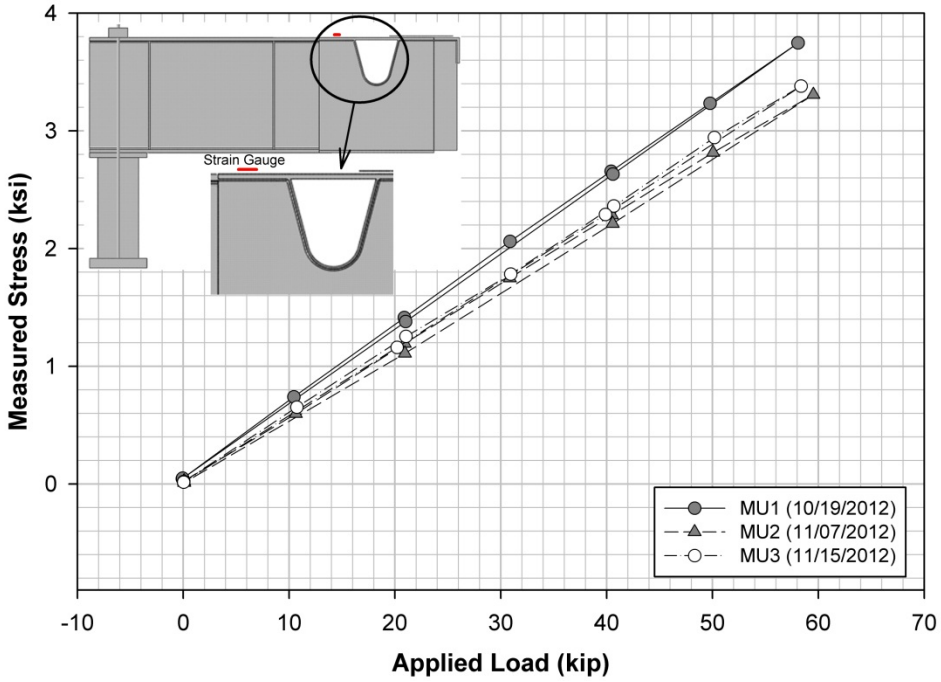

Figure 119. Comparison of measurements at strain gauge TDP_WEB_Avg

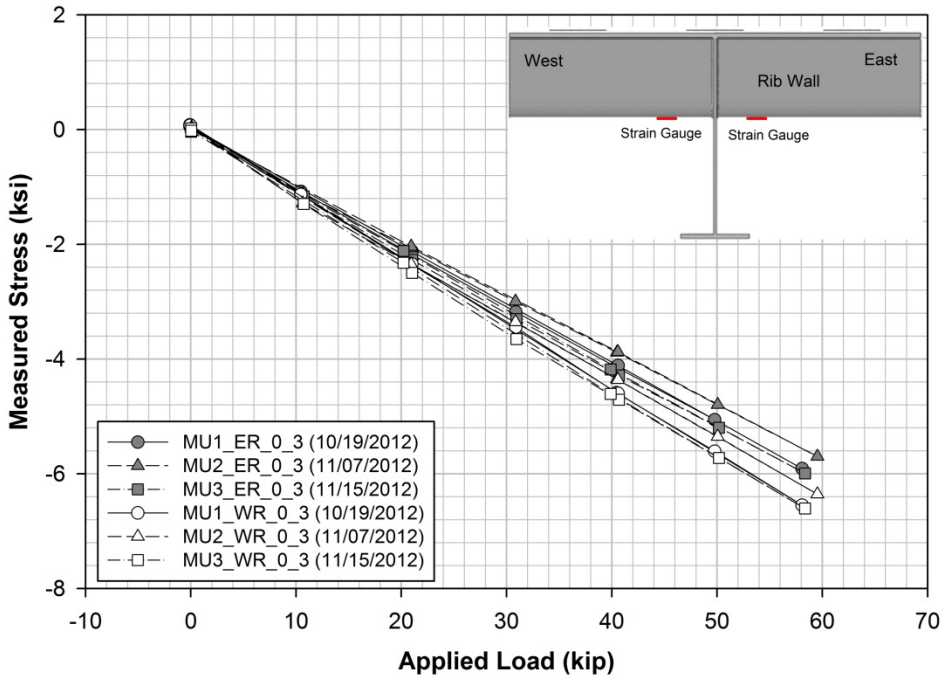

Figure 120. Comparison of measurements at strain gauges ER_0_3_Avg and WR_0_3_Avg

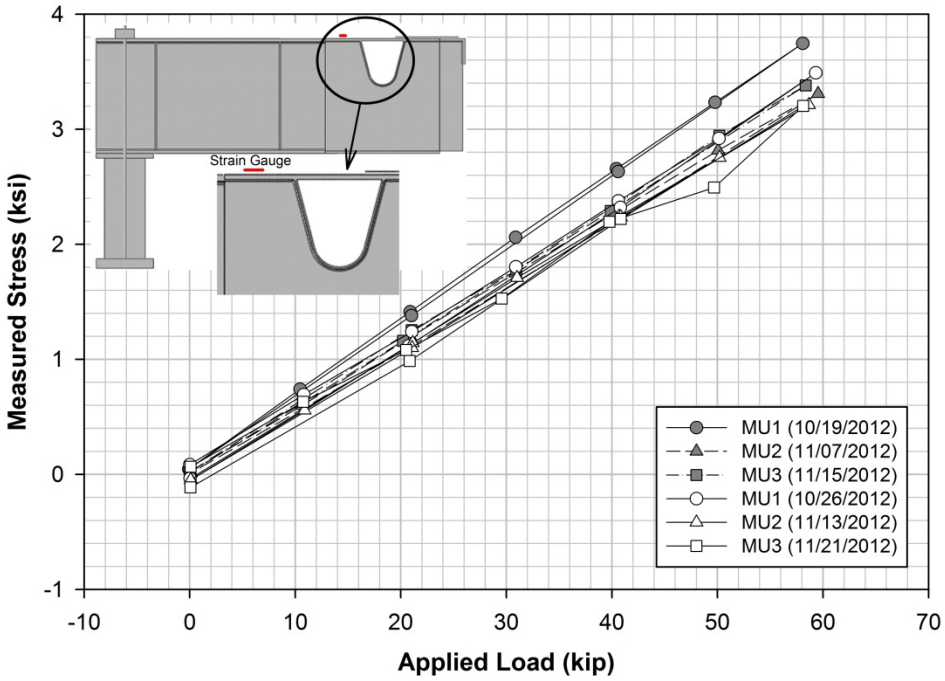

Figure 121. Comparison between measurements during the static tests before the onset of the fatigue testing and the static tests in the cracked specimen, at strain gauge TDP_WEB_Avg

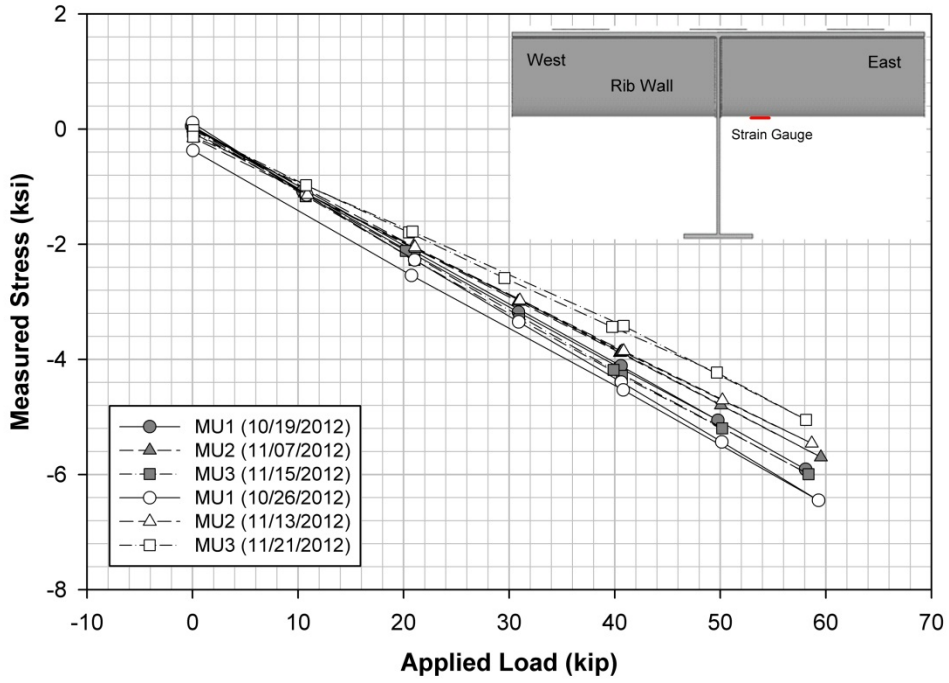

Figure 122. Comparison between measurements during the static tests before the onset of the fatigue testing and the static tests in the cracked specimen, at strain gauge ER_0_3_Avg

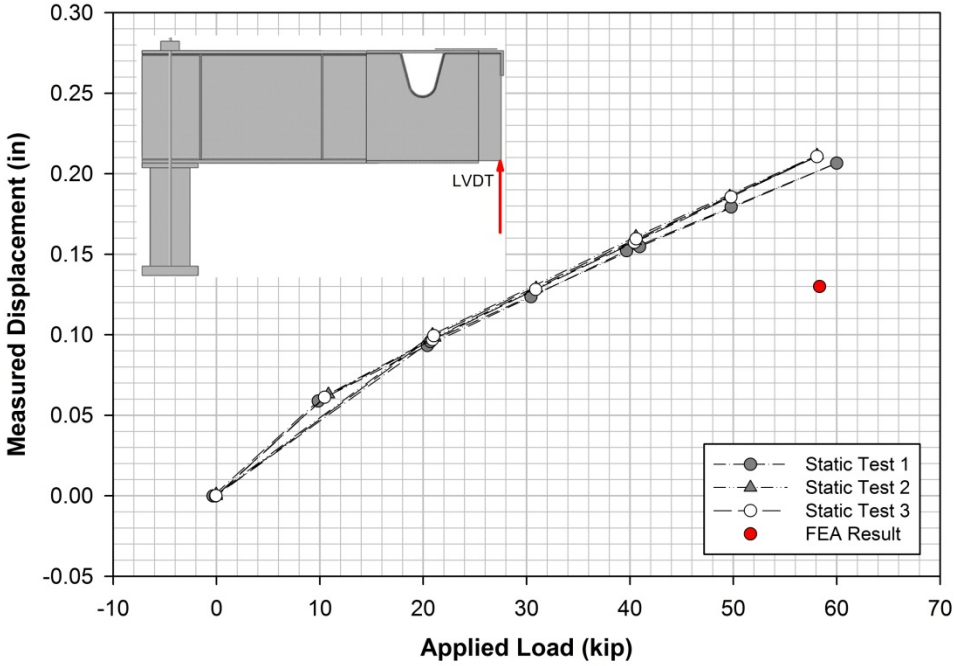

Figure 123. Measurements at strain gauge DISPL_Avg in MU1

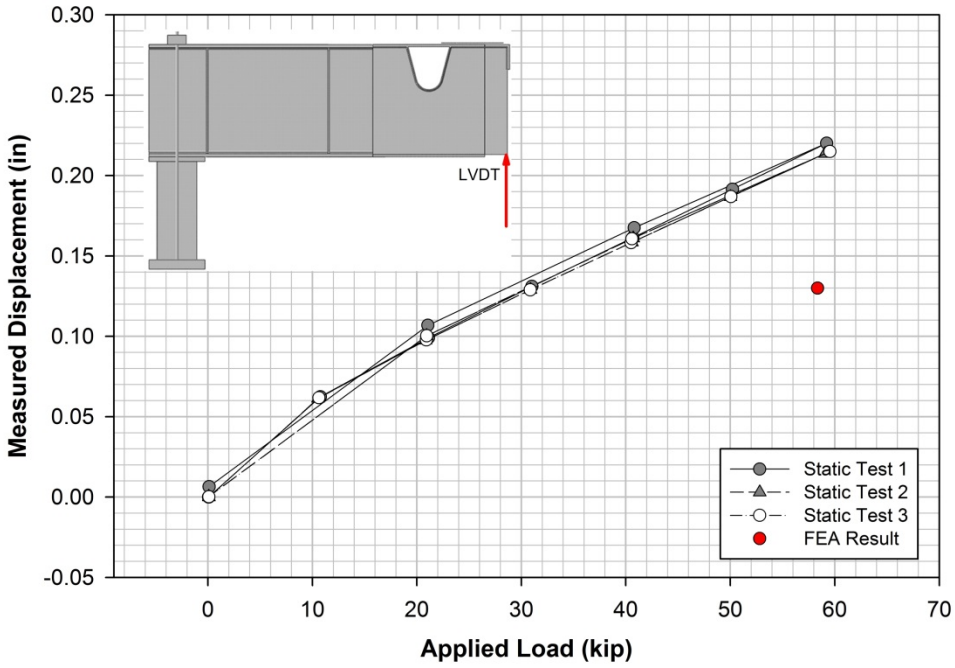

Figure 124. Measurements at strain gauge DISPL_Avg in MU2

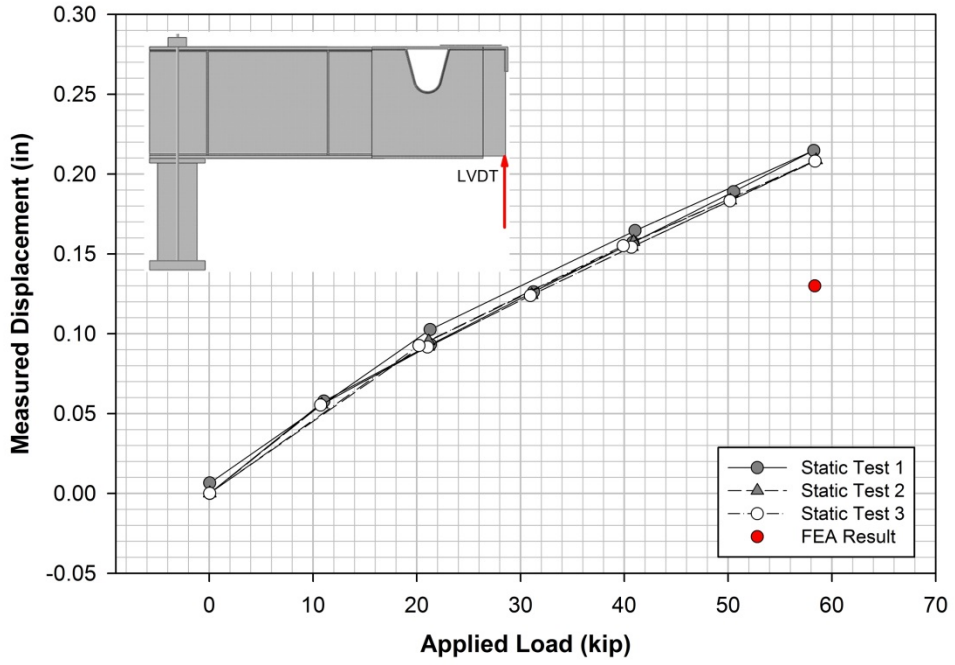

Figure 125. Measurements at strain gauge DISPL_Avg in MU3

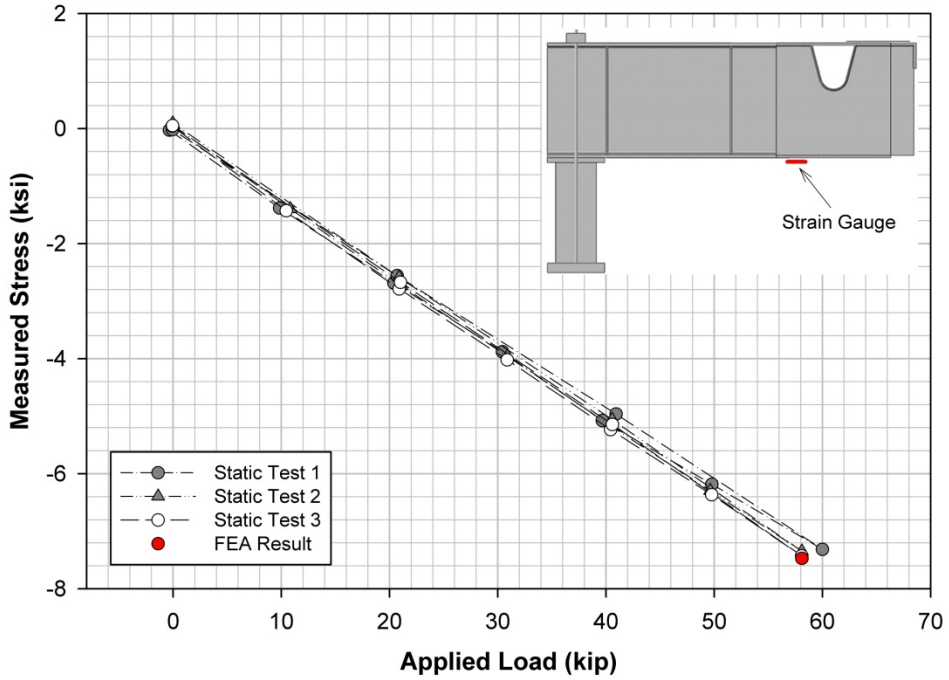

Figure 126. Measurements at strain gauge BDP_WEB_Avg in MU1

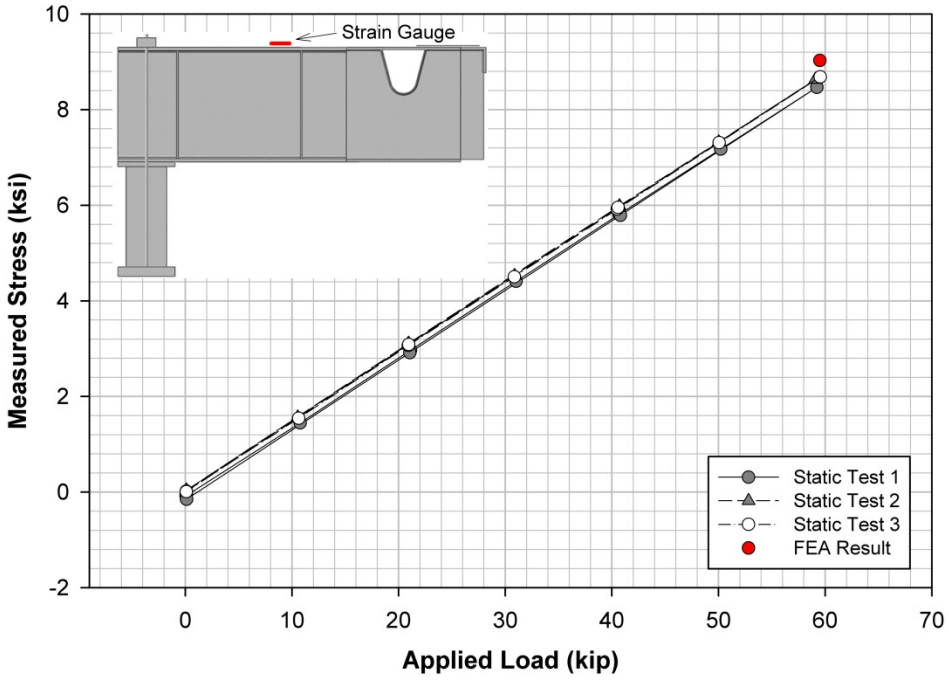

Figure 127. Measurements at strain gauge TF1_Avg in MU2

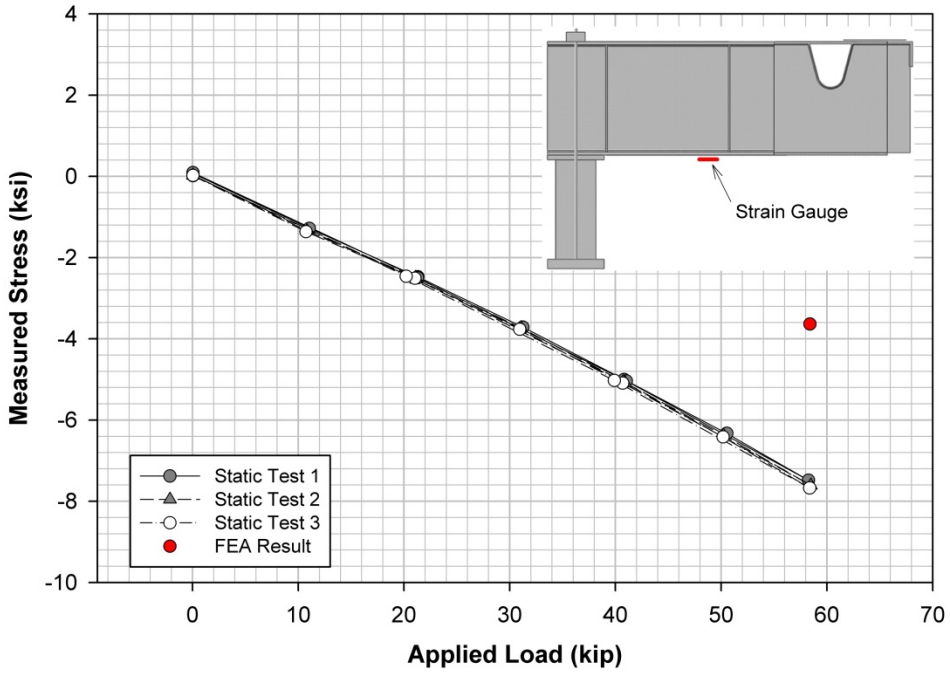

Figure 128. Measurements at strain gauge BF1_Avg in MU3

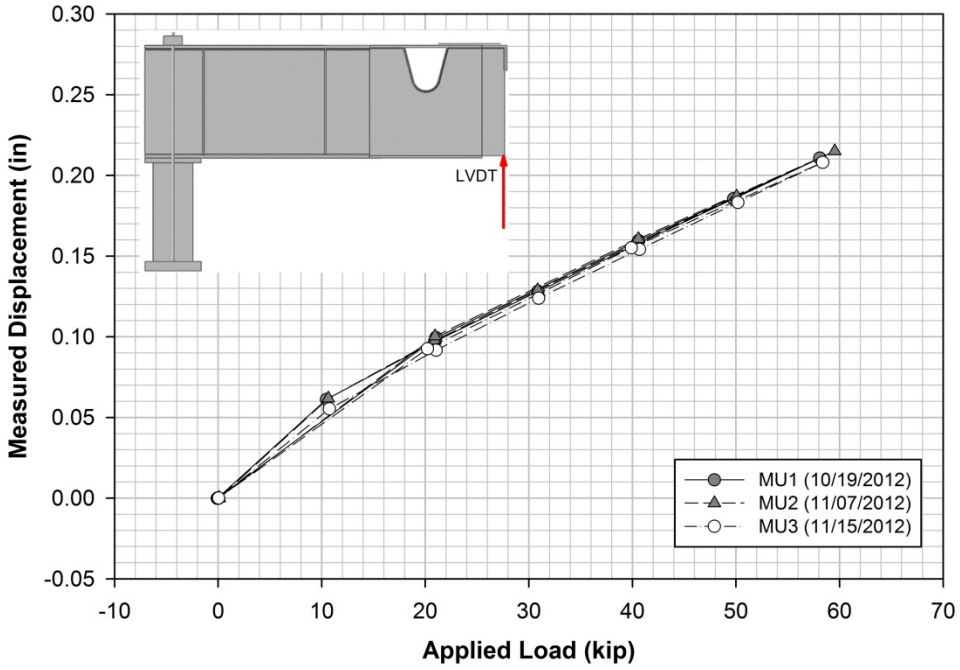

Figure 129. Comparison of measurements at strain gauge DISPL_Avg

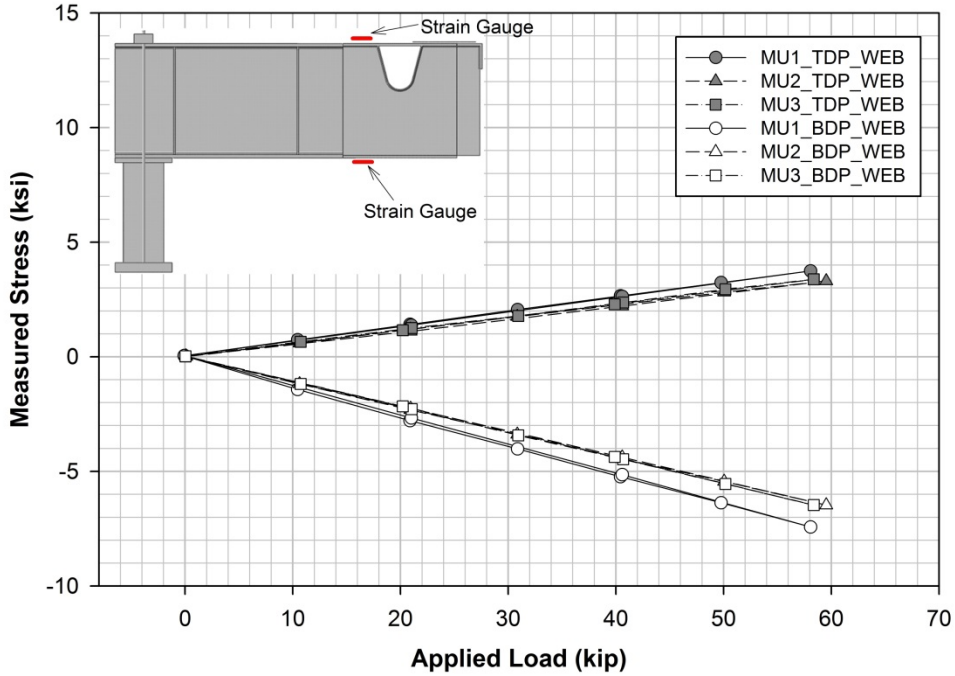

Figure 130. Comparison of measurements at strain gauges TDP_WEB_Avg and BDP_WEB_Avg

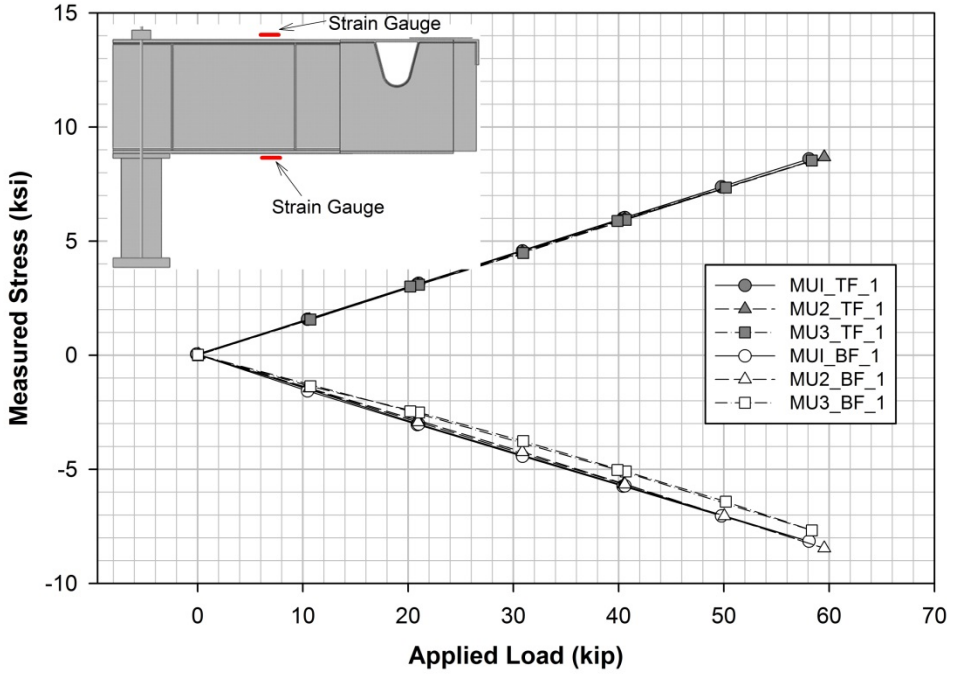

Figure 131. Comparison of measurements at strain gauges TF_1_Avg and BF_1_Avg

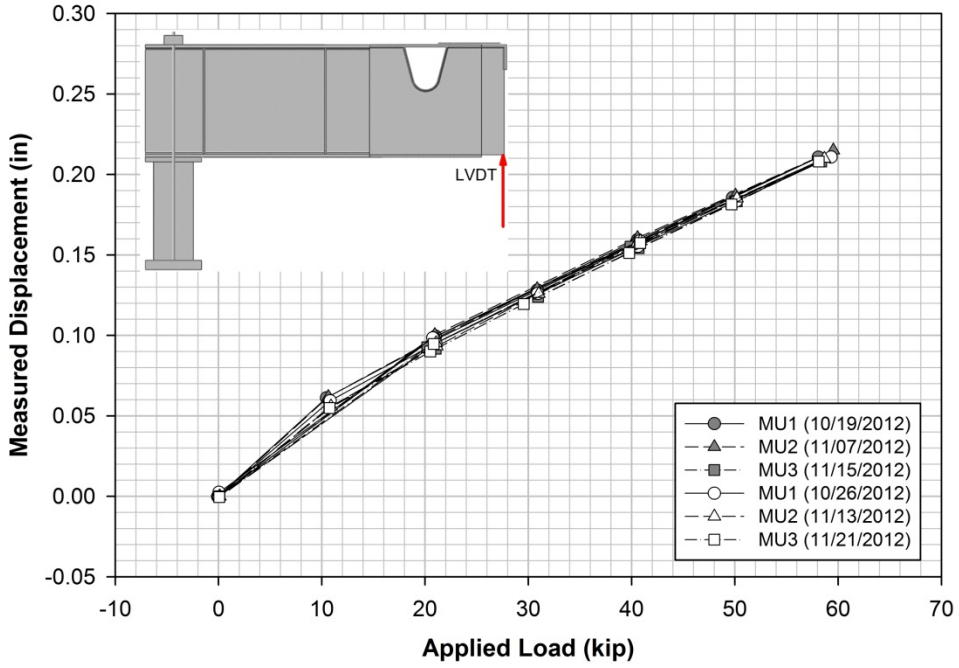

Figure 132. Comparison between measurements during the static tests before the onset of the fatigue testing and the static tests in the cracked specimen, at strain gauge DISPL_Avg

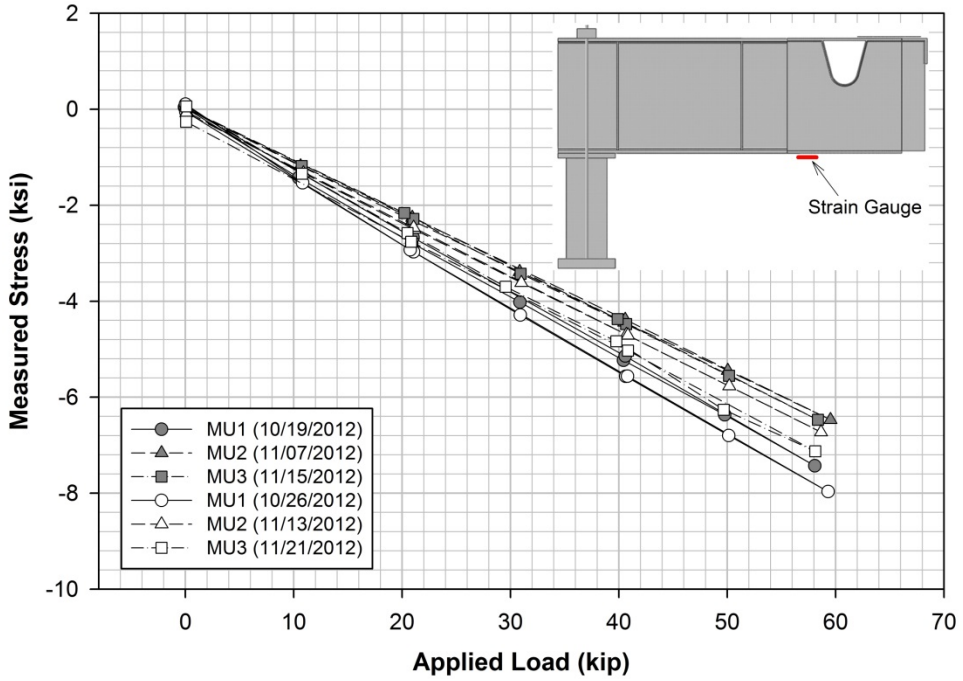

Figure 133. Comparison between measurements during the static tests before the onset of the fatigue testing and the static tests in the cracked specimen, at strain gauge BDP_WEB_Avg

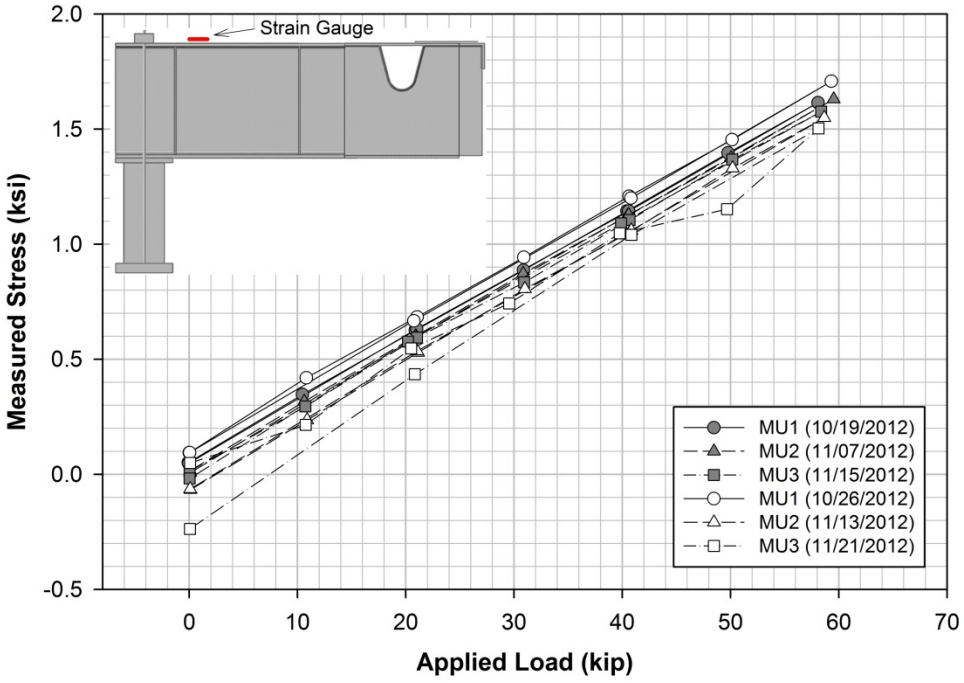

Figure 134. Comparison between measurements during the static tests before the onset of the fatigue testing and the static tests in the cracked specimen, at strain gauge TF_2_Avg

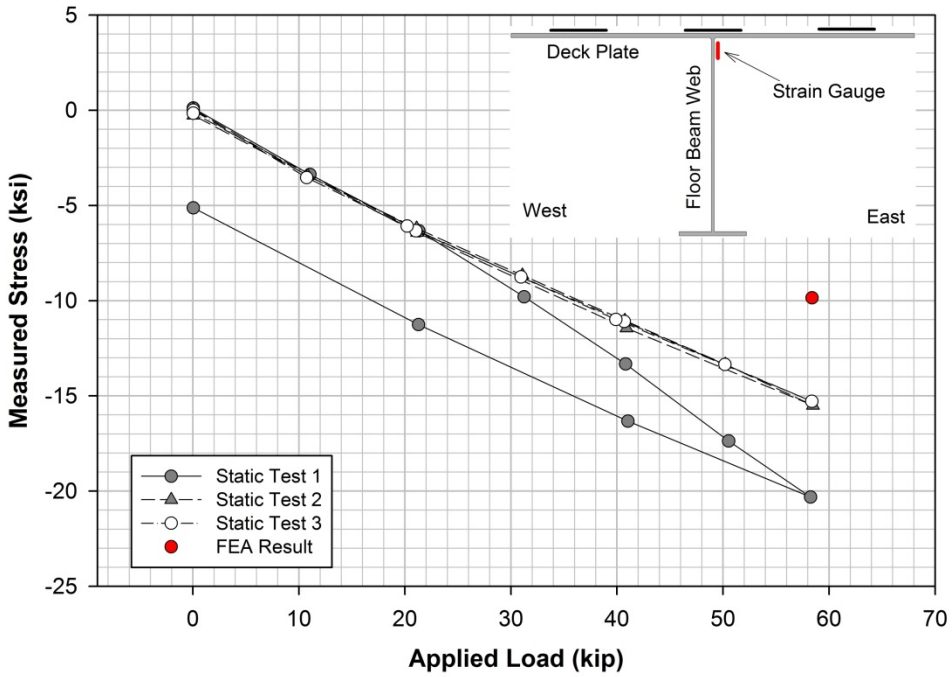

Figure 135. Measurements at strain gauge EDPFB_2_Avg in MU3

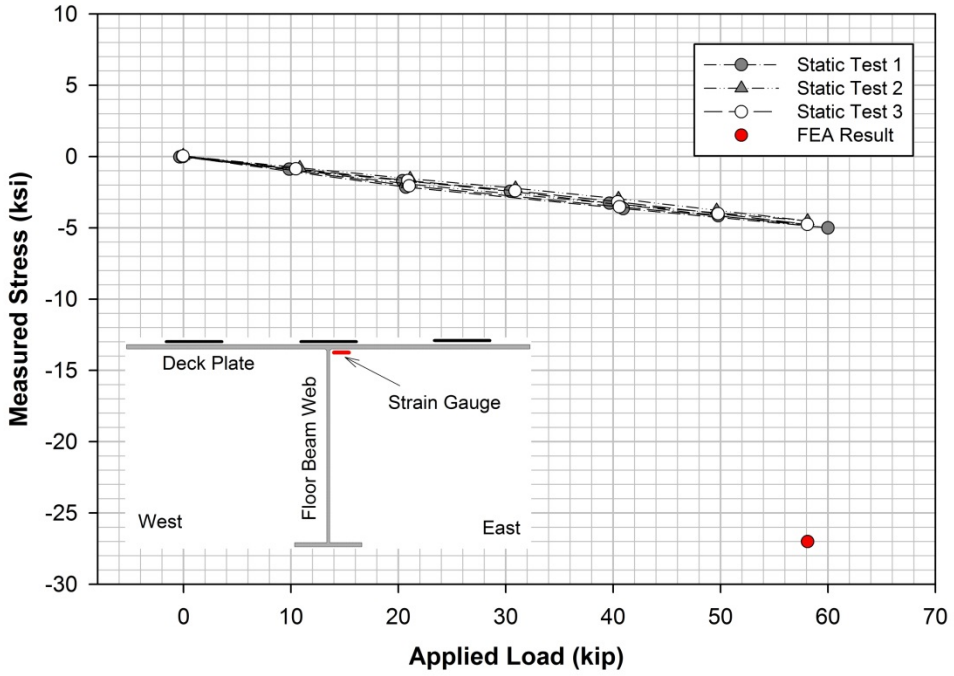

Figure 136. Measurements at strain gauge EDPFB_1_Avg in MU1

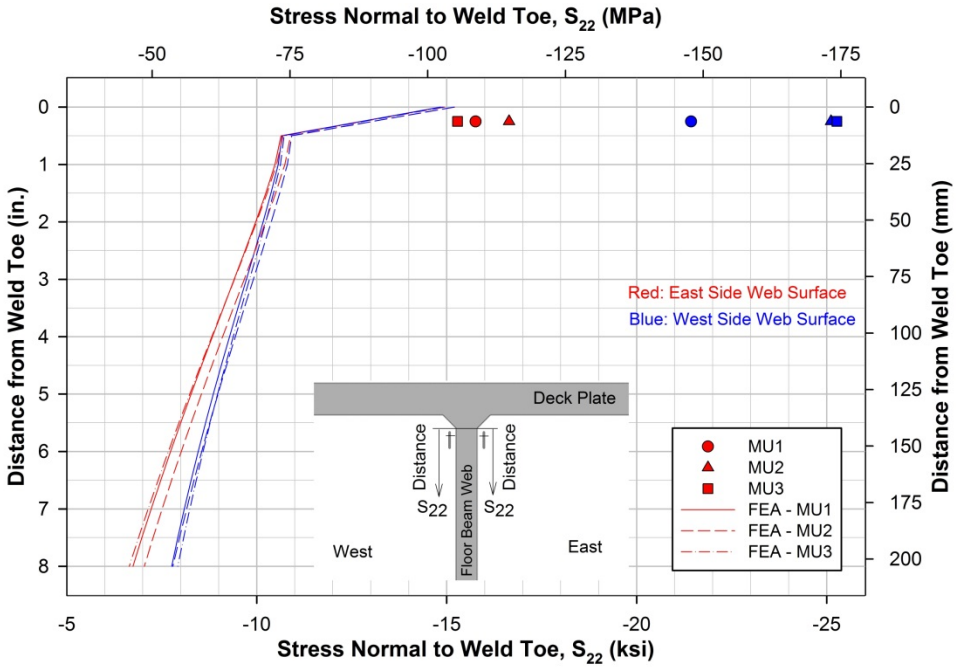

Figure 137. Comparison of measurements at strain gauges WDPFB_2_Avg and EDPFB_2_Avg

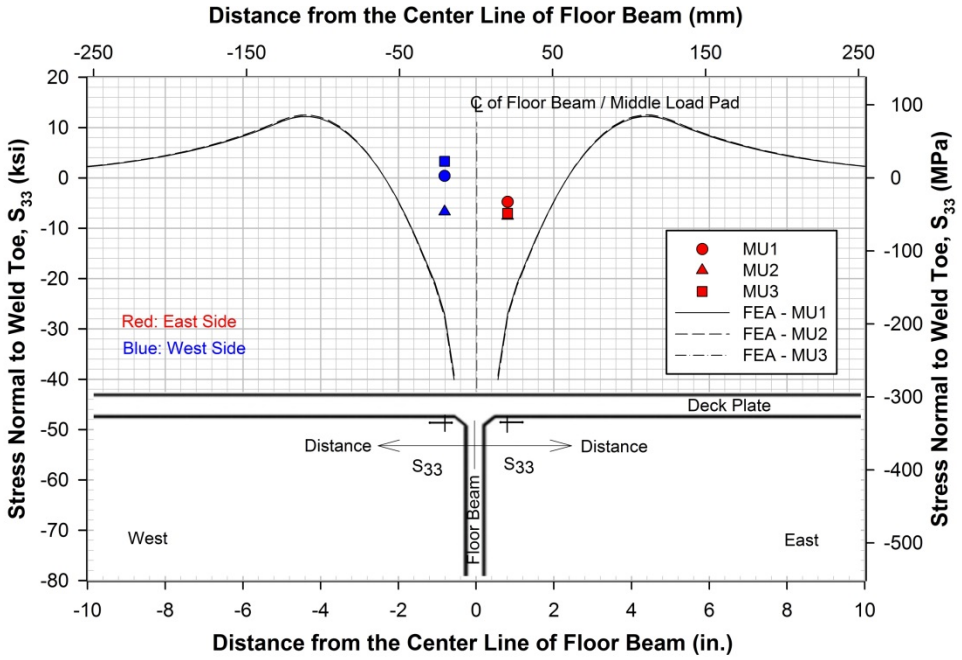

Figure 138. Comparison of measurements at strain gauges WDPFB_1_Avg and EDPFB_1_Avg

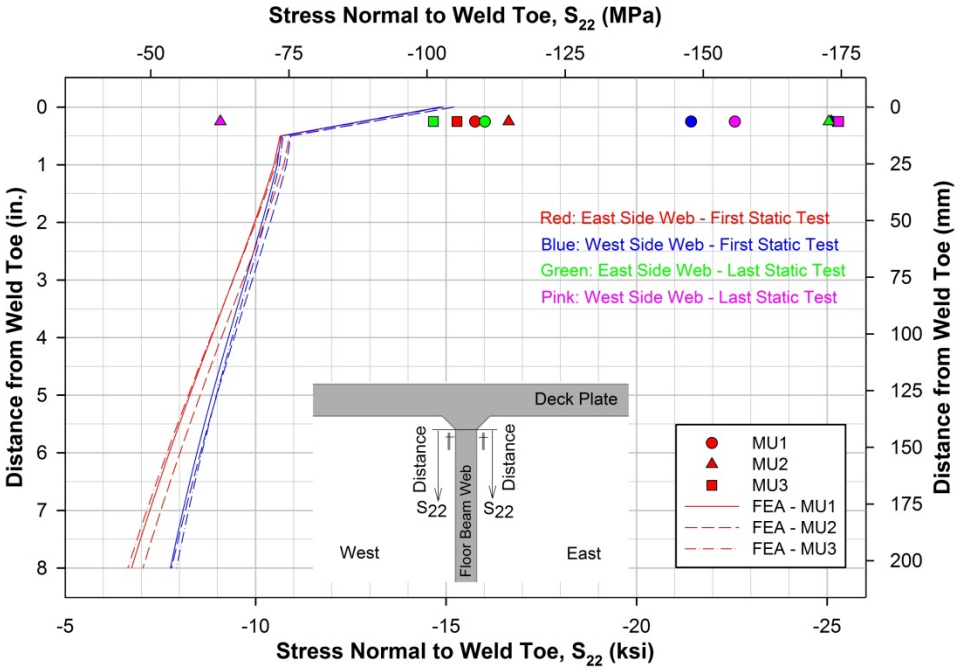

Figure 139. Comparison between measurements during the static tests before the onset of the fatigue testing and the static tests in the cracked specimen, at strain gauges WDPFB_2_Avg and EDPFB_2_Avg

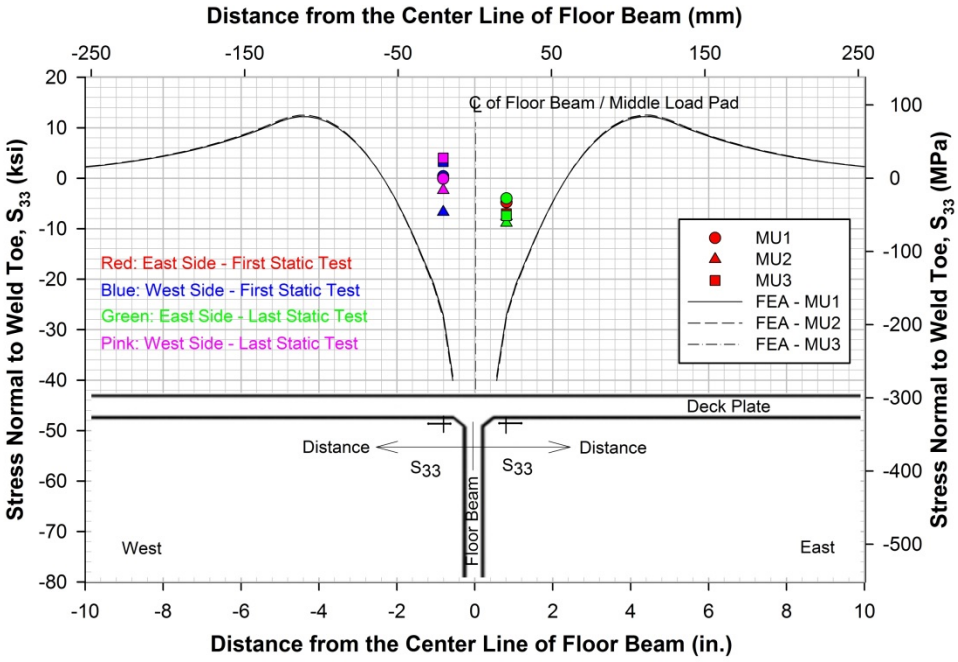

Figure 140. Comparison between measurements during the static tests before the onset of the fatigue testing and the static tests in the cracked specimen, at strain gauges WDPFB_1_Avg and EDPFB_1_Avg

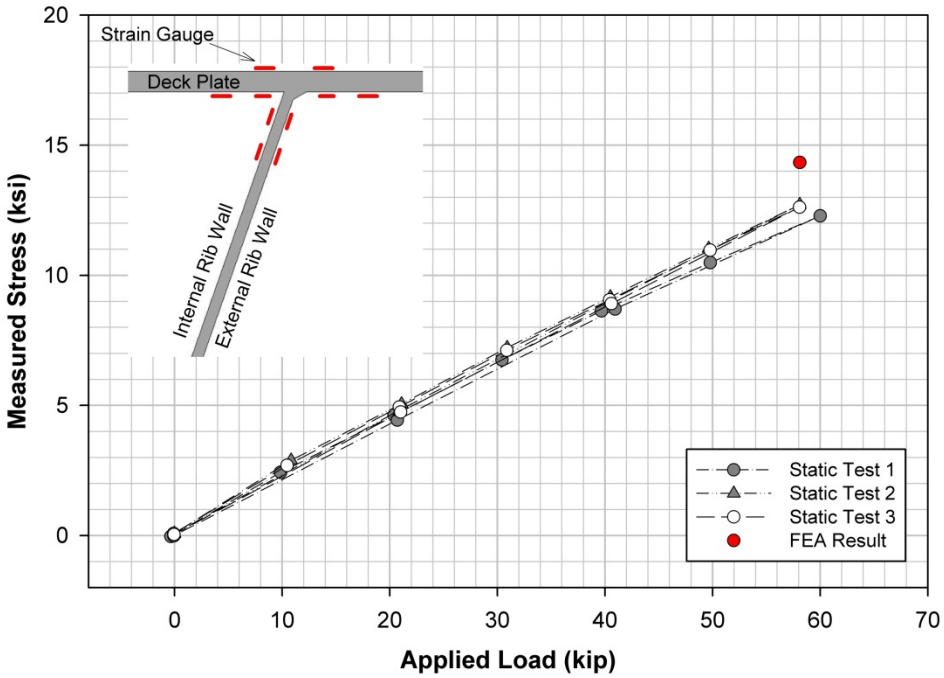

Figure 141. Measurements at strain gauge ETDP_1_Avg in MU1

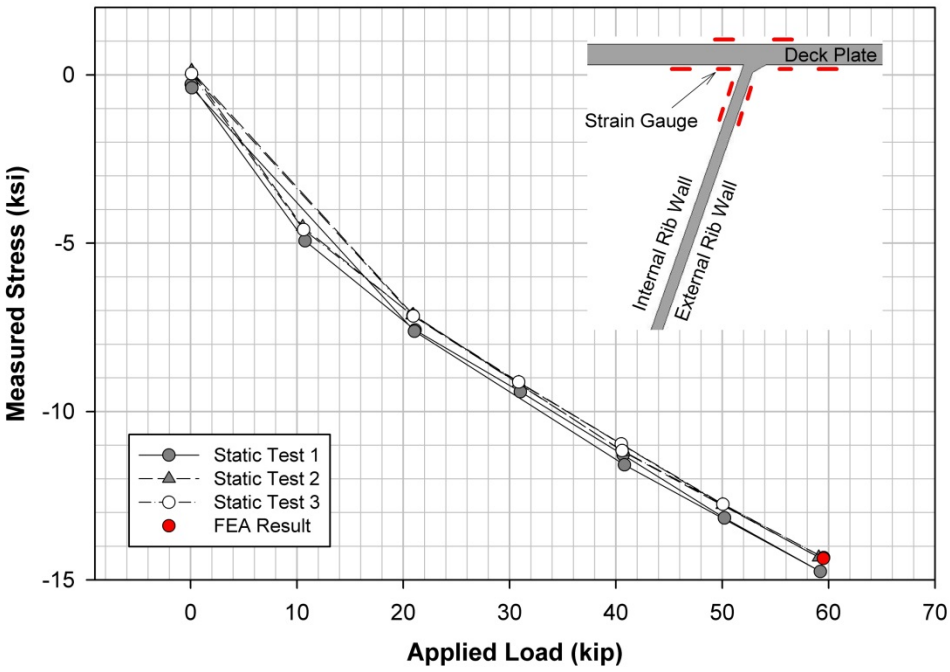

Figure 142. Measurements at strain gauge WBDP_I1_Avg in MU2

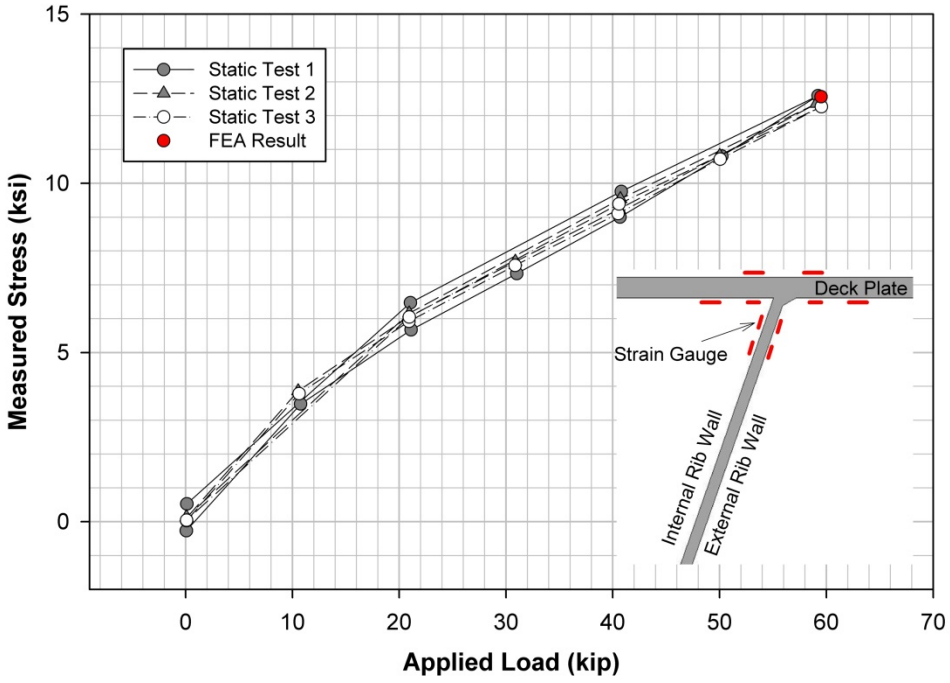

Figure 143. Measurements at strain gauge WRIB_I1_Avg in MU2

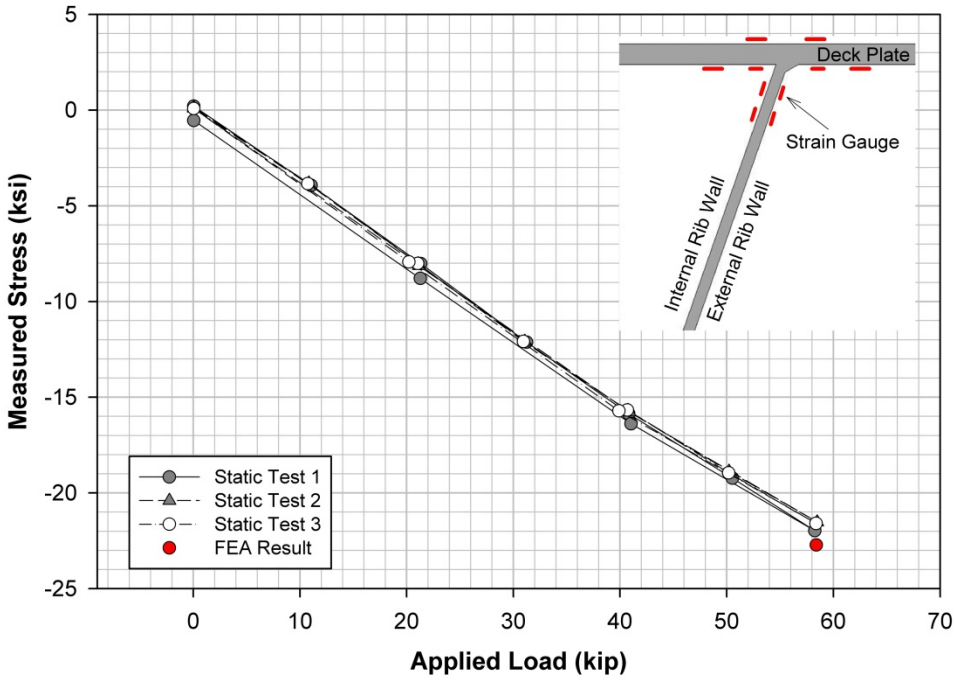

Figure 144. Measurements at strain gauge ERIB_E1_Avg in MU3

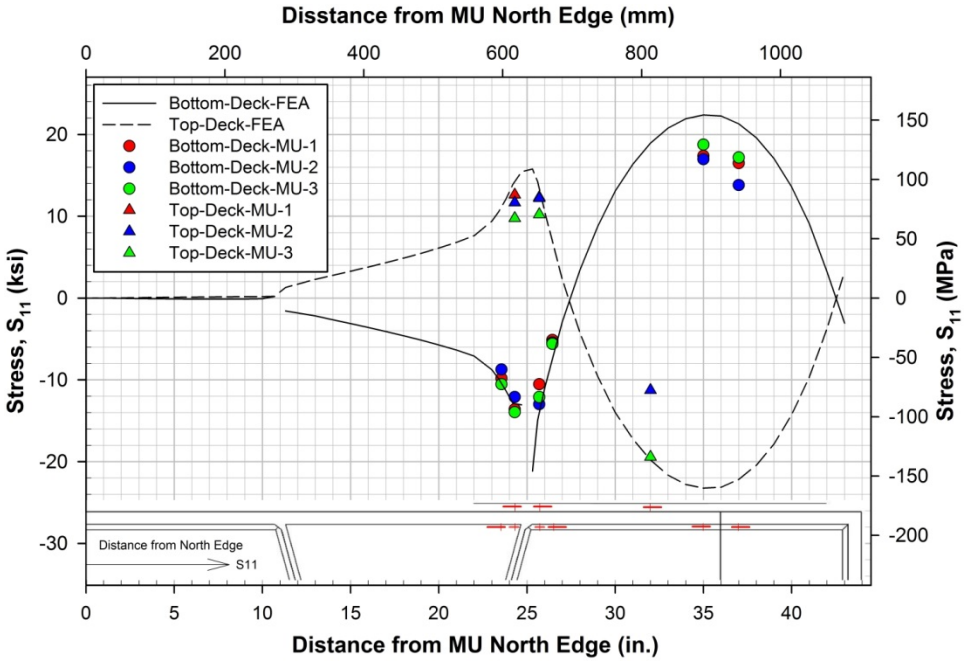

Figure 145. Comparison of measurements at strain gauges on the deck plate

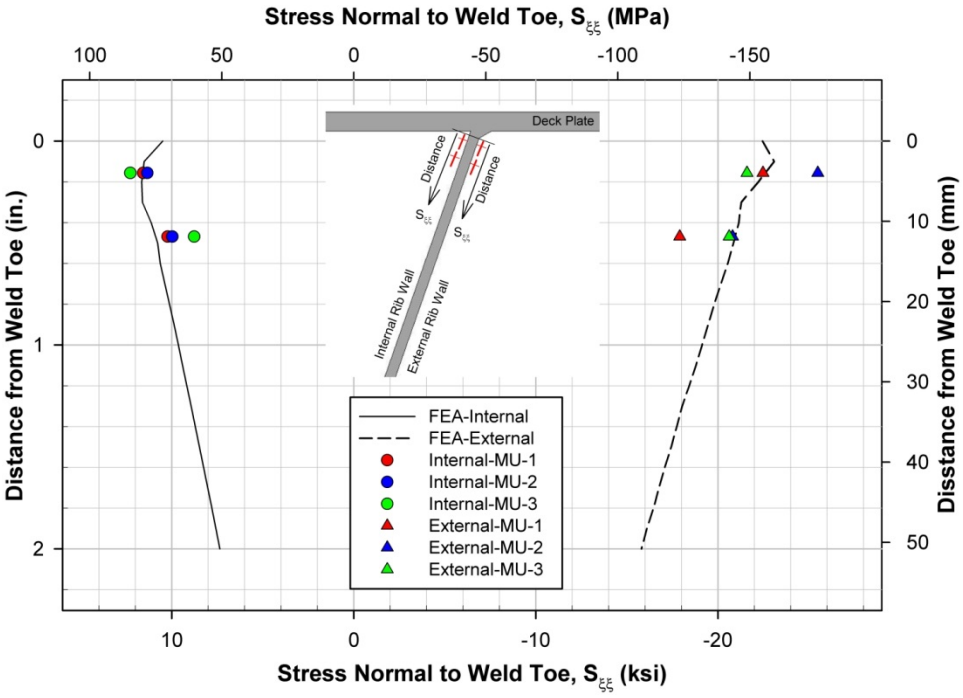

Figure 146. Comparison of measurements at strain gauges on the rib wall

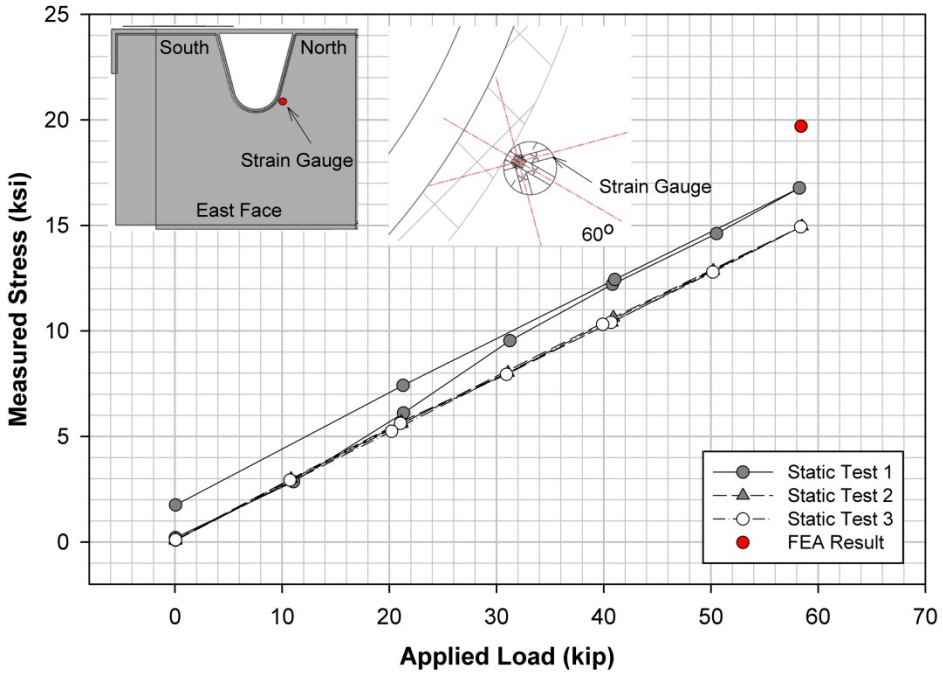

Figure 147. Measurements at strain gauge NEFB_R1_Avg in MU3

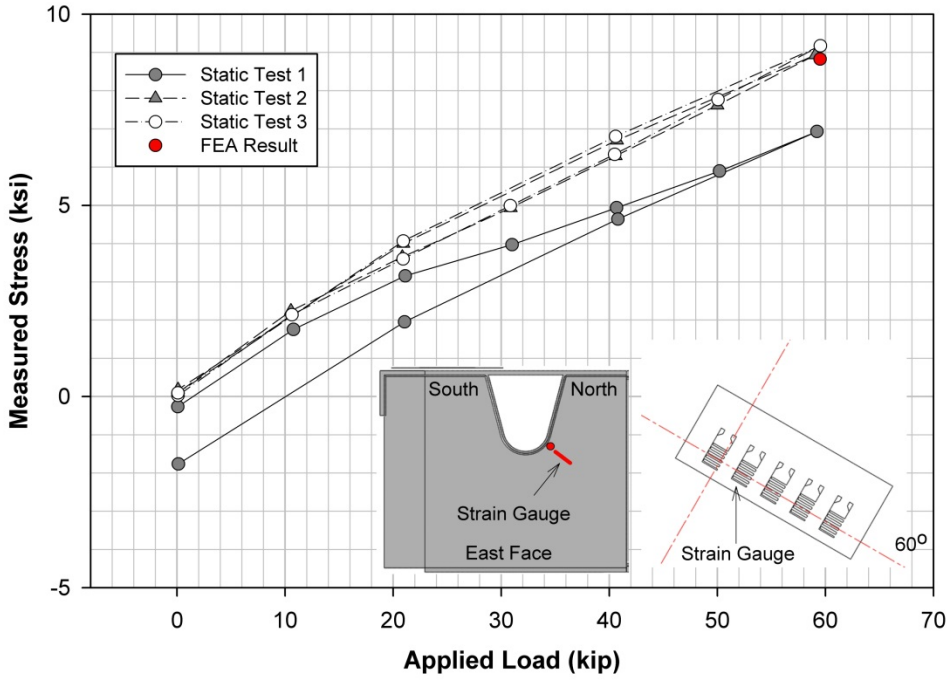

Figure 148. Measurements at strain gauge NEFB_S2_Avg in MU2

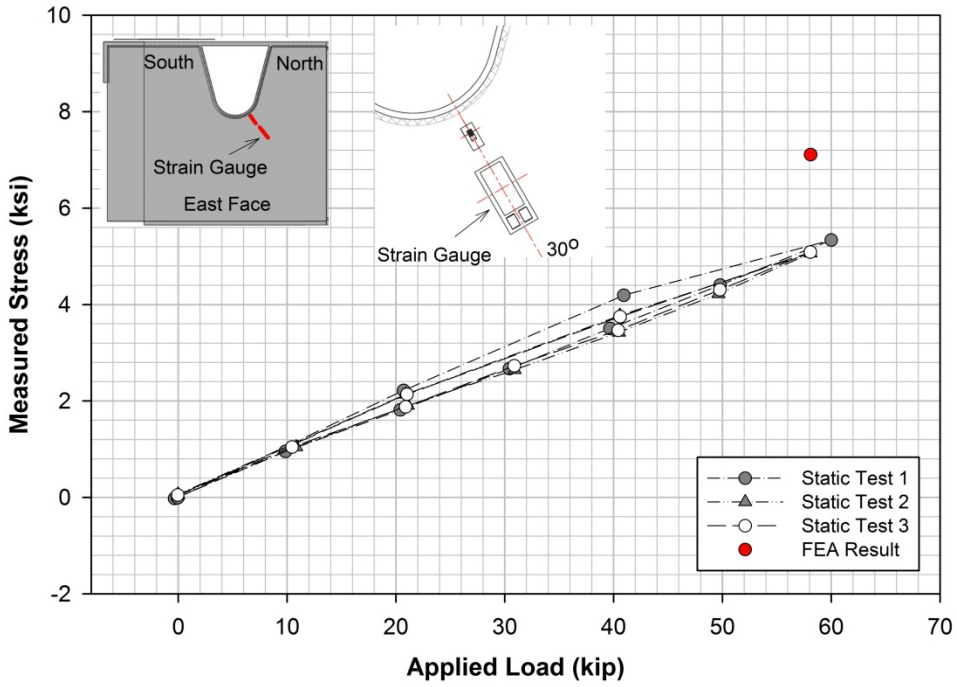

Figure 149. Measurements at strain gauge NEFB_30_2_Avg in MU1

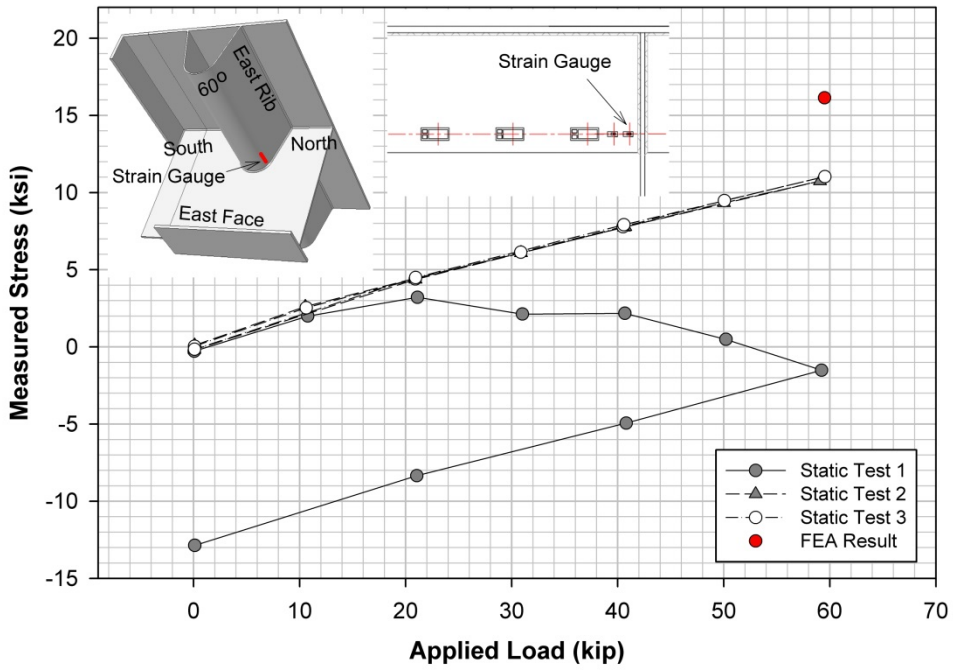

Figure 150. Measurements at strain gauge NER_60_1_Avg in MU2

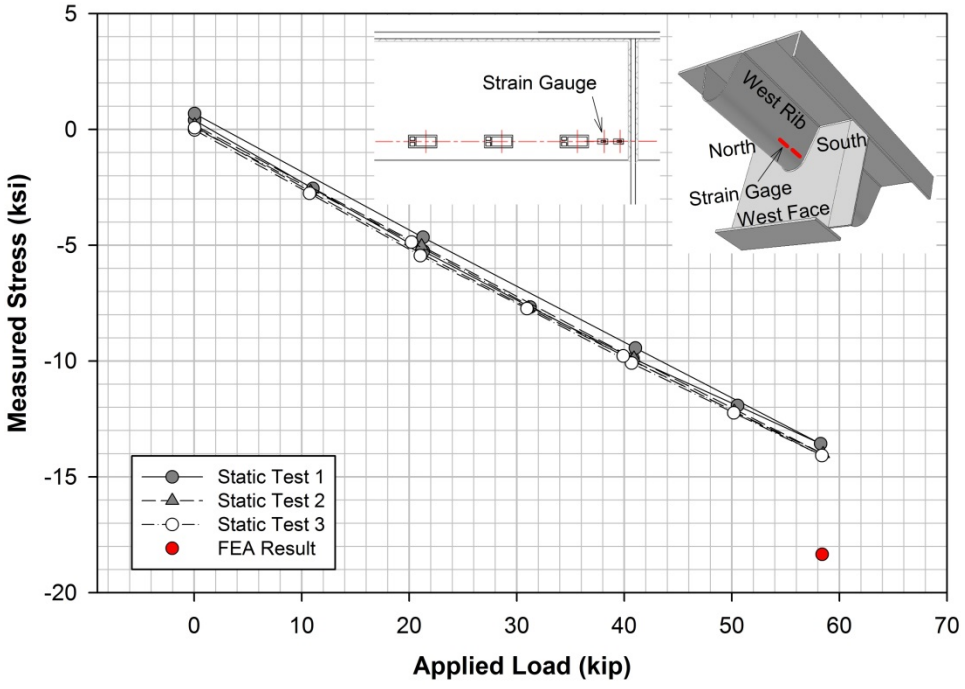

Figure 151. Measurements at strain gauge SWR_60_2_Avg in MU3

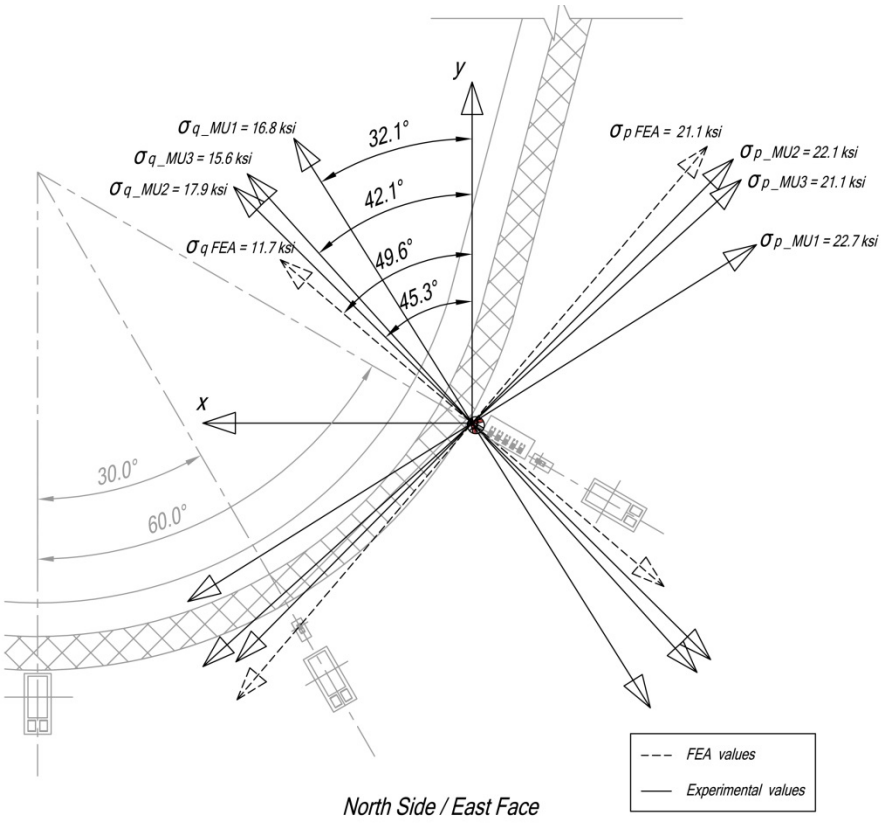

Figure 152. Comparison of FEA and measured principal stresses on the north-east rosette gauge on the floor beam

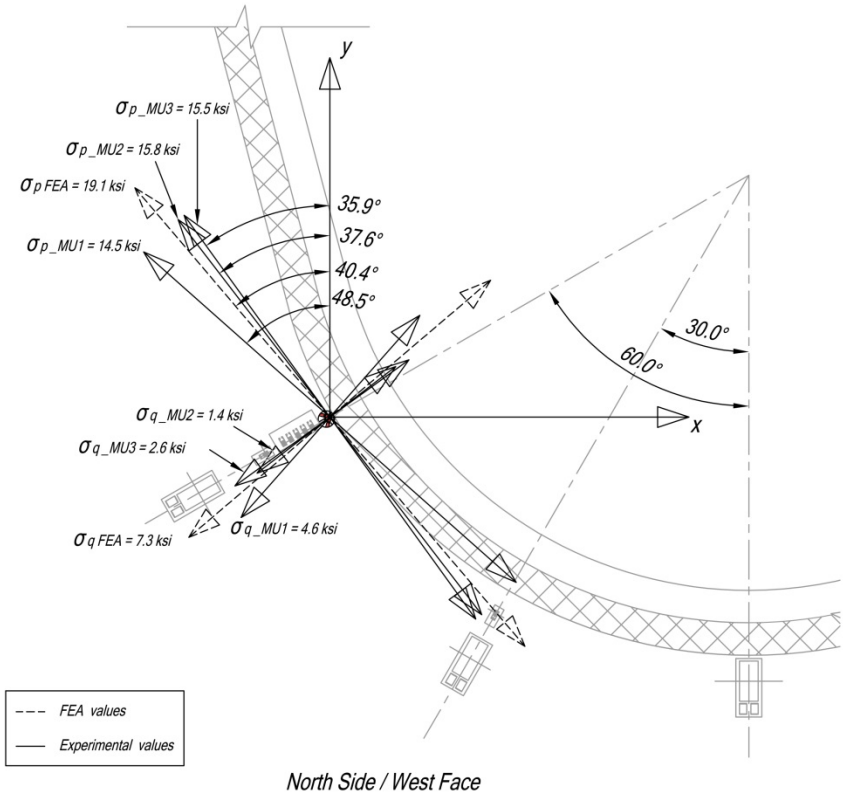

Figure 153. Comparison of FEA and measured principal stresses on the north-west rosette gauge on the floor beam

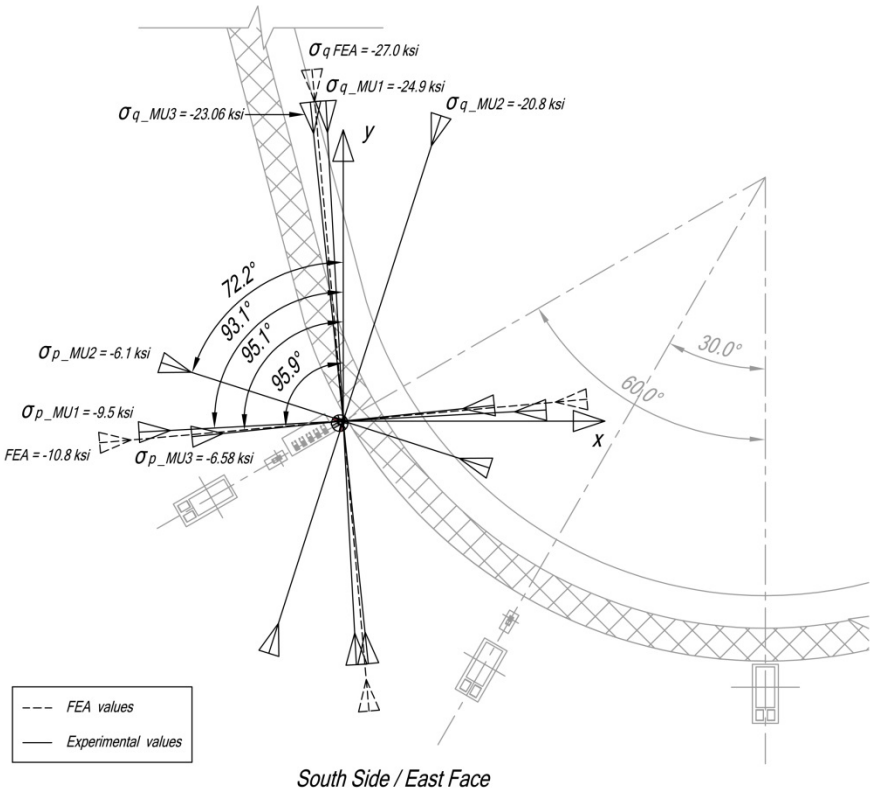

Figure 154. Comparison of FEA and measured principal stresses on the south-east rosette gauge on the floor beam

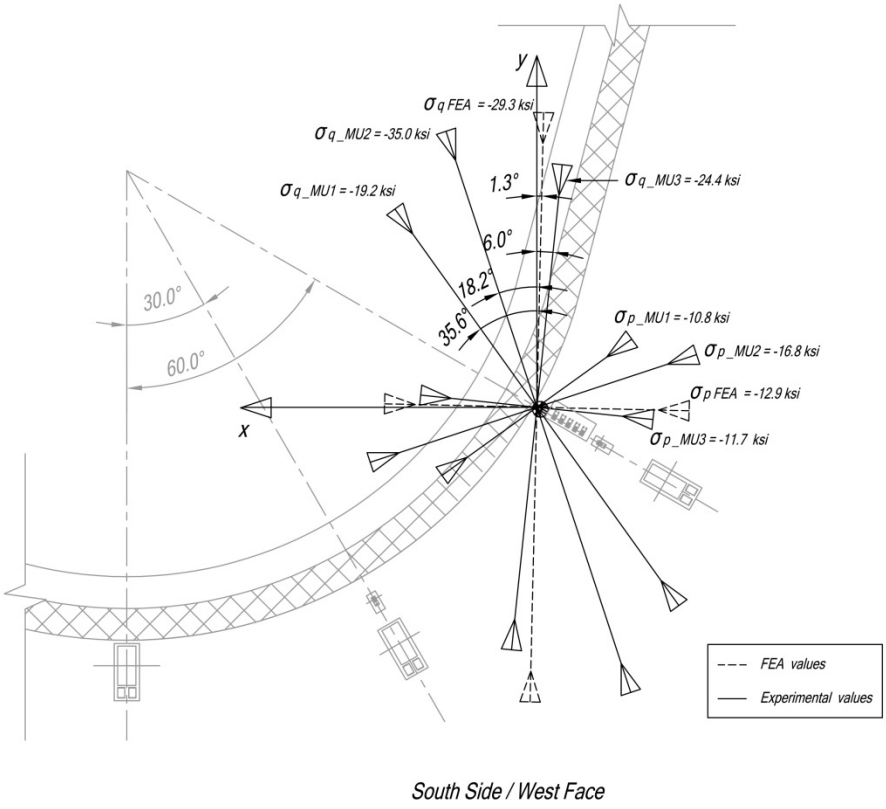

Figure 155. Comparison of FEA and measured principal stresses on the south-west rosette gauge on the floor beam

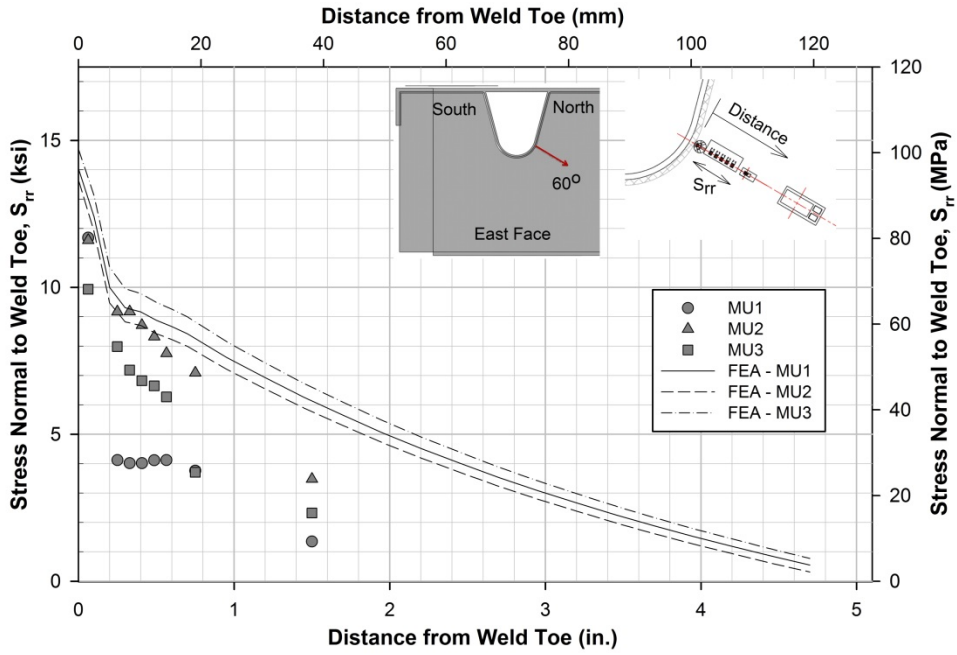

Figure 156. Comparison of FEA and measured stresses on the east face of the floor beam along a path at 60 degrees from the rib soffit to the north of the rib

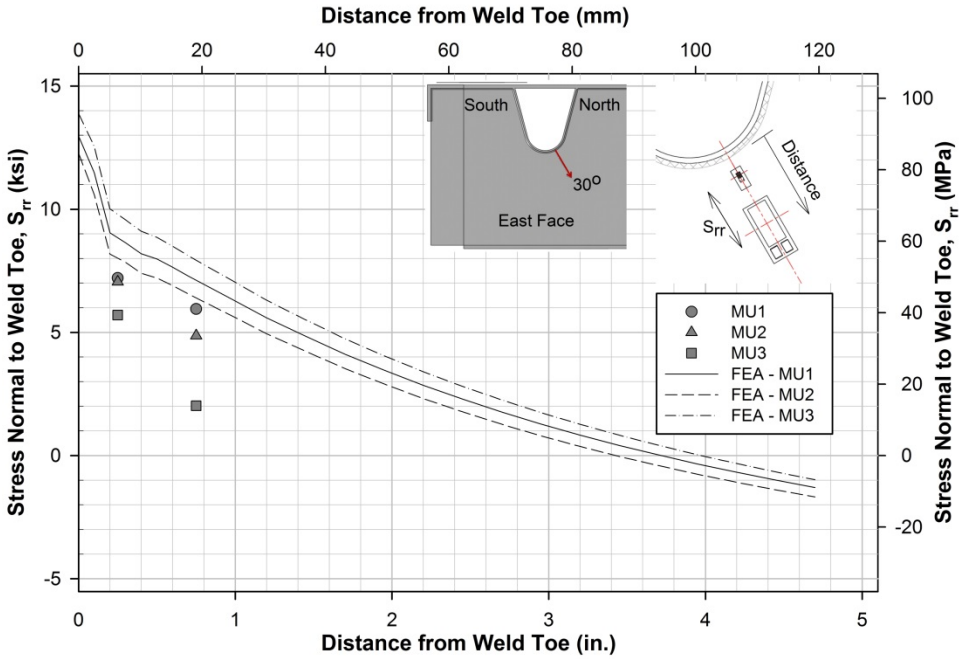

Figure 157. Comparison of FEA and measured stresses on the east face of the floor beam along a path at 30 degrees from the rib soffit to the north of the rib

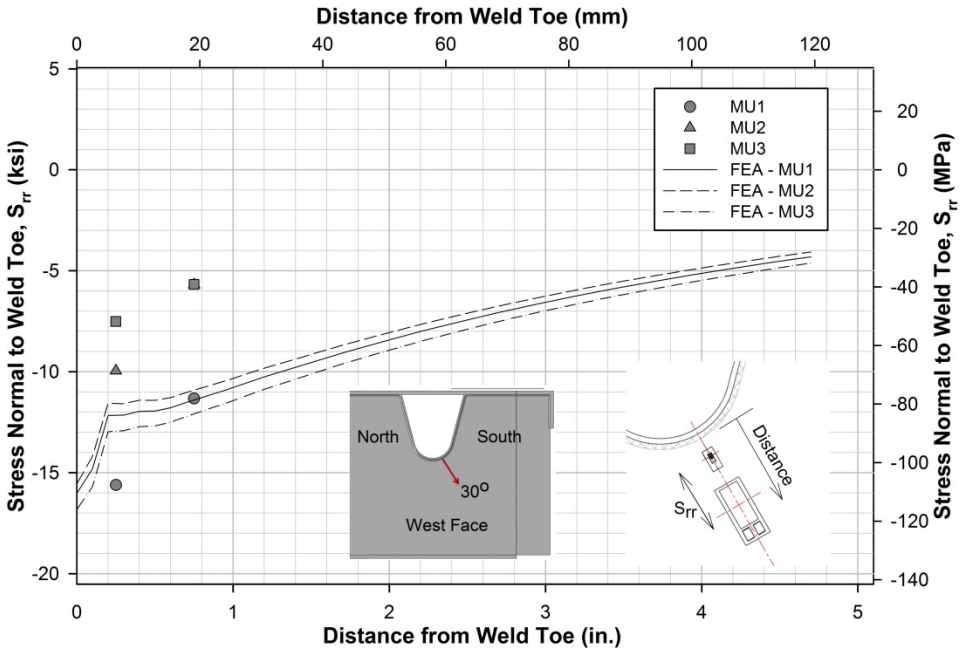

Figure 158. Comparison of FEA and measured stresses on the west face of the floor beam along a path at 30 degrees from the rib soffit to the south of the rib

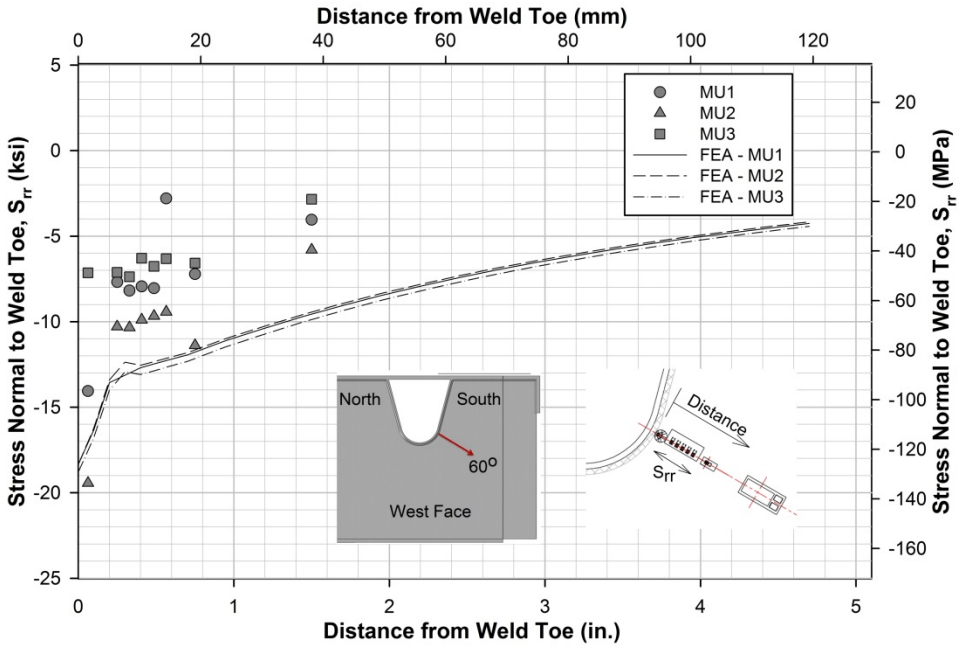

Figure 159. Comparison of FEA and measured stresses on the west face of the floor beam along a path at 60 degrees from the rib soffit to the south of the rib

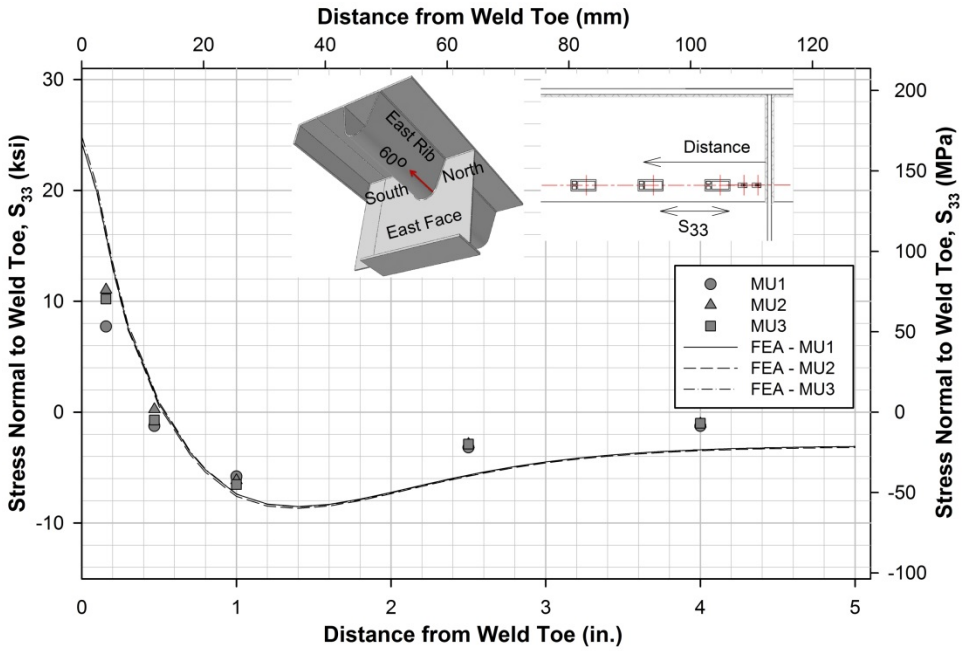

Figure 160. Comparison of FEA and measured stresses on the outer face of the rib wall along a path at 60 degrees north from the rib soffit to the east of floor beam

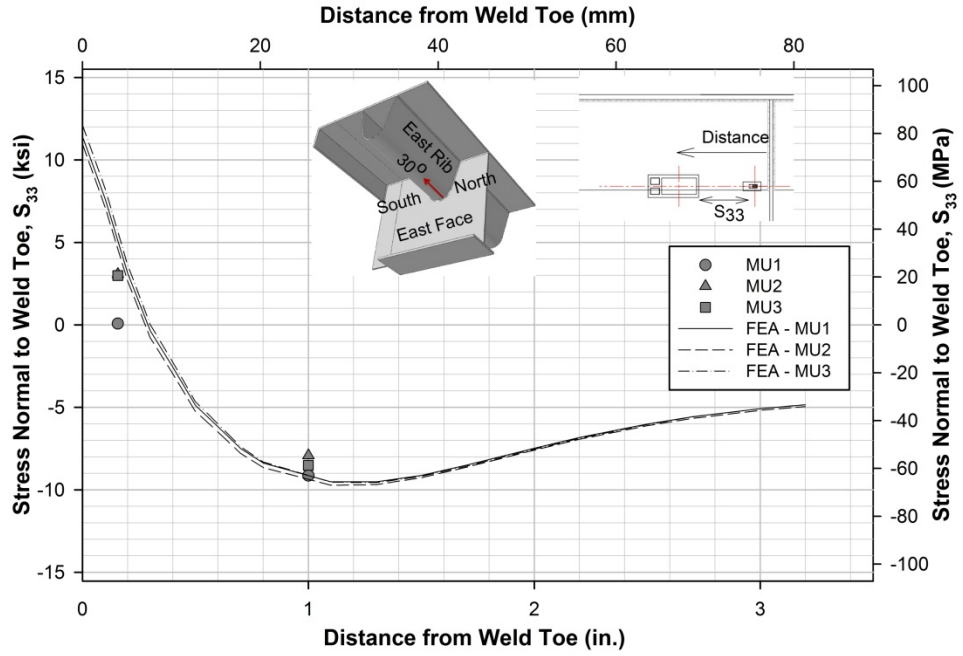

Figure 161. Comparison of FEA and measured stresses on the outer face of the rib wall along a path at 30 degrees north from the rib soffit to the east of floor beam

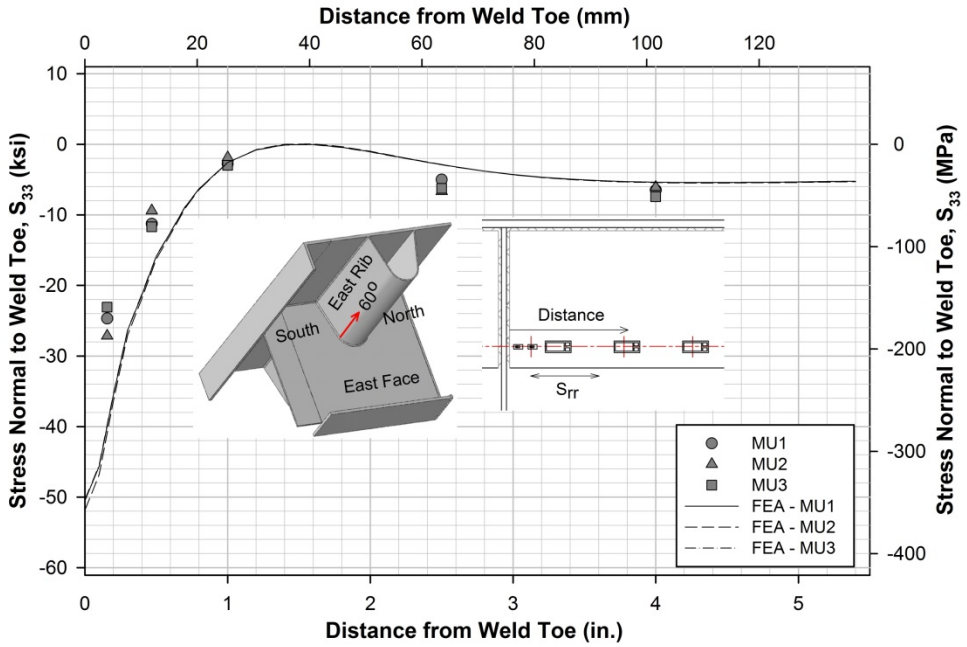

Figure 162. Comparison of FEA and measured stresses on the outer face of the rib wall along a path at 60 degrees south from the rib soffit to the east of floor beam

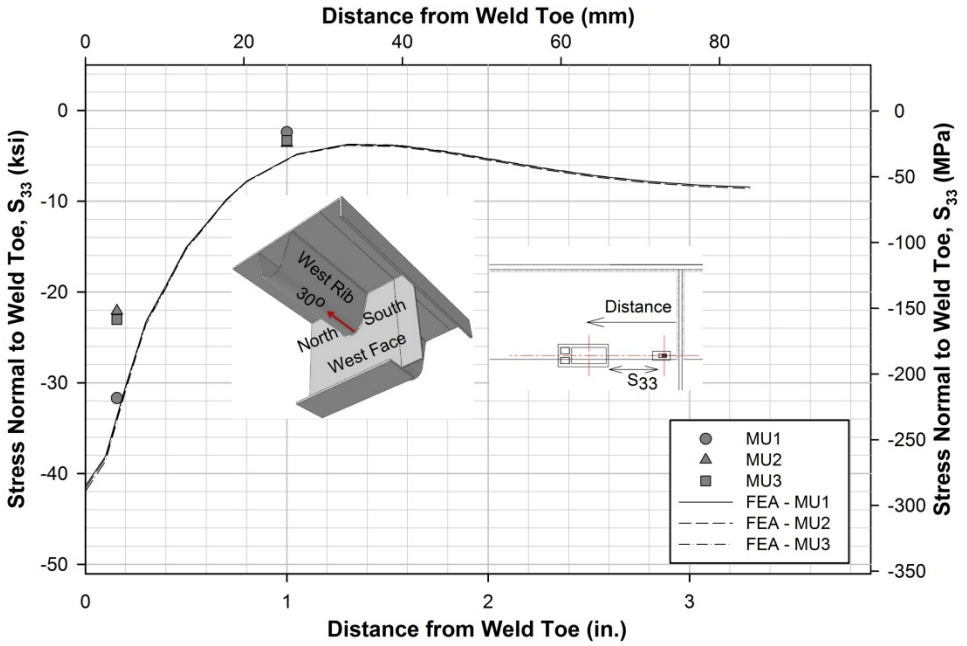

Figure 163. Comparison of FEA and measured stresses on the outer face of the rib wall along a path at 30 degrees south from the rib soffit to the west of floor beam

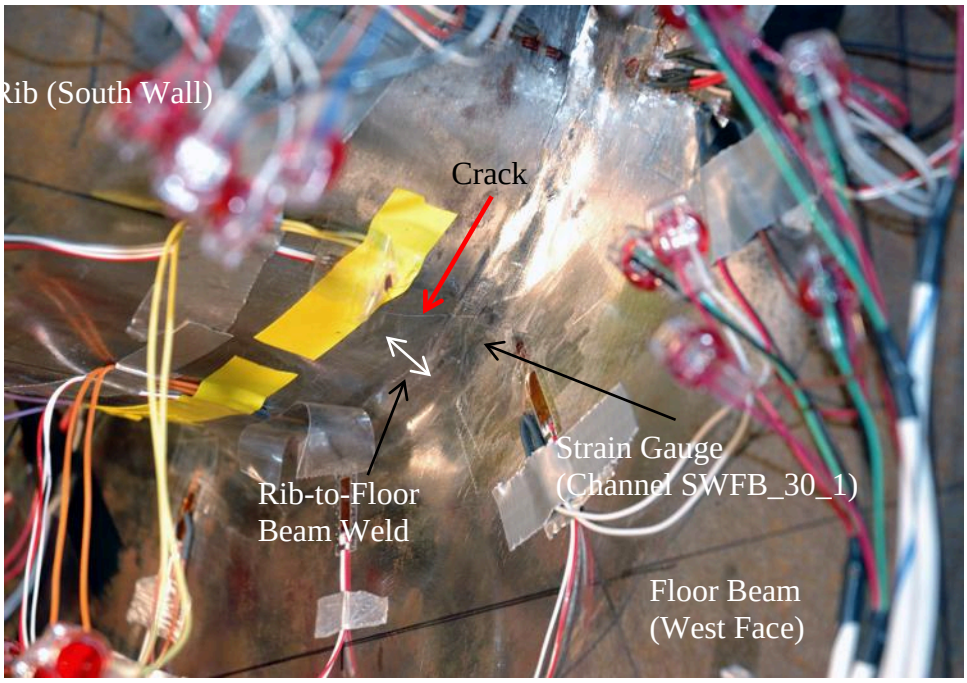

Figure 164. Crack at the floor beam-to-rib welded connection in the mock-up specimen MU1 – south west

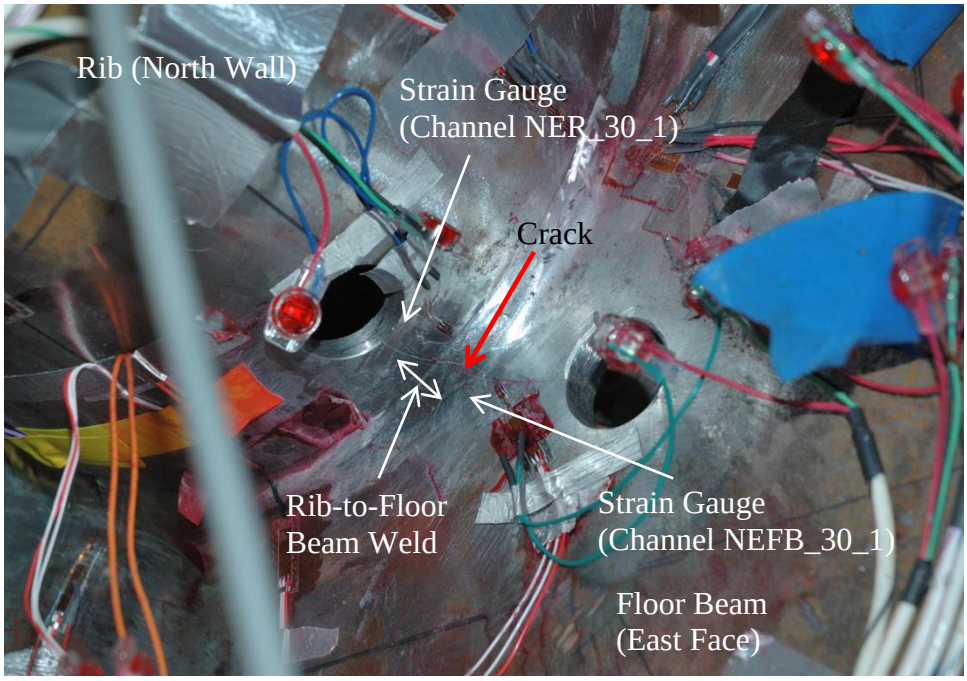

Figure 165. Crack at the floor beam-to-rib welded connection in the mock-up specimen MU1 – north east

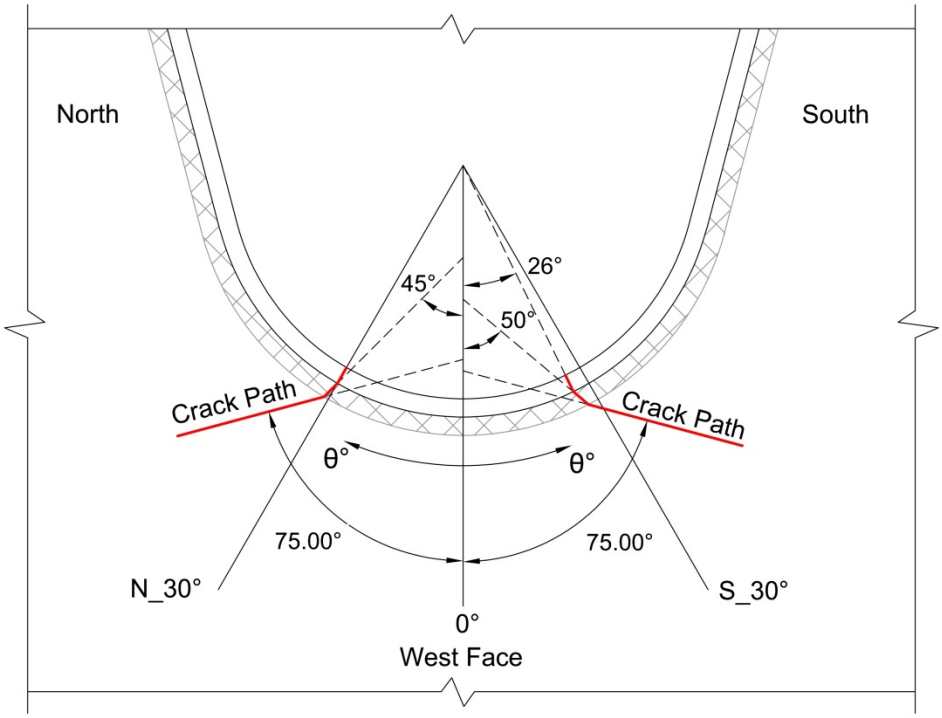

Figure 166. Schematics of cracks in mock-up specimen MU1

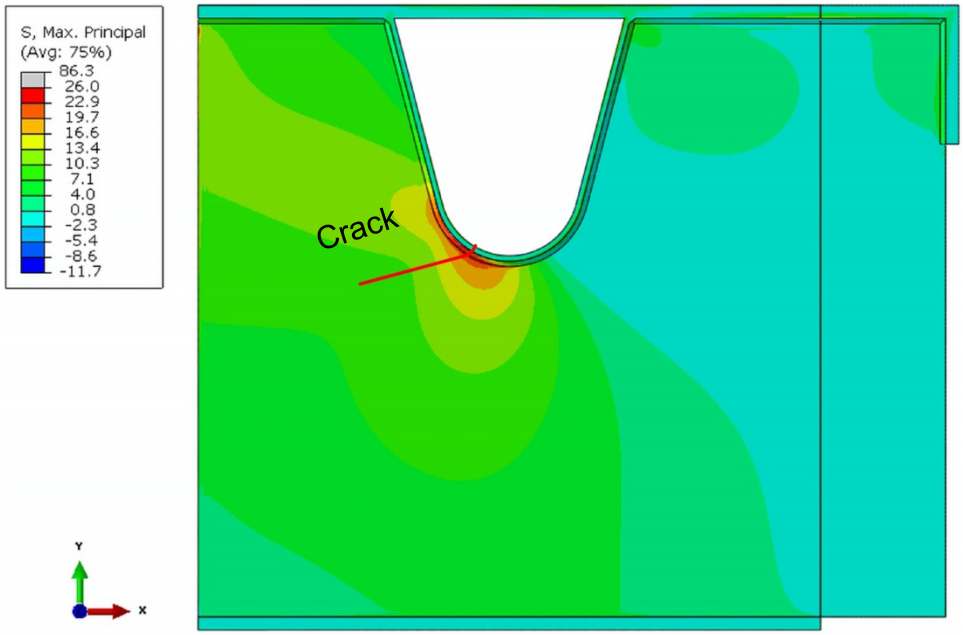

Figure 167. FEA contour of maximum principal stress in the floor beam web in MU1

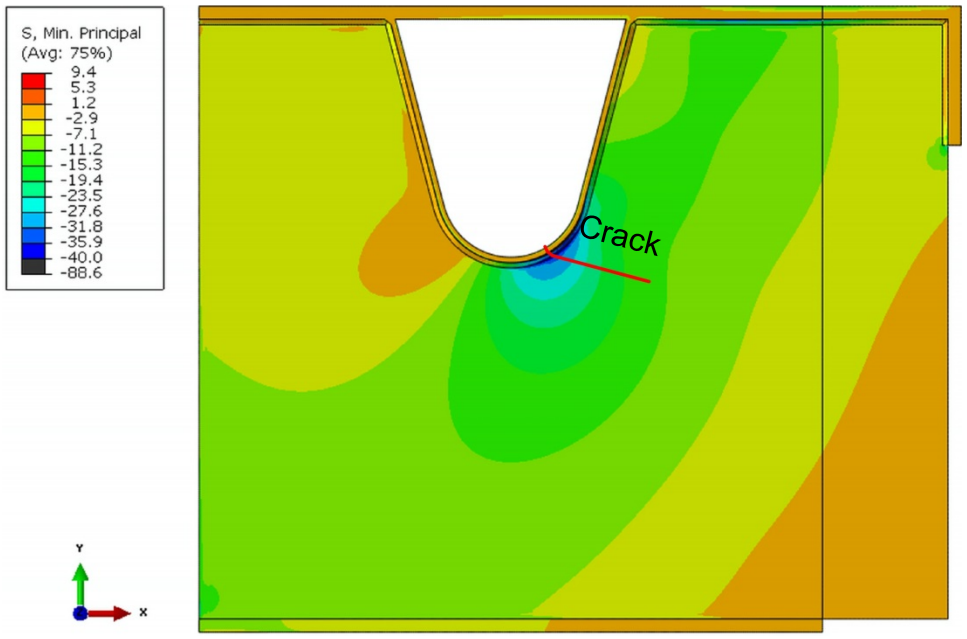

Figure 168. FEA contour of maximum principal stress in the floor beam web in MU1

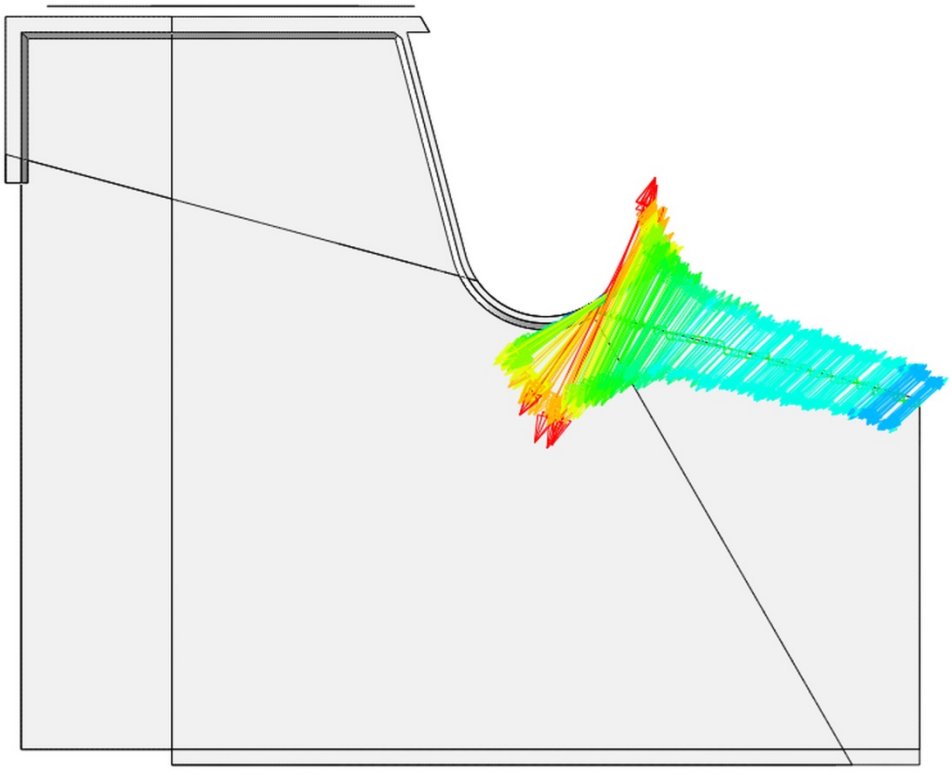

Figure 169. Direction of maximum principal stress in the floor beam web along the crack path to the north of rib in MU1 as obtained from FEA

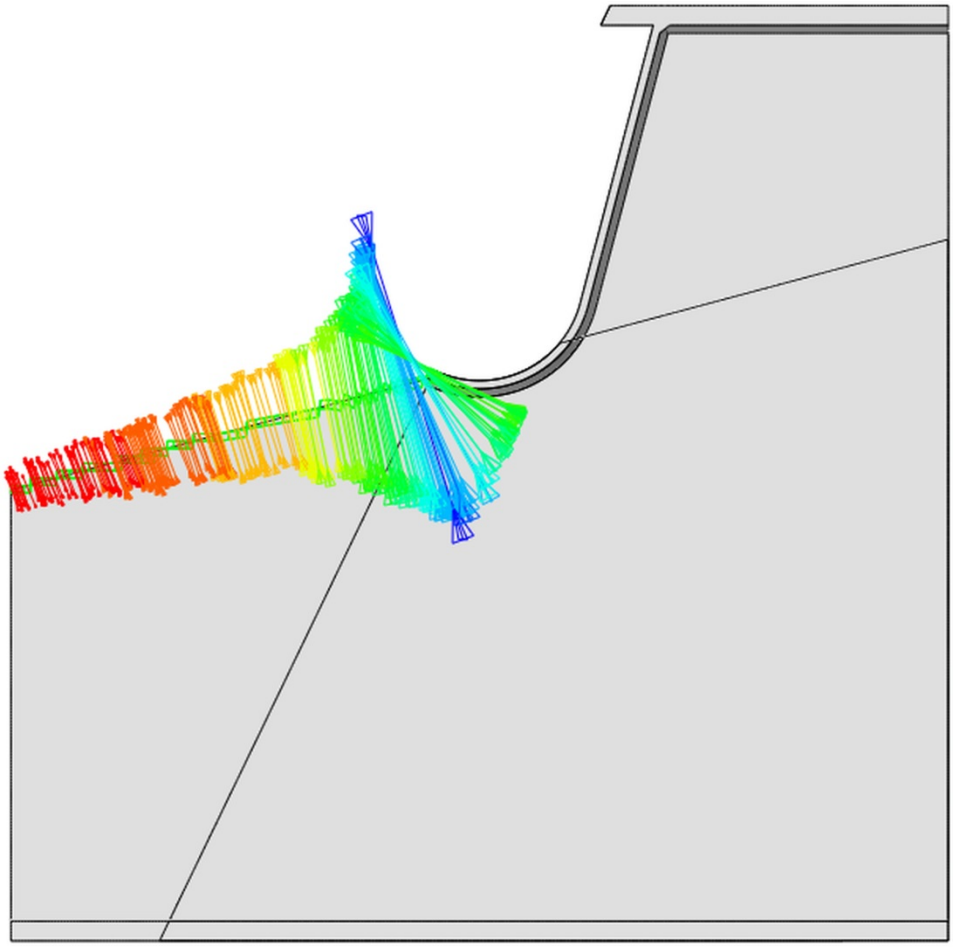

Figure 170. Direction of minimum principal stress in the floor beam web along the crack path to the south of rib in MU1 as obtained from FEA

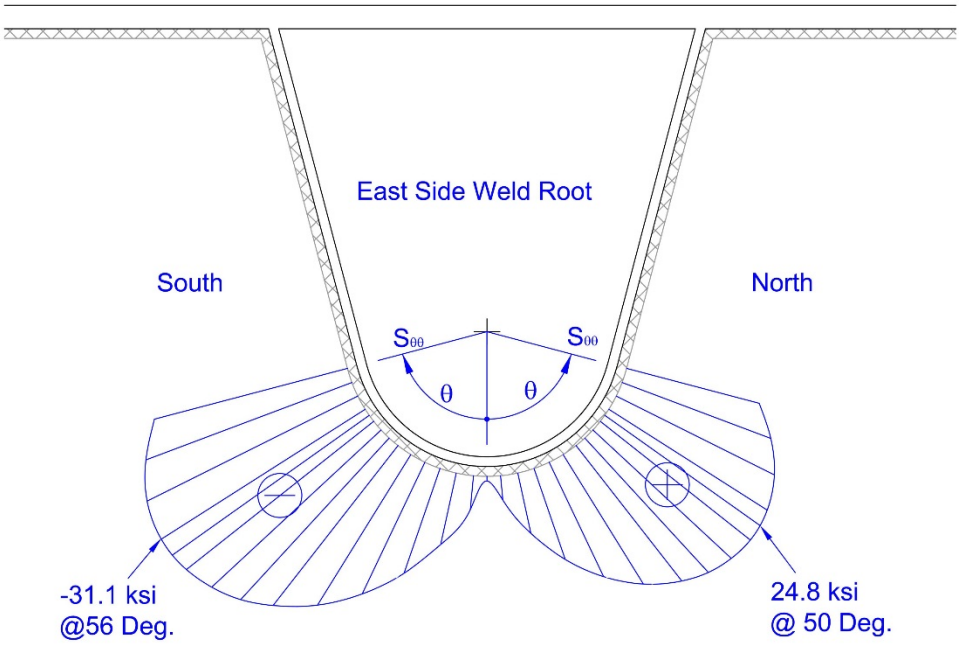

Figure 171. Distribution of circumferential stress (tangential to weld toe) at the rib-to-floor beam weld root along circumferential path through the weld root

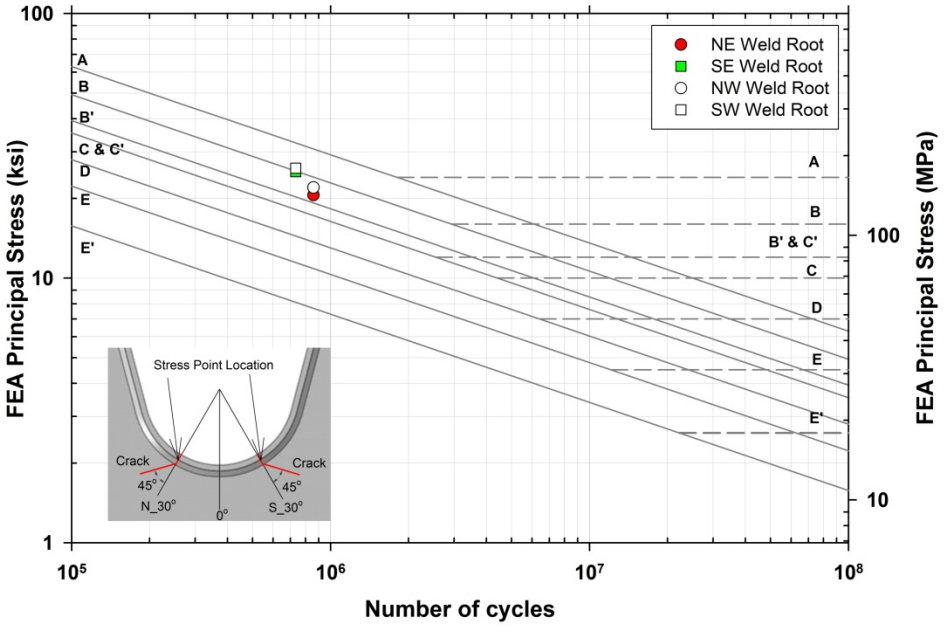

Figure 172. Fatigue test results for the rib-to-floor beam welds in MU1

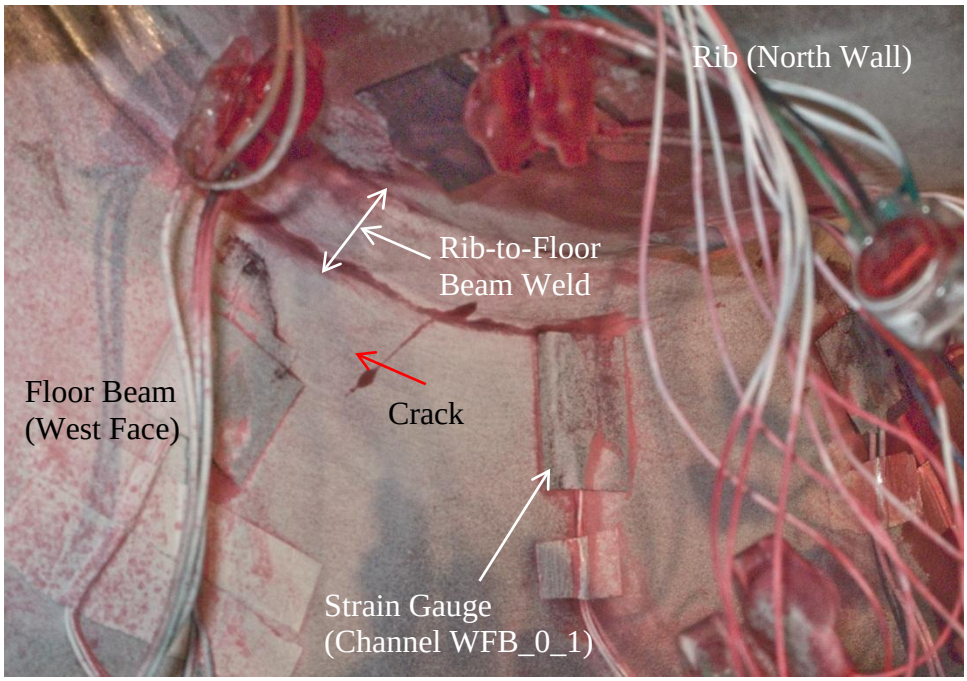

Figure 173. Crack at the floor beam-to-rib welded connection in the mock-up specimen MU2 – north west

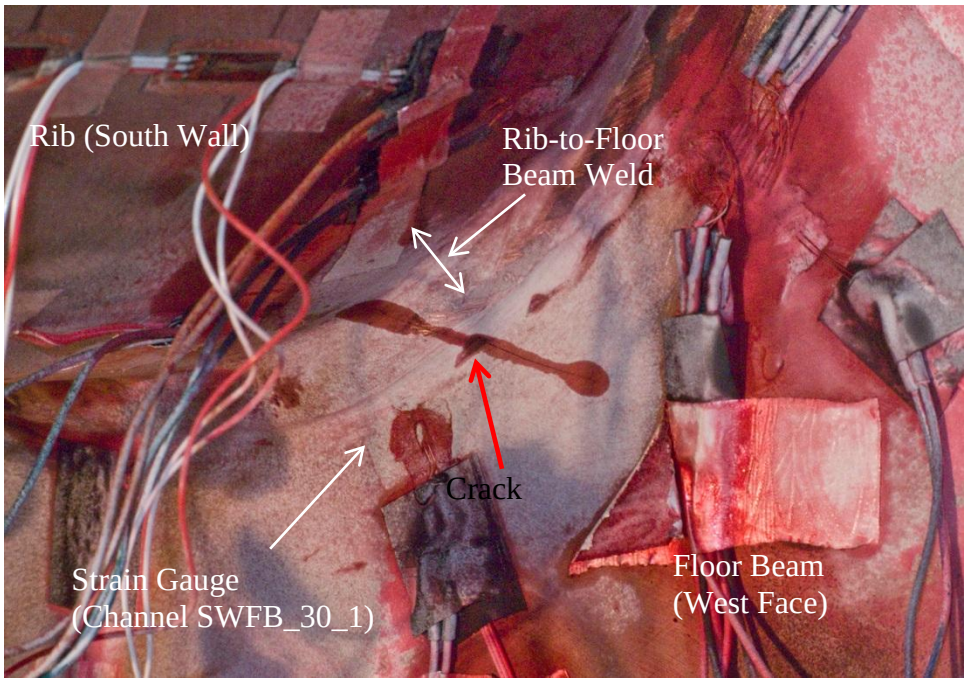

Figure 174. Crack at the floor beam-to-rib welded connection in the mock-up specimen MU2 – south west

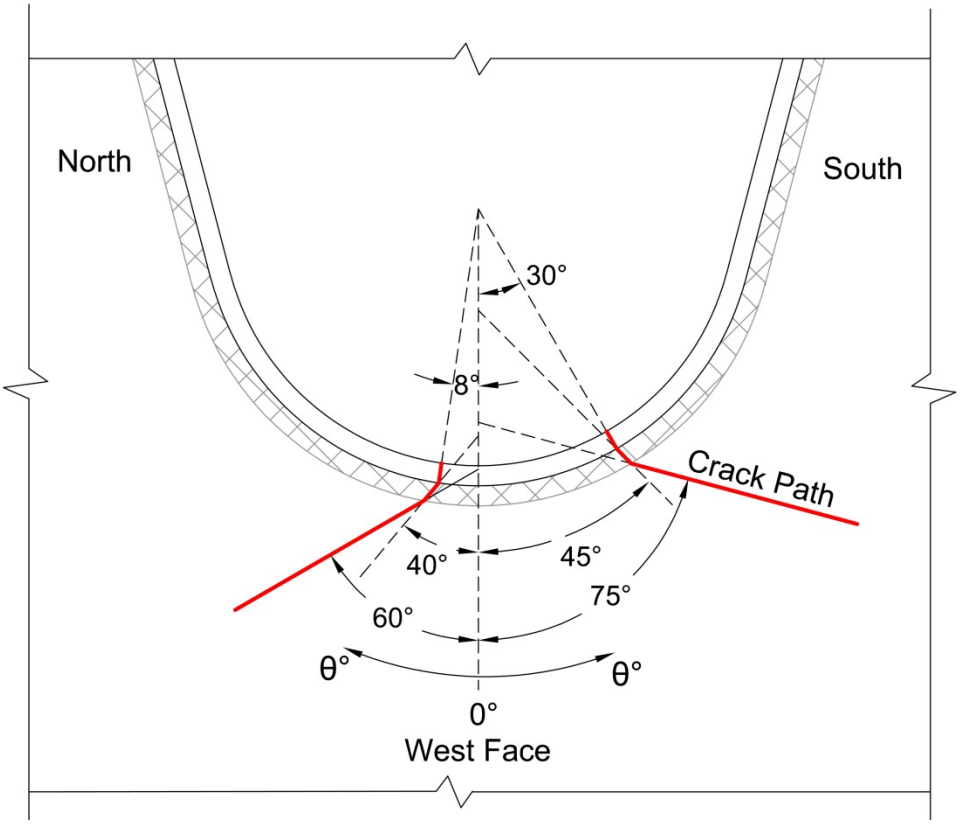

Figure 175. Schematics of cracks in mock-up specimen MU2

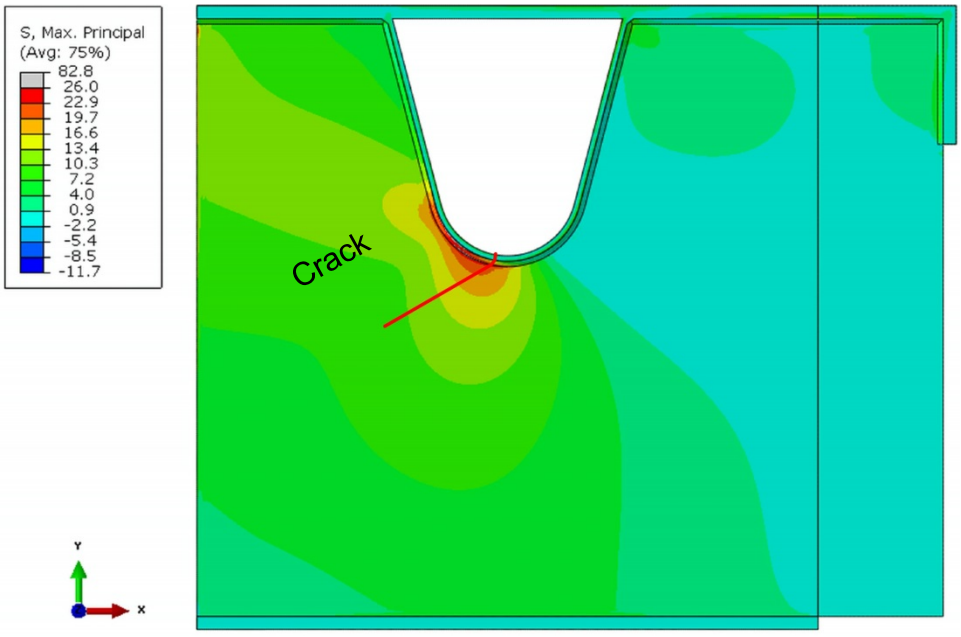

Figure 176. FEA contour of maximum principal stress in the floor beam web in MU2

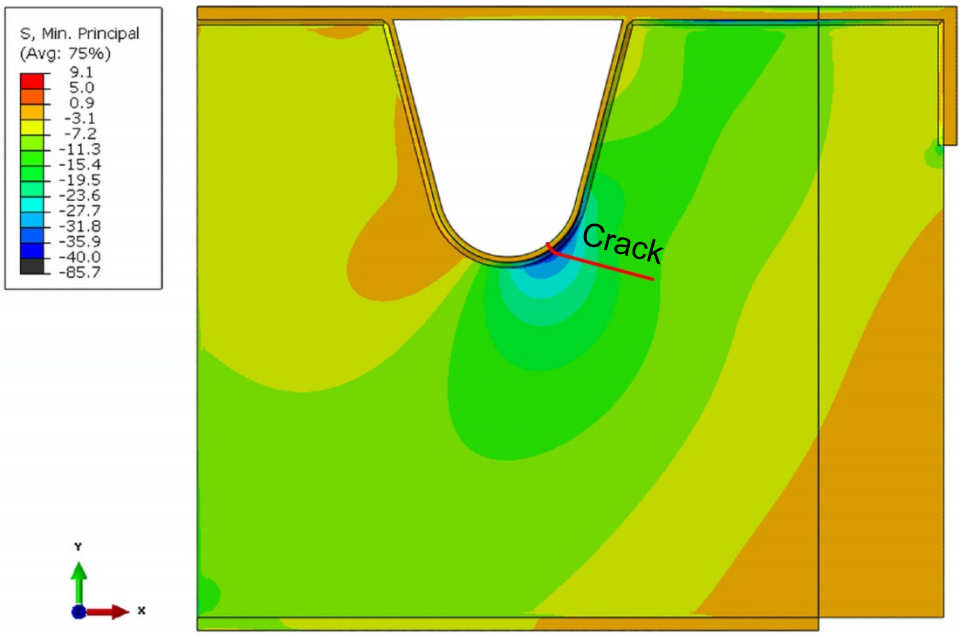

Figure 177. FEA contour of minimum principal stress in the floor beam web in MU2

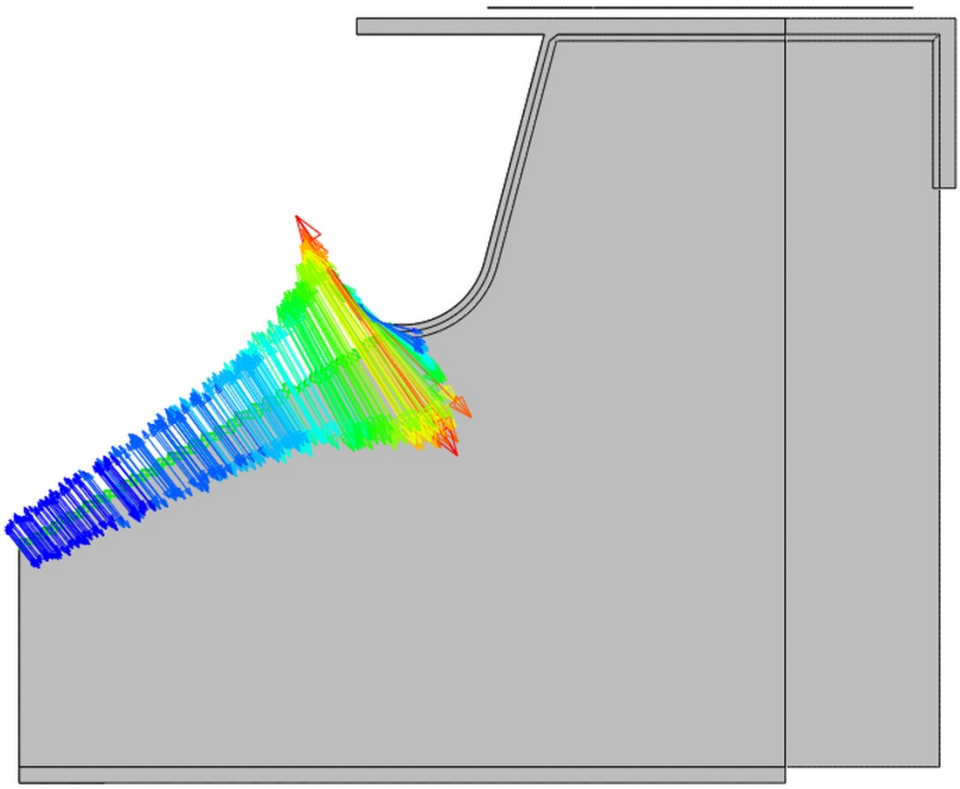

Figure 178. Direction of maximum principal stress in the floor beam web along the crack path to the north of rib in MU2 as obtained from FEA

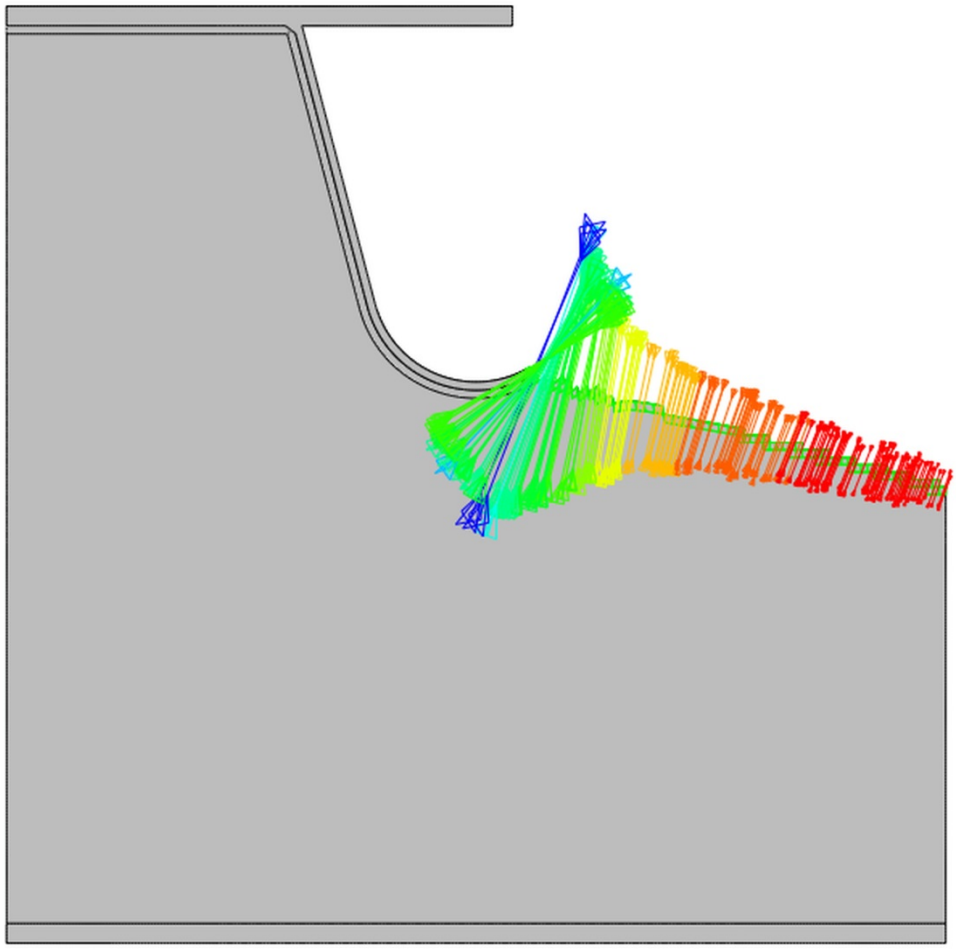

Figure 179. Direction of minimum principal stress in the floor beam web along the crack path to the south of rib in MU2 as obtained from FEA

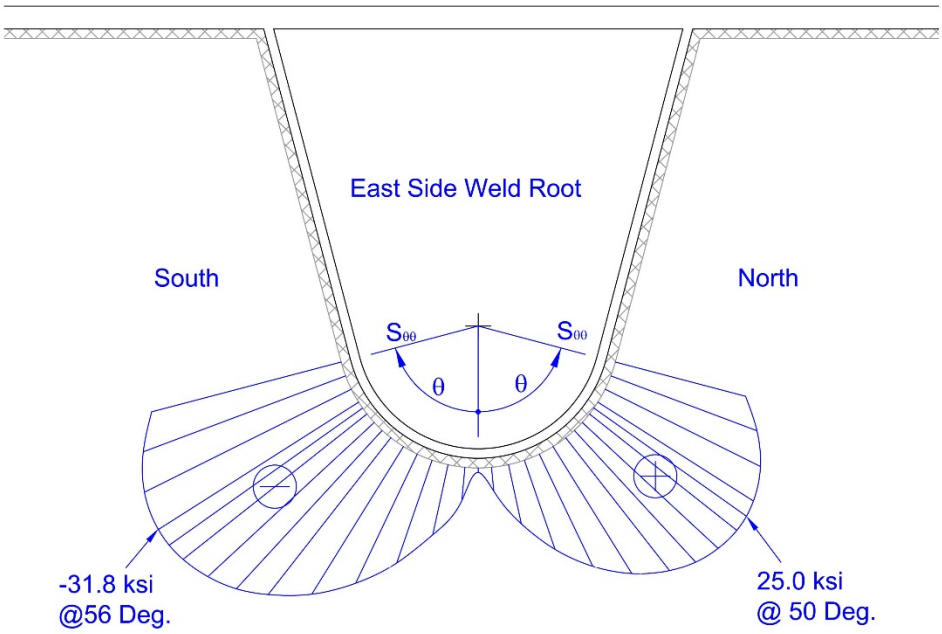

Figure 180. Distribution of circumferential stress (tangential to weld toe) at the rib-to-floor beam weld root along circumferential path through the weld root

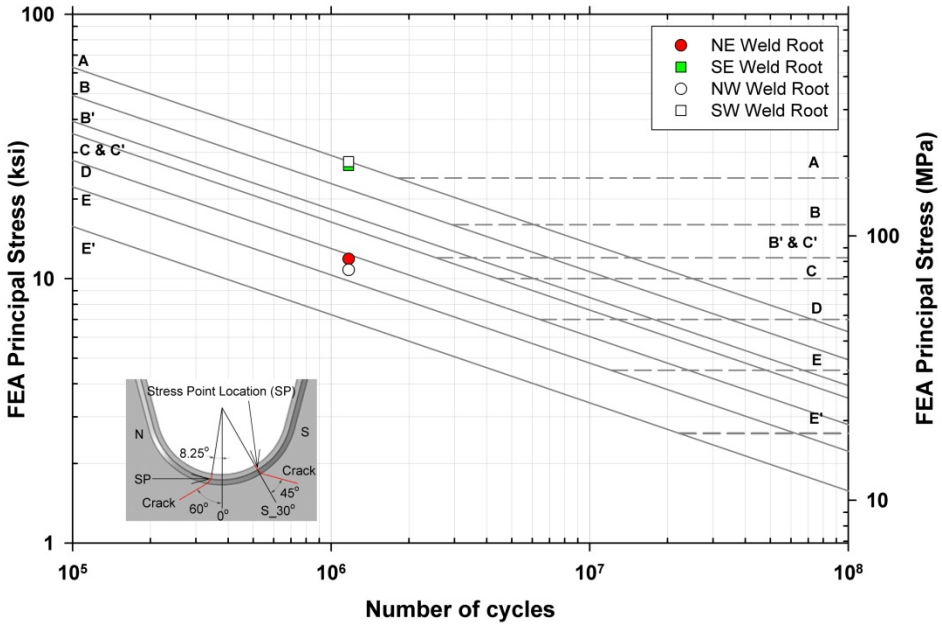

Figure 181. Fatigue test results for the rib-to-floor beam welds in MU2

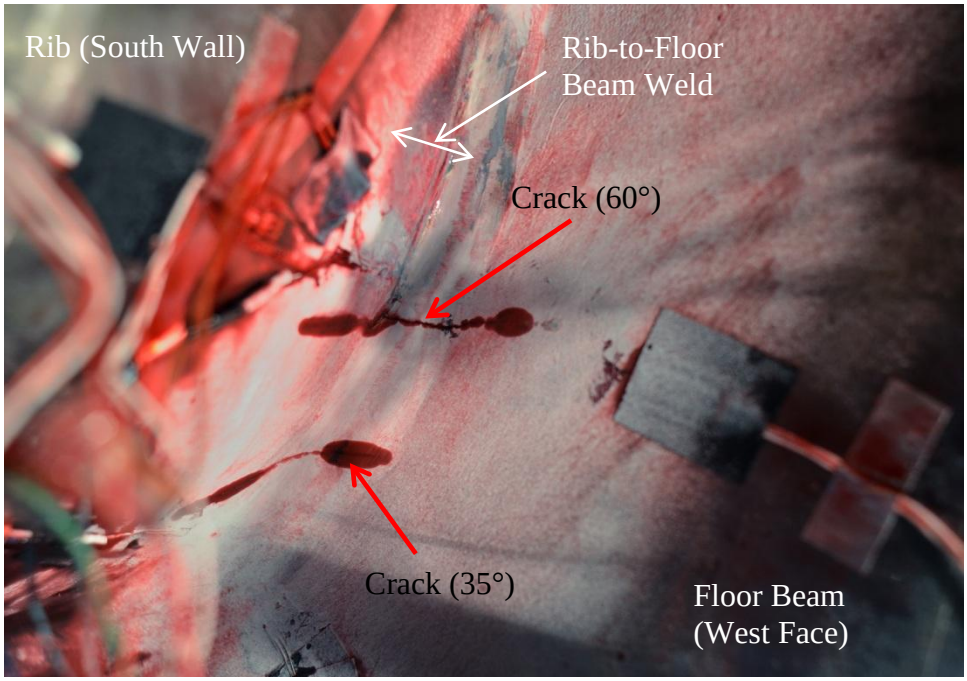

Figure 182. Crack at the floor beam-to-rib welded connection in the mock-up specimen MU3 – south west

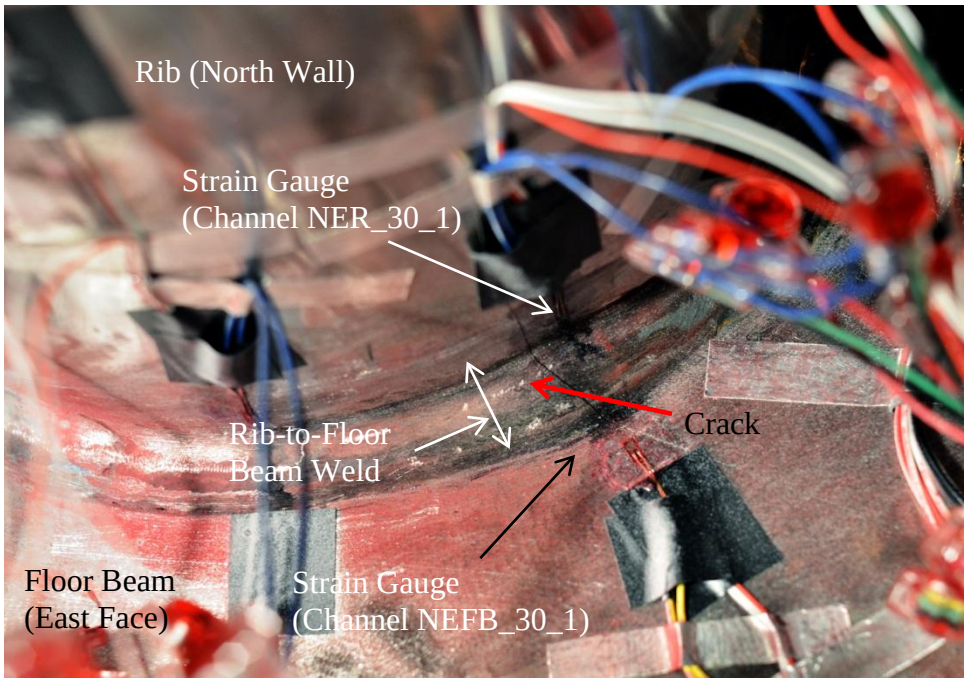

Figure 183. Crack at the floor beam-to-rib welded connection in the mock-up specimen MU3 – north east

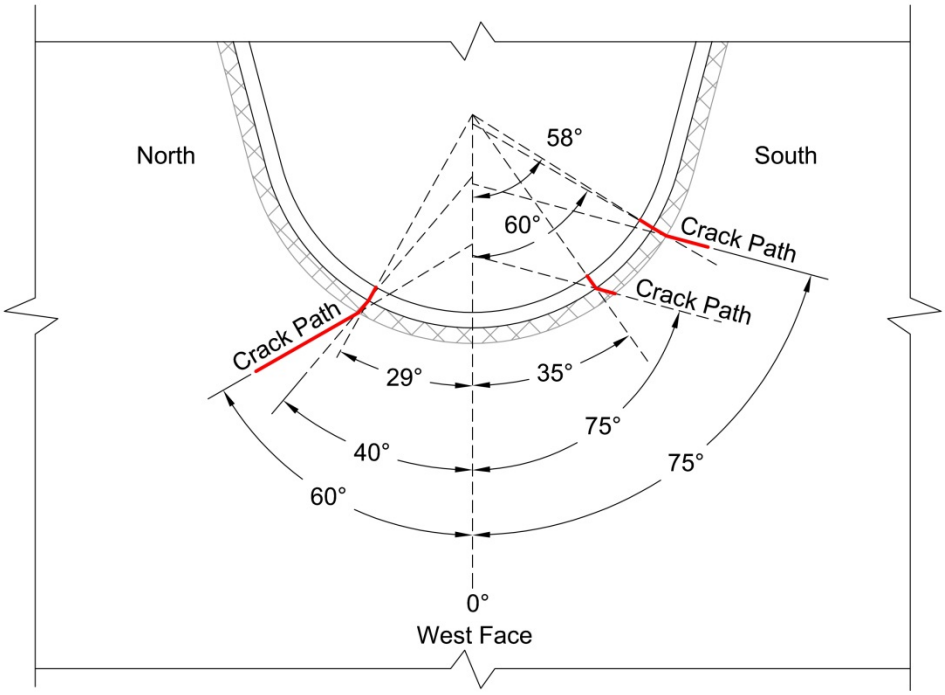

Figure 184. Schematics of cracks in mock-up specimen MU3

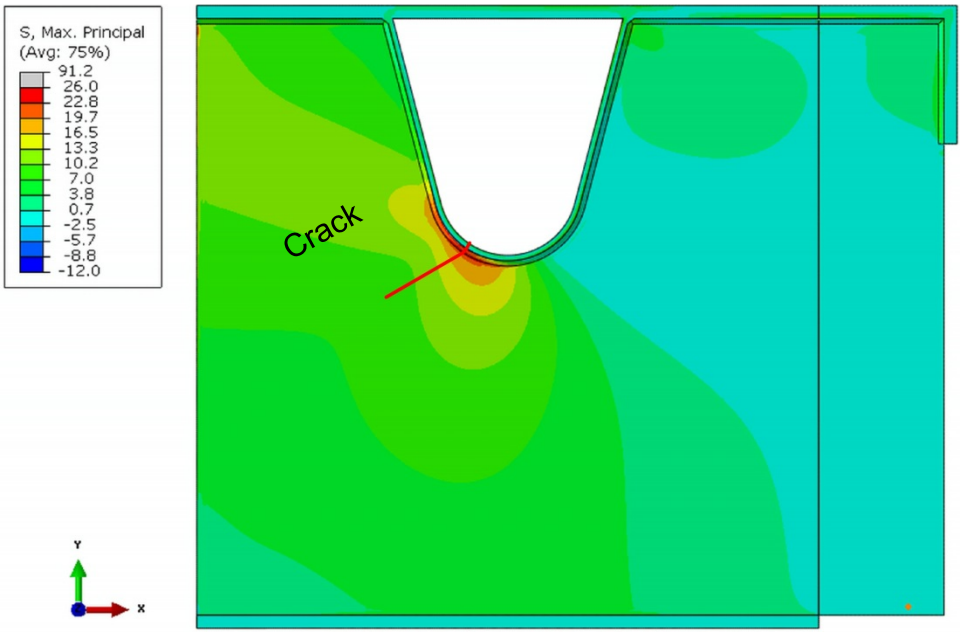

Figure 185. FEA contour of maximum principal stress in the floor beam web in MU3

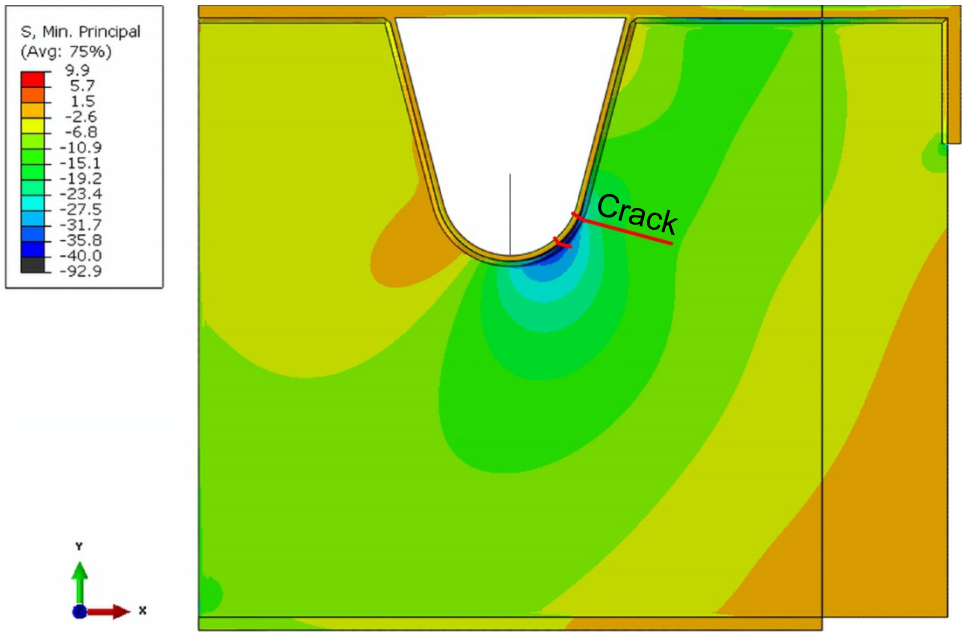

Figure 186. FEA contour of minimum principal stress in the floor beam web in MU3

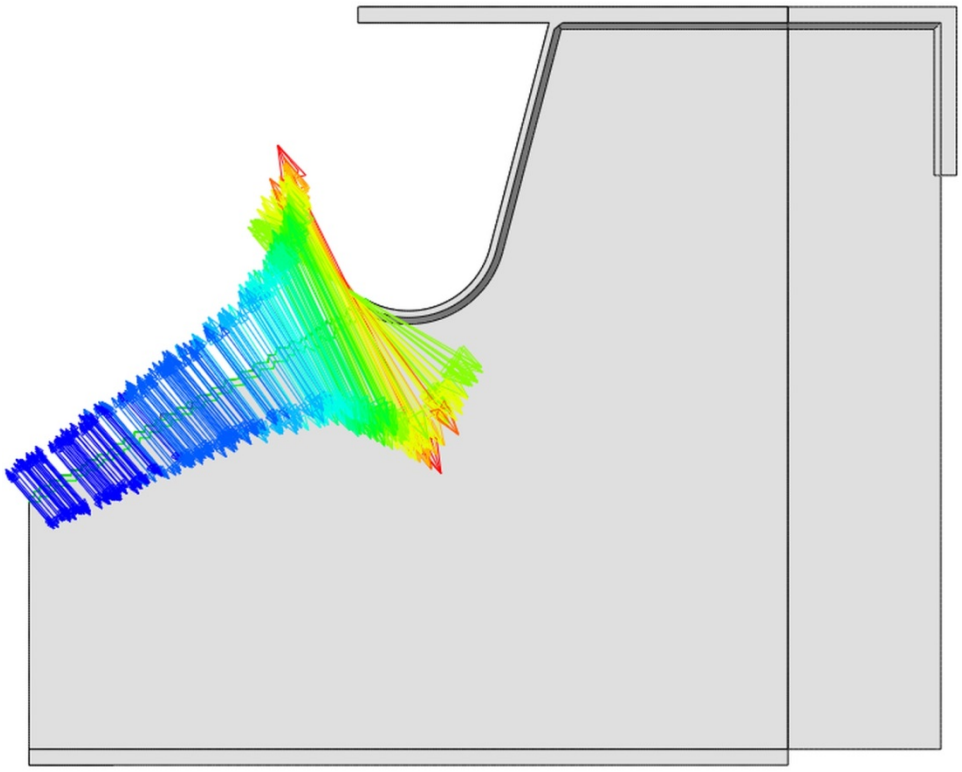

Figure 187. Direction of maximum principal stress in the floor beam web along the crack path to the north of rib in MU3 as obtained from FEA

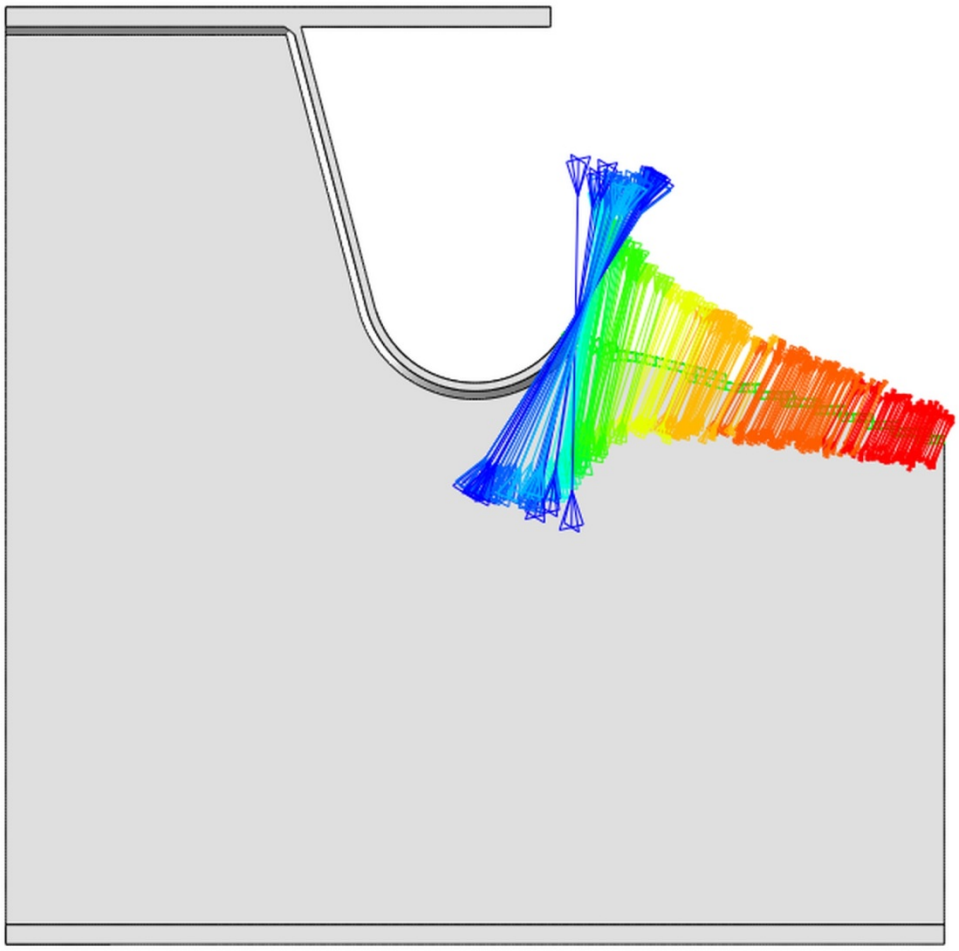

Figure 188. Direction of minimum principal stress in the floor beam web along the crack path (58° crack) to the north of rib in MU3 as obtained from FEA

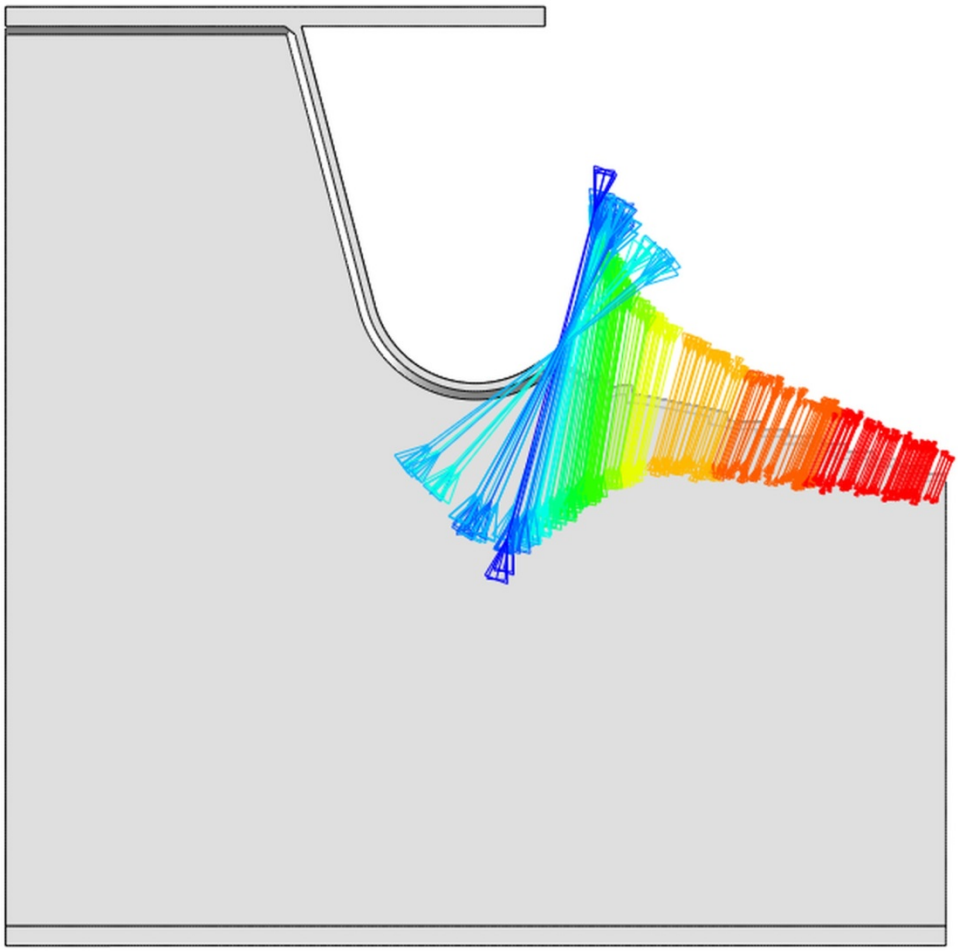

Figure 189. Direction of minimum principal stress in the floor beam web along the crack path (35° crack) to the north of rib in MU3 as obtained from FEA

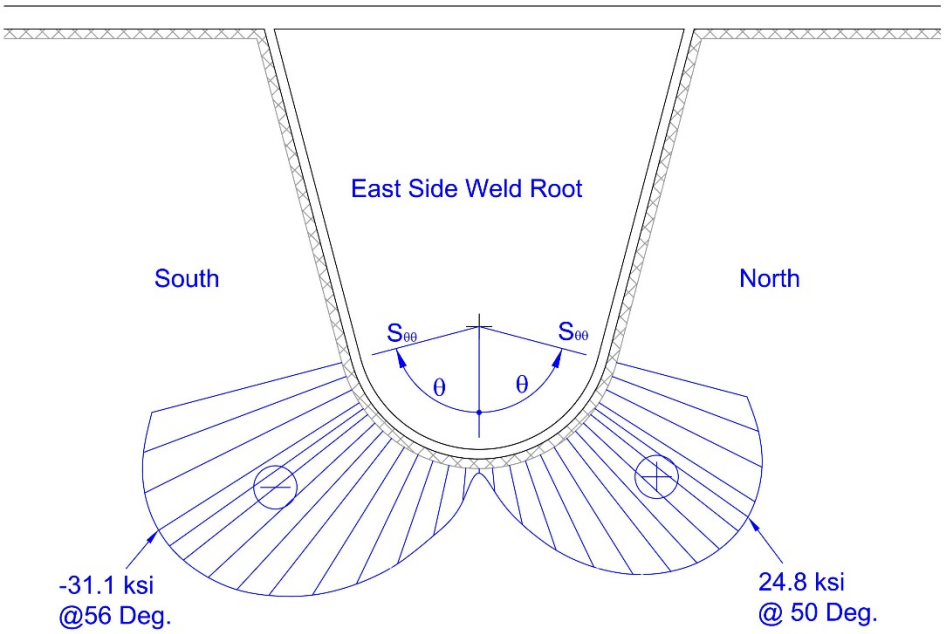

Figure 190. Distribution of circumferential stress (tangential to weld toe) at the rib-to-floor beam weld root along circumferential path through the weld root

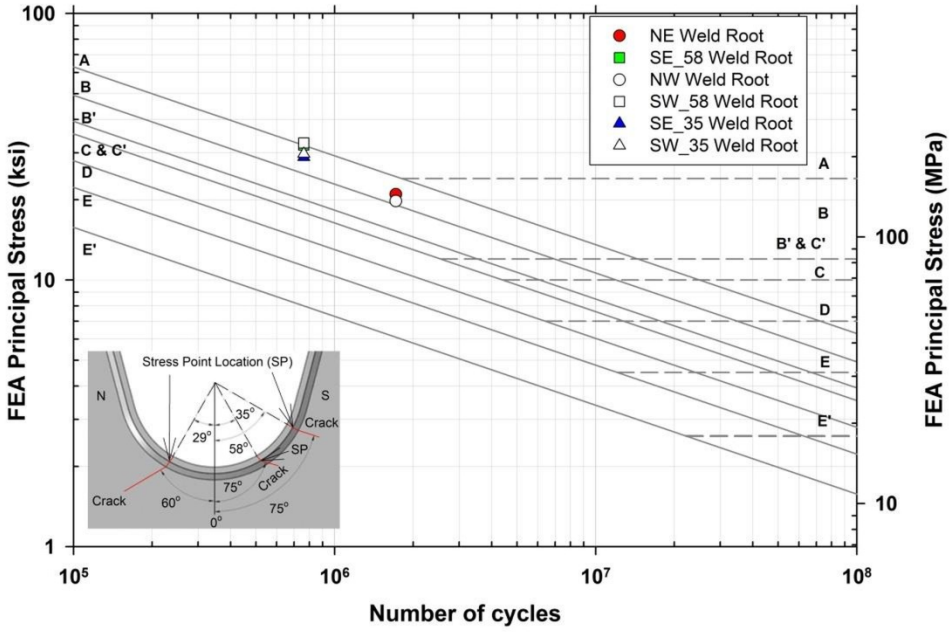

Figure 191. Fatigue test results for the rib-to-floor beam welds in MU3

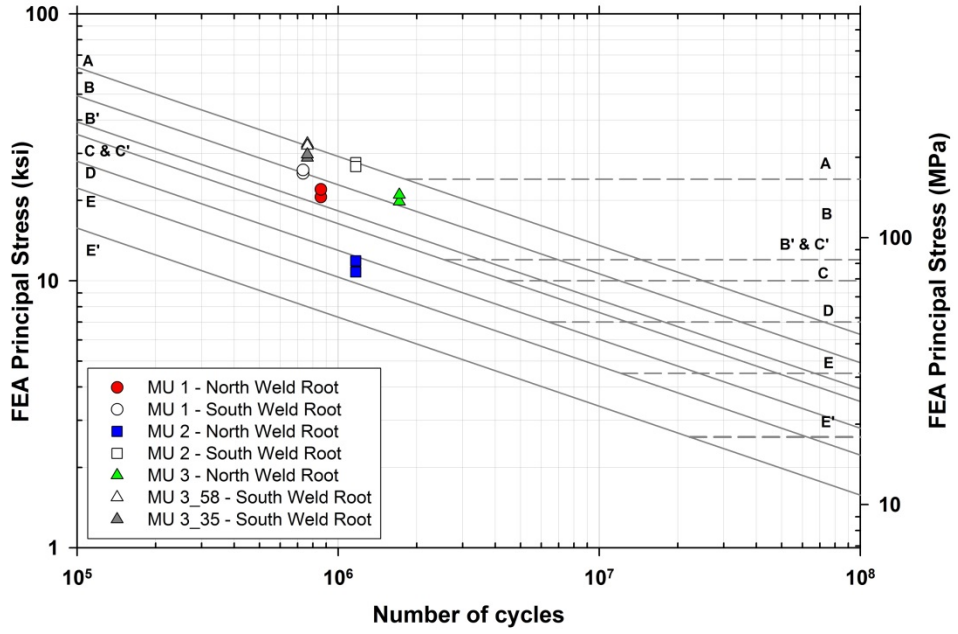

Figure 192. Fatigue test results for the rib-to-floor beam welds in MU1, MU2, and MU3

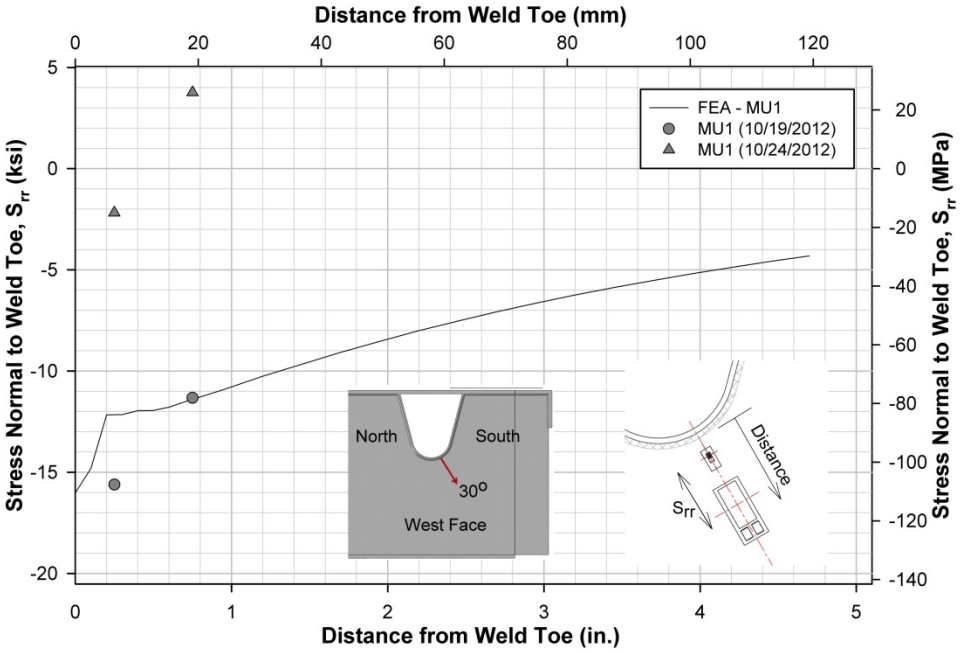

Figure 193. Change in stress at gauges on the west face of the floor beam along a path at 30 degrees from the rib soffit to the south of the rib in MU1

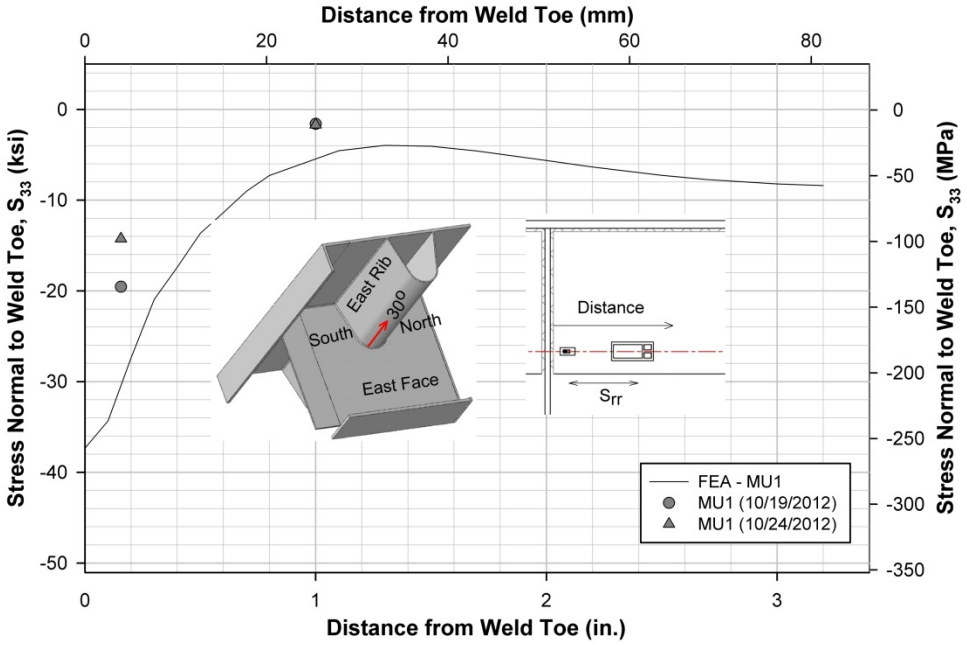

Figure 194. Change in stress at gauges on the outer face of the rib wall along a path at 30 degrees south from the rib soffit to the east of floor beam in MU1

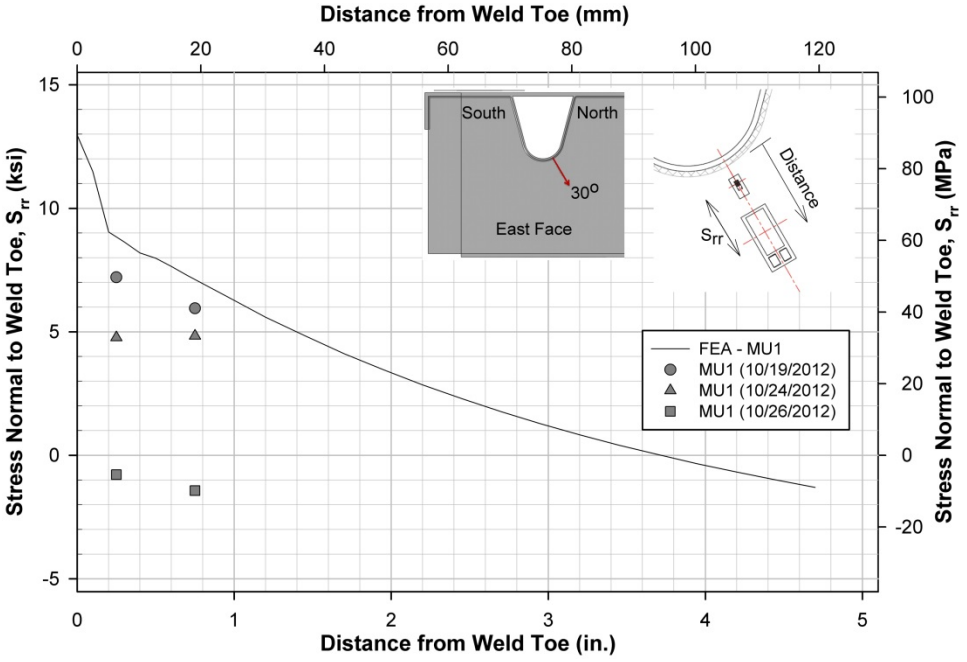

Figure 195. Change in stress at gauges on the east face of the floor beam along a path at 30 degrees from the rib soffit to the north of the rib in MU1

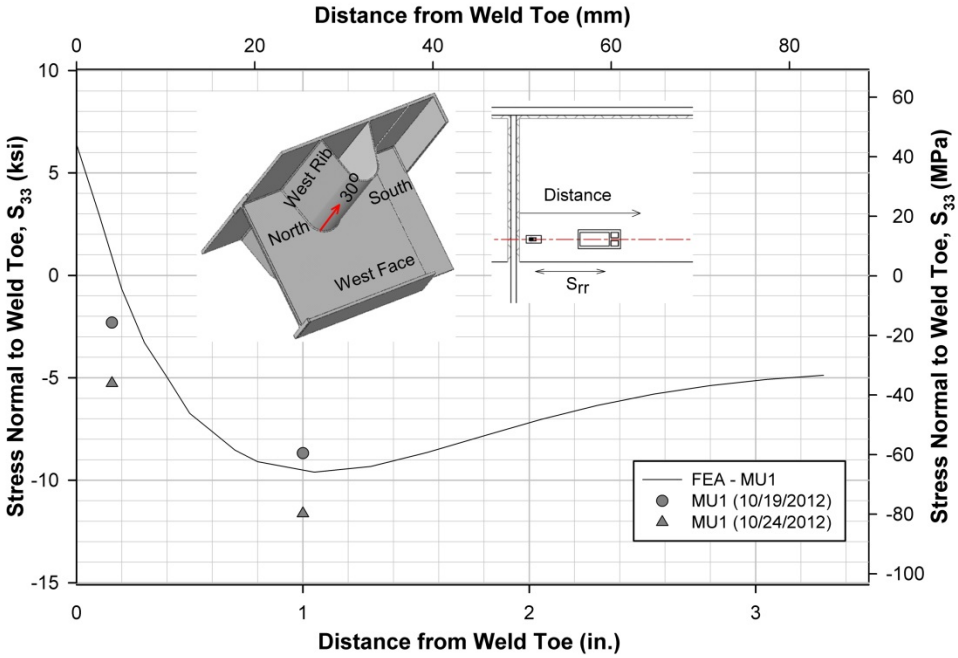

Figure 196. Change in stress at gauges on the outer face of the rib wall along a path at 30 degrees north from the rib soffit to the west of floor beam in MU1

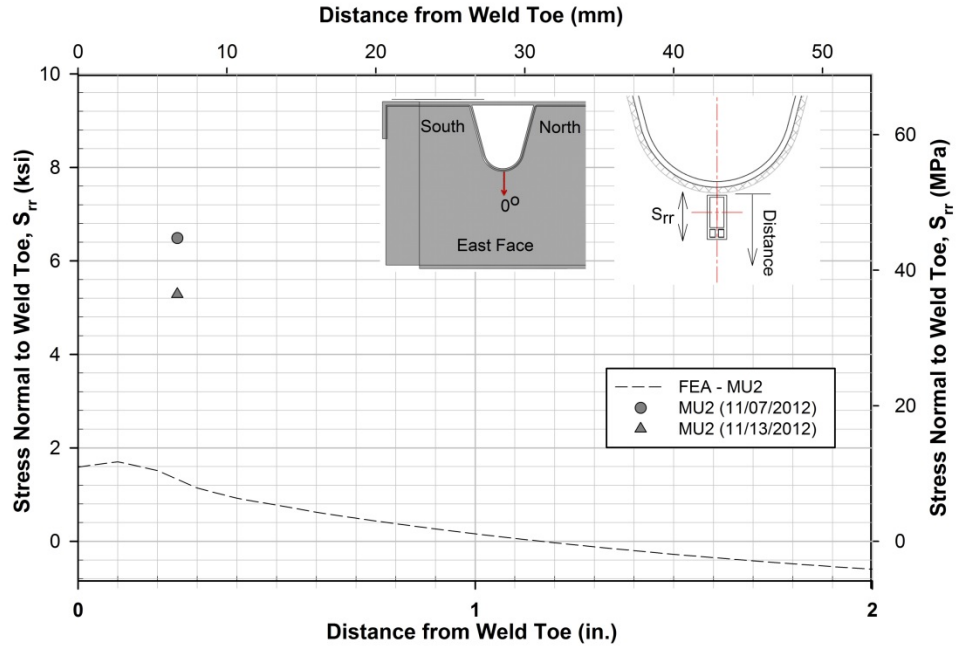

Figure 197. Change in stress at a gauge on the east face of the floor beam web along a path at 0 degrees from the rib soffit in MU2

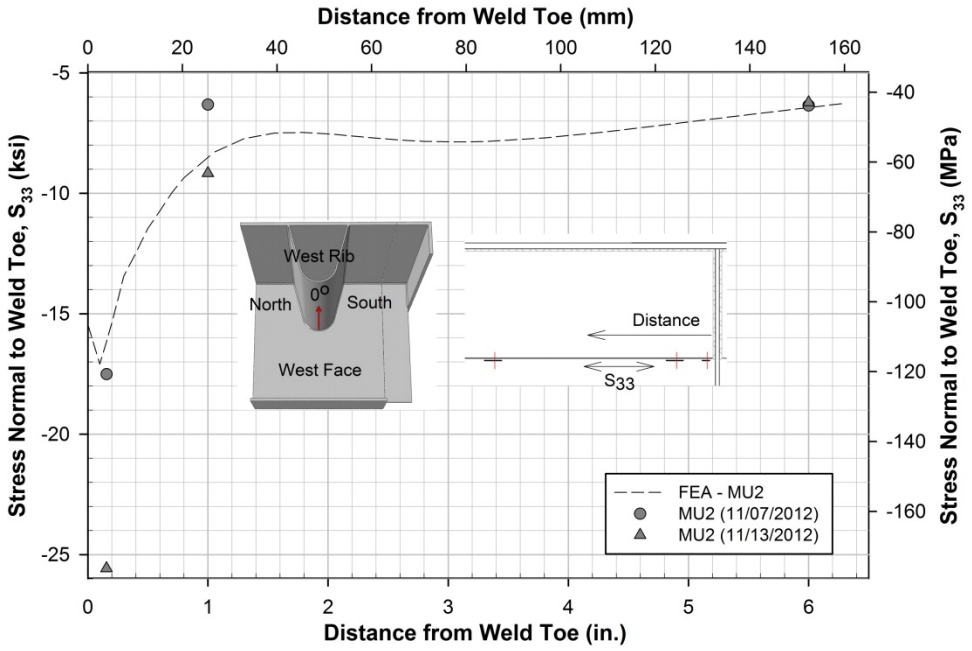

Figure 198. Change in stress at gauges on the rib soffit along a path to the west of floor beam in MU2

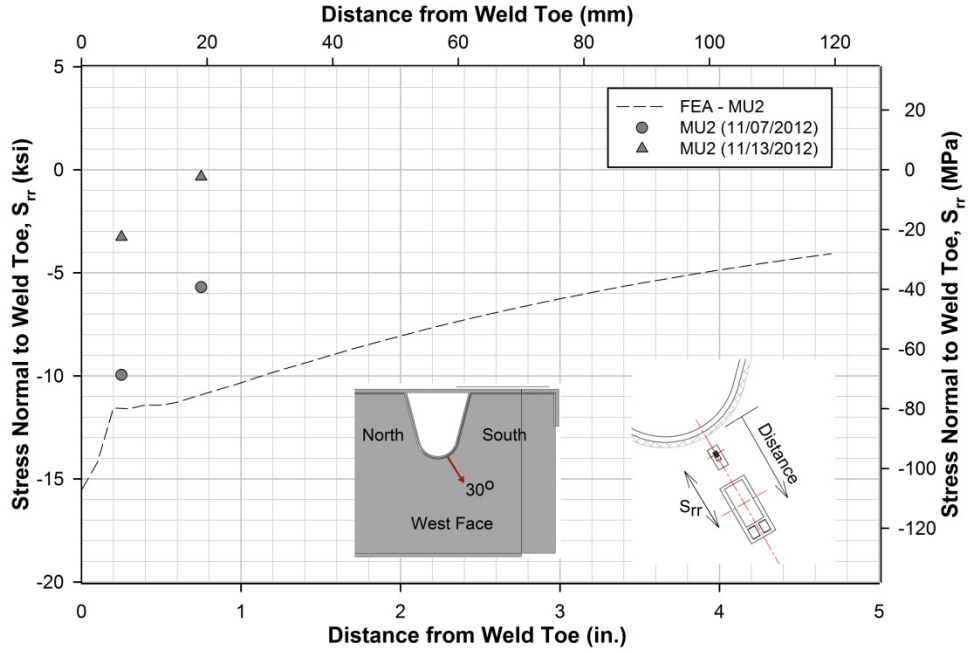

Figure 199. Change in stress at gauges on the west face of the floor beam along a path at 30 degrees from the rib soffit to the south of the rib in MU2

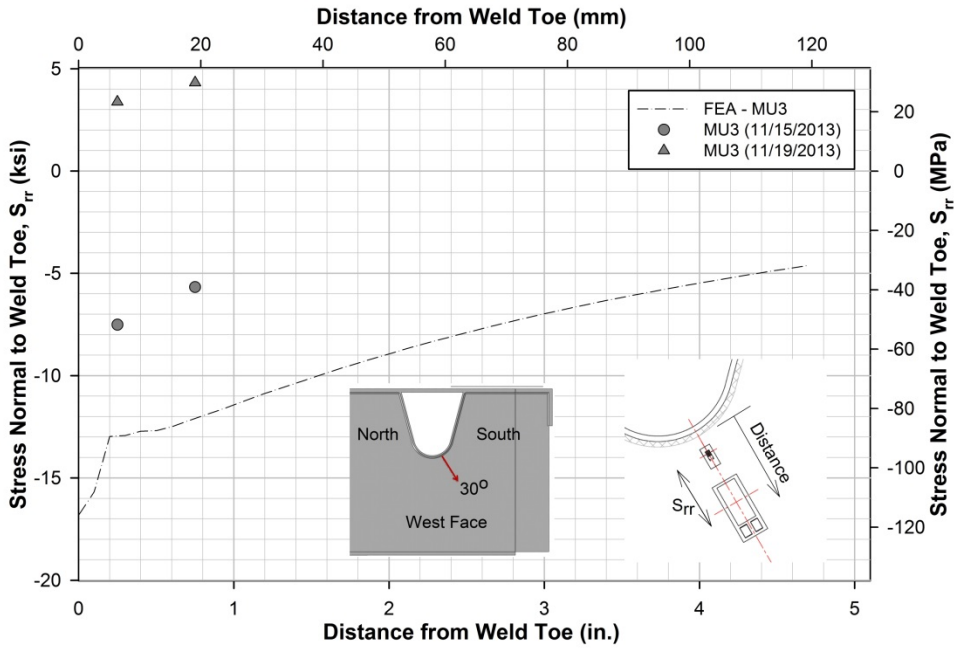

Figure 200. Change in stress at gauges on the west face of the floor beam along a path at 30 degrees from the rib soffit to the south of the rib in MU3

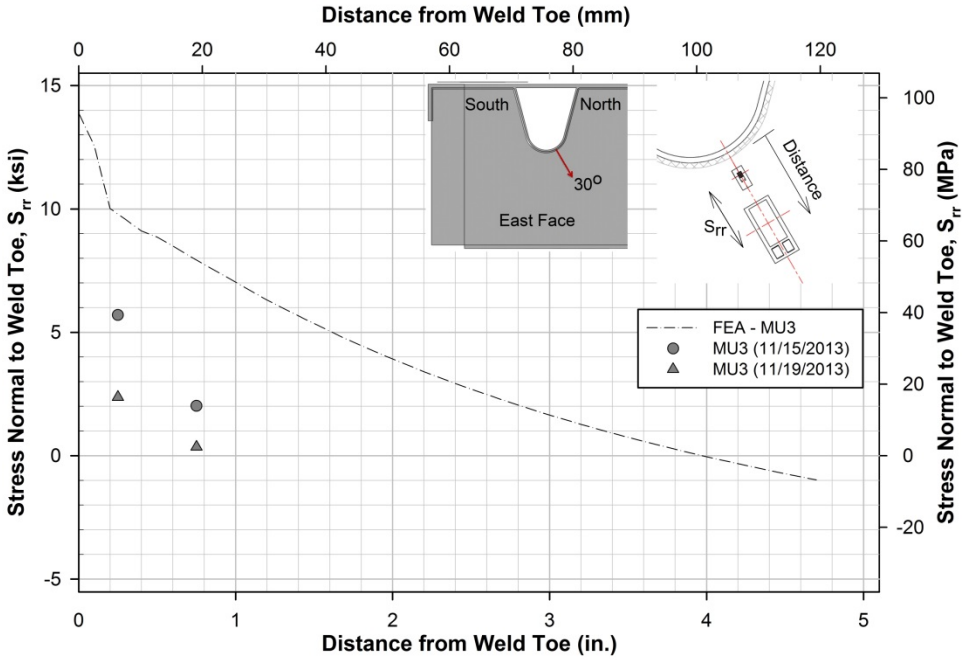

Figure 201. Change in stress at gauges on the east face of the floor beam along a path at 30 degrees from the rib soffit to the north of the rib in MU3

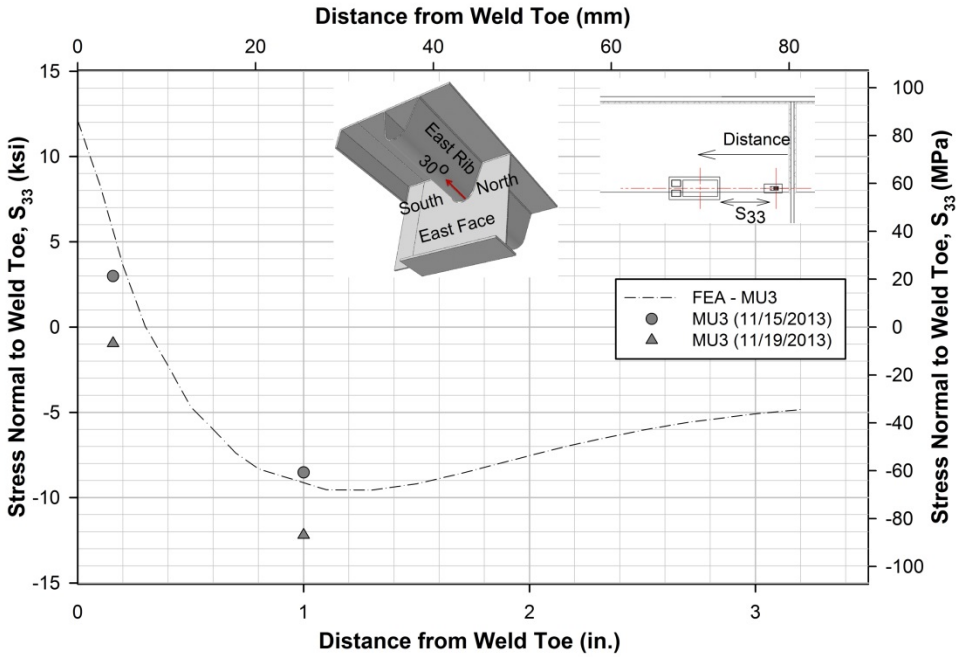

Figure 202. Change in stress at gauges on the outer face of the rib wall along a path at 30 degrees north from the rib soffit to the east of floor beam in MU3

5. POST-TEST DESTRUCTIVE EVALUATION OF MOCKUPS

The activities undertaken in Task 4 of the research project related to the post-test destructive evaluation of the weld details in the mockup specimens are reported in this chapter. After fatigue testing, the fatigue fracture surfaces were exposed for characterization of origin and growth of cracks. In addition, multiple polished and macro-etched cross sections of each welded detail of the rib-to-floor beam and rib-to-deck plate connections were prepared at discreet locations to destructively compare their fabrication conditions. The destructive measurements of the rib-to-deck plate connection details were also compared with the PAUT measurements.

5.1 Post-mortem Studies

5.1.1 Evaluation of Fatigue Cracking in MU1

Fatigue cracks at the rib-to-floor beam connection for MU1 has already been identified in section 4.2.1. A schematic of the fatigue cracks in MU1 is shown in Figure 203. After the fatigue test, the cracks at the rib-to-floor beam connections were exposed to characterize their origin and growth. Figures 204 and 205 show a typical portion of the floor beam and the rib containing the north and the south side cracks respectively, that was cut out of MU1. Figures 206 and 207 show the exposed mating fracture surfaces of the cracks to the north and the south sides of the rib respectively. The cracks grew on two different planes though the rib wall and the floor beam by transitioning through the rib-to-floor beam weld. As shown in Figure 203, the cracks grew in the rib wall and in the floor beams on planes subtending approximately 30 and 75 degrees to the vertical. Through the weld, the crack plane transitioned between the two, forming approximately 50 degrees with the vertical at around the weld root. It is also evident from Figures Figure 206 and Figure 207 that the cracks grew in two different planes through the rib wall and the floor beam. Figures Figure 208 and Figure 209 show an enlarged view of the fracture surfaces, photographed perpendicular to the camera to clarify the lack of fusion (LOF). Classical fatigue crack growth on multiple planes and in multi-stages was evident on the fracture surfaces. The cracks initiated at both edges of the LOF at the fillet weld root and grew in the first stage as circular (penny-shaped) cracks through the weld metal and the base metal. The two circular cracks coalesced on the floor beam web and grew as a larger single crack in the second stage at a much higher rate.

Measures of the LOF at the origin of the north and the south fatigue cracks are shown in Figures 208 and 209. The fit-up gap on the north side was larger, however, the fatigue crack developed on the south side earlier, suggesting that the fit-up gap probably did not have any significant effect on the fatigue crack initiation. It may be noted that fillet welds inherently include LOF, and such large LOF are not uncommon in properly fabricated fillet welded connections. Both fit-up gaps were within the specified tolerance of $^{1}/_{32}$ in. However, the width of LOF was larger on the south side which also developed fatigue cracking earlier than the north side, suggesting the possibility of width of LOF having significant effect on the fatigue crack initiation.

5.1.2 Evaluation of Fatigue Cracking in MU2

Fatigue cracks at the rib-to-floor beam connection for MU2 has already been identified in section 4.2.2. A schematic of the fatigue cracks in MU2 is shown in Figure 210. Similar to MU1, the cracks at the floor beam-to-rib connections were exposed to characterize their origin and growth. Figures 211 and 212 show a typical portion of the floor beam and the rib containing the north and the south side cracks respectively, that was cut out of MU2. Figures 213 and 214 show the exposed mating fracture surfaces of the cracks to the north and the south sides of the rib respectively. Similar to MU1, the cracks grew on two different planes though the rib wall and the floor beam by transitioning through the rib-to-floor beam weld. As shown in Figure 210, on the north and south sides, the cracks grew in the floor beam on planes subtending approximately 60 and 75 degrees respectively to the vertical. In the ribs on the north and the south sides, the crack planes subtended approximately 8 and 30 degrees respectively. Through the weld, the crack planes transitioned between the two, forming approximately 45 degrees with the vertical around the weld root. Figures 215 and 216 show the enlarged views of the fracture surfaces, photographed perpendicular to the camera to clarify the lack of fusion (LOF). As observed in MU1, classical fatigue crack growth in multi-stages was evident on the fracture surfaces, with the cracks initiating from both edges of the LOF at the fillet weld root. Similar to MU1, the cracks grew in the first stage as circular (penny-shaped) cracks through the weld metal and the base metal, and then circular cracks then coalesced on the floor beam web and the rib wall, and grew as a larger single crack in the second stage at a much higher rate. In addition, a crack growth from the fillet weld toe on the floor beam was observed on the south fracture surface that did not grow through the thickness when the fatigue testing was terminated.

Measures of the LOF at the origin of the north and the south fatigue cracks are shown in Figures 215 and 216. The fit-up gap on the north side was larger, whereas the width of LOF was about $^{1}/_{16}$ in. greater on the south side. Nevertheless, the fatigue cracks appeared at both locations at about the same number of cycles, suggesting that the fit-up gap probably did not have any significant effect on the fatigue crack development. Both fit-up gaps at the origin of fatigue cracks were less than the specified target of $^{1}/_{16}$ in.

5.1.3 Evaluation of Fatigue Cracking in MU3

Fatigue cracks at the rib-to-floor beam connection for MU3 has already been identified in section 4.2.3. A schematic of the fatigue cracks in MU3 is shown in Figure 217. After the fatigue test, the cracks at the floor beam-to-rib connections were exposed to characterize their origin and growth. Figures 218 and 219 show a typical portion of the floor beam and the rib containing the north and the south side cracks respectively, that was cut out of MU3. Adjacent to south side crack at 35 degrees, another similar crack at about 27 degrees from the rib soffit was discovered when a segment of the rib-to-floor beam connection containing the 35 degrees crack was cut out of MU3 for exposing the fracture surface. This second crack, however, did not progress into the floor beam, and therefore could not be easily exposed. The crack was exposed by brittle fracture after cooling the segment to cryogenic temperature in a liquid nitrogen bath. Figures 220 to

223 show the exposed mating fracture surfaces of the cracks. Similar to the other mockup specimens, the cracks grew on two different planes though the rib wall and the floor beam by transitioning through the rib-to-floor beam weld. This can be seen more clearly from Figure 224. On the north side, the crack grew in the floor beam on plane subtending approximately 60 degrees to the vertical as shown in Figure 217. In the rib wall, the crack grew on a plane subtending approximately 29 degrees to the vertical. On the south side, the crack planes at 35 and 60 degrees from the rib soffit subtended respectively 35 and 58 degrees through the rib wall. Through the weld, the crack planes transitioned between the angles in the rib and the floor beam, where the cracks grew on the floor beam subtending approximately 75 degrees to the vertical. The crack on the side at 27 degrees did not grow into the floor beam, but was estimated to form about 83 degrees through the weld. Figures 225 and 228 show the enlarged views of the fracture surfaces, photographed perpendicular to the camera to clarify the lack of fusion (LOF). Similar to the other specimens, classical fatigue crack growth in multi-stages was evident on the fracture surfaces. In the first stage, the fatigue cracks initiated from the LOF at the weld root and grew as circular (penny-shaped) cracks through the weld metal and the base metal of the rib. After breaking through the weld, the crack grew in the second stage through the floor bema web and the rib wall, still as a circular crack, but at a much higher rate. Thus, most of the fatigue life was expended in growing the fatigue crack in the first stage.

Measures of the LOF at the origin of the north and the south fatigue cracks are shown in Figures Figure 225 to Figure 228. The fit-up gaps were within the specified limit. The fit-up gap on the north side was larger, but the width of the LOF was much smaller. On the south side, the width of LOF was about $^{5}/_{16}$ in. with , but the fit up gap was generally much less than $^{1}/_{32}$ in. On one side, however, the LOF due to the fit-up gap increased to about $^{3}/_{32}$ in. It appears that this larger LOF on one side was created as the weld root at the bevel on the floor beam was not completely fused. As is evident, the fatigue crack grew centered about this LOF. The south fatigue cracks appeared much earlier than the north fatigue crack, suggesting that the fit-up gap probably did not have any significant effect on the fatigue crack growth, but the size of the LOF had. An adequately fabricated PJP weld would have had a smaller LOF as in the north crack location.

5.1.4 Conclusions from Post-mortem Studies

Fatigue testing of the mockup specimens identified a failure mode of the floor beam-to-rib welded connection by crack growth from the LOF at the weld root, when the fatigue cracking from the weld toe or through the weld throat was suppressed. This failure mode was not identified in the existing literature. No significant effect of the fit-up gap could be discerned from the limited data set; however, the size of the LOF seemed to have an effect on the fatigue resistance of the connection details, as adequately fabricated PJP rib-to-floor beam weld detail in MU3 with smaller LOF exhibited higher fatigue resistance than the corresponding fillet welded details in MU1 and MU2. No fatigue cracking was observed in any of the other welded connections.

5.2 Metallographic Studies

5.2.1 Rib-to-Deck Plate Weld Study

Destructive Evaluation

Multiple polished and macro-etched cross sections of each welded detail of rib-to-deck plate connection were prepared at discreet locations, and detailed measurements of the welds were made at each section to compare the fabricated conditions with the specified connection detail. Statistical estimates of the as-fabricated weld geometry were determined from these measurements and the fabrication conditions were comparatively assessed. The results of this study were discussed in detail in Interim Report 3 [(4)] (dated 02/25/2013). Noted below is a summary of the key findings of the study.

80% PJP weld was specified for both MU1 and MU2. However, the mean penetration was significantly lower than the specified for both the specimens. A minimum penetration of 75%, as specified by NJDOT's special provisions for orthotropic decks, was achieved only at a handful of sections. The largest variation of weld penetration was noted in MU2 with coefficient of variation (COV) as 19.8%. The weld penetration for MU3 was the most consistent among all the mockup specimens where a 70% PJP weld with a rib wall landing of $^{5}/_{32}$ in. and a bevel angle of 30° were specified. Mean weld penetrations of 73% and 71% were obtained at the south and the north sides of the rib respectively for MU3.

One of the primary reasons for the lesser weld penetration in MU1 and MU2 was probably inadequate heat input. Generally, higher heat input is required to facilitate desired weld penetration at connections without joint preparations as in MU1. However, chances of hot-cracking increases with higher heat input. Due to this apprehension, the heat input for welding MU1 was probably too low, which led to non-uniform and less than adequate penetration. In case of MU2, where a smaller root face or landing and a larger root opening or bevel was used to achieve the relatively larger 80% penetration, a melt-through or a blow through at the weld root was of concern due to the inherently high heat input associated with the SAW process. Driven by this apprehension, the heat input was probably again too low, resulting in the large variability in penetration and LOP over significant length of this mockup. For MU3, where a smaller penetration of 70% was specified with a larger landing, a more consistent minimum penetration was achieved due to a greater flexibility in selecting the welding parameters, with a lesser concern for a melt-through or a blow-through and inadequate penetration.

Extent of weld pentation didn't show any significant effect on the fatigue performance of this connection. Weld penetration under the load pads were as low as 55%. However, no fatigue cracking was observed. The minimum effective throat thickness of the welds at most details exceeded the nominal thickness of the rib, which allowed flow of stresses from the deck plate to the rib wall with minimum stress concentration at the weld root lack of penetration (LOP) and suppressed fatigue crack growth. Apparently, the minimum effective throat thickness of the welds is a more critical parameter for the

fatigue performance of the rib-to-deck plate welded connections than the weld penetration. The study didn't show any effect of fit-up gap.

An underfill of the weld metal was noted for all details, particularly towards the rib, where the weld surface was tangential to the rib wall. The weld nugget appeared to have lesser penetration towards the edges with the deck plate and the rib, creating a flared shape near the weld surface. In addition, all cross sections showed a relatively large heat affected zone (HAZ). These features are typical of a SAW process with relatively slower travel speed of the weld arc, particularly in the range of travel speeds employed for the rib-to-deck plate welds. In addition, a greater inclination of the wire towards the deck plate, rather than the rib wall, may have contributed to less than desired and inconsistent penetration of the PJP weld.

High Steel, the fabricator of the specimens, reported that a joint preparation or bevel on the rib wall added considerable effort in fabrication. Mechanization of joint preparation may be possible prior to the bending of the plates. Moreover, joint preparation introduced additional challenge of weld melt through or blow through conditions. However, the challenge of preventing hot cracking by reducing heat input for connection without bevel was of even higher concern. So, MU3 detail with bevel on the rib wall and a landing of $^{5}/_{32}$ in. (larger than MU2) was recommended by High Steel, as it allowed more flexibility in selecting the fabrication parameters for achieving the desired weld.

Comparison with PAUT

The weld penetrations of the rib-to-deck plate welds by destructive measurements are compared with the PAUT measurements in Tables 6 to 8 for MU1, MU2 and MU3 respectively. From the tables, it can be seen that the PAUT measurements didn't match with the destructive measurements at all the sections. For MU1 the maximum PAUT measurement was 42% (95%) higher than the destructive measured weld penetration (53%). For MU2 the PAUT weld penetration exceeded the destructively measured weld penetration by41 % and for MU3 this value was 35%. Due to this large differences, the procedure of PAUT scanning by GE Phasor XS was questionable. Subsequently, in the later mockups, the weld penetrations were non-destructively measured using Olympus OmniScan MX1 equipment, which is discussed in detail in Chapter 7.

Recommendations for the Full-size Specimen

Based on the Phase 2 study on the mockup specimens, a 70% PJP weld with a $^{5}/_{32}$ in. (4 mm) root face or landing on the rib wall was recommended for the rib-to-deck plate connections of the orthotropic deck. A penetration range of 65% to 100% without any blow-through may be accepted. Limited study conducted so far has not shown any significant effect of melt-trough and therefore melt-through condition at the weld root should be acceptable. A weld penetration providing a minimum effective throat thickness equal to the rib wall may be accepted as an absolute minimum in special circumstances, without any adverse effect on the deck performance. It was recommended that the limitation on the root gap or the fit-up tolerance between the rib

and the deck plate be relaxed and left to the discretion of the fabricator. Any root gap that would allow consistent fabrication of the weld should be acceptable.

The travel speed of the weld arc may be increased to obtain a deeper and narrower penetration and a more proportionate weld zone. It is also possible to obtain a deeper and narrower penetration by adjusting other parameters. More inclination of the wire towards the weld root should also help in achieving a deeper penetration and a steeper weld profile. In addition, increasing the bevel angle to 35 degrees and a minor adjustment in heat input may be necessary to accomplish a consistent penetration at the weld root. The fabricator must design a weld procedure that will properly target the joint root, achieve the desired penetration without blow-through or significant melt-through, and would generate a deeper and narrower weld profile without any underfill (or washout). This approved weld procedure must be executed with due quality control to consistently produce the desired rib-to-deck plate weld.

The scope of Phase 2 study was to evaluate several fabrication conditions and select a cost-effective detail for the large orthotropic deck specimen. To this end only a few mockups were available within the limited budget and time. Achieving a specified weld penetration uniformly and consistently for a particular joint preparation requires careful selection of the right welding parameters through repeated trials, and several destructive evaluations of the fabricated connection to verify the as-welded condition. Usually, these efforts are carried out more rigorously during the production welding of orthotropic decks. The welding procedures developed during the Phase 2 study and the lessons learnt provided the foundation for refining the parameters for uniform and consistent fabrication of the rib-to-deck plate connection.

Additional full-scale mockups were subsequently fabricated and evaluated (see chapter 7, contained in Volume III) in the research project, where the welding parameters were varied and different weld details were investigated to achieve the desired penetration and weld bead shape.

5.2.2 Rib-to-Floor Beam Weld Study

Destructive Evaluation

Similar to the rib-to-deck plate connection, multiple polished and macro-etched cross sections of each welded detail of rib-to-floor beam connection were also prepared at discreet locations, and detailed measurements of the welds were made at each section to compare the fabricated conditions with the specified connection detail. Statistical estimates of the as-fabricated weld geometry were determined from these measurements and the fabrication conditions were comparatively assessed.

In this report, the rib-to-floor beam sections are identified by the mock specimen identification (e.g., MU1, MU2 or MU3) suffixed by the side of the connection (e.g., N for North or S for South) and then suffixed by the location of the section measured in degree from the rib soffit at the centerline (e.g., 0, 30, 60, etc.). For the section identification of the fatigue crack surfaces, “F” is prefixed before the location of the

section, to identify it as the fracture surface. Total 21 cross sections were prepared with 6 sections for each of MU1 and MU2, and 9 for MU3.

The rib-to-floor beam weld sections were etched at with 5% Nital. The macro-etched sections were then digitally photographed. The dimensional parameters of the rib-to-floor beam weld were measured from the digital photographs of the macro-etched sections as described in the following. The photographs were imported into AutoCAD 2014 (Autodesk, Inc.). The nominal floor beam thickness was considered as the basis for the measurement. A scaling factor was computed as the ratio of the nominal floor beam thickness to the floor beam thickness measured from the digital photographs in AutoCAD. The other measured dimensional parameters were multiplied with this scaling factor to obtain the respective sizes. The dimensional parameters are shown in Figure 229. The measured dimensional parameters were: (a) the lack of fusion of the weld, *LOF* and (b) the root opening or fit-up gap between the rib and the floor beam, *R*.

The macro-etched sections of the rib-to-floor beam welds in the mockup specimens are shown in Figures B-1 to B-13. The destructive weld measurements on the macro-etched sections are tabulated in Tables 9 to 11 for MU1, MU2 and MU3 respectively. For MU1, the value of R ranged between 0.020 in. and 0.045 in. (~$^{3}/_{64}$ in.), with a mean of 0.03 in. (~$^{1}/_{32}$ in.) and a large COV of 29.7%. Such large COV can be expected considering the small magnitude of R. Out of 6 sections in MU1, the R value in 3 sections were less than the specified $^{1}/_{32}$ in. The LOF showed a less variance (COV of 20.5%), with a mean of 0.391 in., or mean fusion of about 22%. Such small fusion or large LOF is typical of fillet welded connections. For MU2, the value of R ranged between 0.017 in. and 0.048 in. (~$^{3}/_{64}$ in.), with a mean of 0.027 in. (~$^{1}/_{32}$ in.) and a large COV of 41.2%. Such large COV can be expected considering the small magnitude of R. All the 6 sections have R value less than the target $^{1}/_{16}$ in. The LOF showed a lot less variance (COV of 12.9%), with a mean of 0.409 in., or mean fusion of about 18%. Such small fusion or large LOF is typical of fillet welded connections. MU3 was fabricated with a higher root gap. The value of R ranged between 0.031 in. and 0.109 in. (~$^{1}/_{8}$ in.), with a mean of 0.068 in. (~$^{1}/_{16}$ in.) and a large COV of 41.9%. Such large COV can be expected considering the small magnitude of R. Out of 9 sections in MU2, the R value in 2 sections were more than the target $^{3}/_{32}$ in. The LOF also showed a large variance (COV of 37.6%), with a mean of 0.239 in., or mean fusion of about 52%. Such large fusion or small LOF is typical of PJP welded connections. The distributions of LOF and R in the three mockup specimens are shown in Figure 230 and Figure 231 respectively.

Typical macro-etched cross sections of the rib-to-floor beam weld in MU1, MU2 and MU3 are shown in Figures 232 to 234. The photo macrographs of the all sections are provided in Appendix B. The weld profiles for MU1 and MU2 were typical of manual fillet welds with large LOF. The welds were fused to the rib and the floor beam and the quality of the fillet welds appeared to be adequate. The weld profile for MU3 was typical for a PJP welded detail with smaller LOF and larger R. Unacceptable weld profiles were noted at two cross sections in MU3 (Figures 235 and 236). The weld fusion on one side of these sections appeared to be more like a fillet welded connection as in MU1 and MU2. On the other side, the weld root at the bevel on the floor beam was not completely fused. Apparently, the joint preparation (bevel) on the floor beam was non uniform in

contrary to the design, which created a larger LOF than expected at the typical PJP weld root.

Recommendations for the Full-size Specimen

Fatigue testing of the mock-up specimens identified a failure mode of the rib-to-floor beam welded connection by crack growth from the LOF at the weld root. This failure mode was not identified in the existing literature. No significant effect of the fit-up gap could be discerned from the limited data set; however, the size of the LOF seemed to have an effect on the fatigue resistance of the connection details, as smaller LOF exhibited higher fatigue resistance.

High Steel, the fabricator of the mock-up specimens, reported that the efforts required for fitting the floor beam-to-rib connection of MU1 was about eight times the effort required for fitting the connection in MU3, even considering the joint preparation required for the PJP welded detail. The primary reason for the increased effort was the significant grinding of the floor beam required to achieve a fit-up gap tolerance of $^{1}/_{32}$ in., due to the uncontrolled surface profile of the fabricated ribs. The efforts required to accomplish a target fit-up tolerance of $^{1}/_{16}$ in. with a maximum limit of $^{3}/_{32}$ in. for the floor beam-to-rib connection in MU2 were about four times that of MU3. As the test results demonstrated, the fit-up gap did not have any significant effect on the fatigue resistance of the subject connection, whereas the larger LOF at the weld root precipitated fatigue cracking, when the other modes of fatigue crack growth were suppressed. As such, the rib-to-floor beam connection detail in MU3 appeared to be the most cost-effective for the proposed orthotropic deck design of the Wittpenn Bridge. It was recommended that the performance of this detail in the full-size large scale prototype, resembling the production fabrication, be investigated in Phase 3 of this research project.

Table 6 - Comparison of Destructive and PAUT Measurements of Rib-to-Deck Plate Welds in MU1

ID	Phased Array		Destructive		Difference	
	LOP (in.)	Pen. (%)	LOP (in.)	Pen. (%)	LOP (in.)	Pen. (%)
MU1_SE_A	0.015	95	0.098	70	0.083	26
MU1_SE_B	0.017	95	0.153	53	0.136	42
MU1_SE_C	0.018	94	0.148	54	0.130	40
MU1_SE_D	0.029	91	0.141	56	0.112	35
MU1_SE_E	0.013	96	0.112	65	0.100	31
MU1_SE_F	0.033	90	0.139	57	0.107	33
MU1_SW_G	0.017	95	0.111	66	0.094	29
MU1_SW_H	0.013	96	0.115	64	0.102	31
MU1_SW_I	0.021	94	0.110	66	0.090	28
MU1_SW_J	0.038	88	0.100	69	0.062	19
MU1_SW_K	0.024	93	0.094	71	0.071	22
MU1_SW_L	0.014	96	0.112	65	0.098	30
MU1_NW_M	0.013	96	0.075	77	0.062	19
MU1_NW_N	0.012	96	0.099	69	0.087	27
MU1_NW_O	0.019	94	0.073	78	0.054	17
MU1_NW_P	0.021	93	0.104	68	0.082	25
MU1_NW_Q	0.022	93	0.100	69	0.078	24
MU1_NW_R	0.019	94	0.095	71	0.075	23
MU1_NE_S	0.021	93	0.087	73	0.065	20
MU1_NE_T	0.014	96	0.087	73	0.073	23
MU1_NE_U	0.045	86	0.078	76	0.034	10
MU1_NE_V	0.028	91	0.101	69	0.074	23
MU1_NE_W	0.019	94	0.103	68	0.085	26
MU1_NE_X	0.024	93	0.096	70	0.072	22
Maximum	0.045	96	0.153	78	0.136	42
Minimum	0.012	86	0.073	53	0.034	10
Mean	0.021	93	0.105	67	0.084	26
Std. Dev.	0.008	2.545	0.022	6.719	0.023	7.227
COV (%)	38.8	2.7	20.4	9.9	27.6	27.7

Table 7 - Comparison of Destructive and PAUT Measurements of Rib-to-Deck Plate Welds in MU2

Section	Phased Array		Destructive		Difference	
	LOP (in.)	Pen. (%)	LOP (in.)	Pen. (%)	LOP (in.)	Pen. (%)
MU2_SE_A	0.042	87	0.142	56	0.100	31
MU2_SE_B	0.013	96	0.138	57	0.125	39
MU2_SE_C	0.032	90	0.116	64	0.084	26
MU2_SE_D	0.032	90	0.118	63	0.086	27
MU2_SE_E	0.025	92	0.105	67	0.080	25
MU2_SE_F	0.038	88	0.047	85	0.008	3
MU2_SW_G	0.038	88	0.104	68	0.066	21
MU2_SW_H	0.023	93	0.076	76	0.053	16
MU2_SW_I	0.020	94	0.020	94	-0.001	0
MU2_SW_J	0.024	93	0.092	71	0.068	21
MU2_SW_K	0.047	85	0.000	100	-0.047	-15
MU2_SW_L	0.037	88	0.139	56	0.102	32
MU2_NW_M	0.030	91	0.115	64	0.085	26
MU2_NW_N	0.048	85	0.073	77	0.025	8
MU2_NW_O	0.047	86	0.152	53	0.105	33
MU2_NW_P	0.024	93	0.119	63	0.095	29
MU2_NW_Q	0.047	85	0.154	52	0.107	33
MU2_NW_R	0.031	90	0.162	50	0.131	41
MU2_NE_S	0.045	86	0.119	63	0.074	23
MU2_NE_T	0.054	83	0.124	62	0.069	21
MU2_NE_U	0.012	96	0.145	55	0.132	41
MU2_NE_V	0.049	85	0.169	48	0.120	37
MU2_NE_W	0.034	89	0.154	52	0.120	37
MU2_NE_X	0.029	91	0.152	53	0.123	38
Maximum	0.054	96	0.169	100	0.132	41
Minimum	0.012	83	0.000	48	-0.047	-15
Mean	0.034	89	0.114	65	0.080	25
Std. Dev.	0.012	3.610	0.044	13.701	0.045	14.036
COV (%)	34.0	4.0	38.6	21.2	56.6	56.6

Table 8 - Comparison of Destructive and PAUT Measurements of Rib-to-Deck Plate Welds in MU3

Section	Phased Array		Destructive		Difference	
	LOP (in.)	Pen. (%)	LOP (in.)	Pen. (%)	LOP (in.)	Pen. (%)
MU3_SE_A	0.024	93	0.085	74	0.061	19
MU3_SE_A1	0.071	78	0.085	74	0.014	4
MU3_SE_B	0.024	93	0.114	65	0.090	28
MU3_SE_C	0.019	94	0.092	71	0.073	23
MU3_SE_D	0.024	93	0.094	71	0.070	22
MU3_SE_E	0.036	89	0.057	82	0.020	6
MU3_SE_F	0.042	87	0.075	77	0.034	10
MU3_SE_F1	0.072	78	0.075	77	0.004	1
MU3_SW_G	0.049	85	0.031	90	-0.018	-6
MU3_SW_H	0.034	89	0.087	73	0.053	17
MU3_SW_I	0.017	95	0.087	73	0.070	22
MU3_SW_J	0.027	92	0.086	73	0.059	18
MU3_SW_K	0.009	97	0.118	63	0.109	34
MU3_SW_L	0.016	95	0.101	69	0.085	26
MU3_NW_M	0.015	95	0.117	64	0.103	32
MU3_NW_N	0.032	90	0.105	67	0.074	23
MU3_NW_O	0.026	92	0.139	57	0.114	35
MU3_NW_P	0.028	91	0.111	66	0.083	26
MU3_NW_Q	0.021	94	0.115	64	0.095	29
MU3_NW_R	0.026	92	0.069	79	0.043	13
MU3_NE_S	0.028	91	0.071	78	0.044	13
MU3_NE_T	0.061	81	0.019	94	-0.042	-13
MU3_NE_U	0.017	95	0.097	70	0.080	25
MU3_NE_V	0.024	93	0.089	72	0.066	20
MU3_NE_W	0.045	86	0.110	66	0.065	20
MU3_NE_X	0.018	94	0.101	69	0.082	25
MU3_NE_X2	0.019	94	0.101	69	0.081	25
Maximum	0.072	97	0.139	94	0.114	35
Minimum	0.009	78	0.019	57	-0.042	-13
Mean	0.030	91	0.090	72	0.060	18
Std. Dev.	0.016	5.075	0.026	8.077	0.038	11.675
COV (%)	53.7	5.6	28.9	11.2	63.1	63.1

Table 9 - Measured Dimensional Parameters of Rib-to-Floor Beam Weld for MU1

Sl. No.	Sample ID	LOF (in.)	R (in.)
1	MU1_N_F	0.426	0.045
2	MU1_N_F	0.500	0.023
3	MU1_N_60	0.327	0.032
4	MU1_N_70	0.377	0.020
5	MU1_S_60	0.439	0.027
6	MU1_S_75	0.280	0.032
Maximum		0.500	0.045
Minimum		0.280	0.020
Mean		0.391	0.030
Std. Dev.		0.080	0.009
COV (%)		20.5	29.7

Table 10 - Measured Dimensional Parameters of Rib-to-Floor Beam Weld for MU2

Sl. No.	Sample ID	LOF (in.)	R (in.)
1	MU2_N_F	0.364	0.031
2	MU2_S_F	0.500	0.021
3	MU2_N_30	0.434	0.017
4	MU2_N_60	0.356	0.024
5	MU2_S_60	0.400	0.048
6	MU2_S_70	0.400	0.022
Maximum		0.500	0.048
Minimum		0.356	0.017
Mean		0.409	0.027
Std. Dev.		0.053	0.011
COV (%)		12.9	41.2

Table 11 - Measured Dimensional Parameters of Rib-to-Floor Beam Weld for MU3

Sl. No.	Sample ID	LOF (in.)	R (in.)
1	MU3_N_F	0.238	0.070
2	MU3_S_F_35	0.323	0.105
3	MU3_S_F_58	0.313	0.043
4	MU3_S_F_27	0.319	0.109
5	MU3_0	0.152	0.081
6	MU3_N_60	0.268	0.034
7	MU3_N_75	0.246	0.031
8	MU3_S_10	0.046	0.061
9	MU3_S_75	0.246	0.076
Maximum		0.323	0.109
Minimum		0.046	0.031
Mean		0.239	0.068
Std. Dev.		0.090	0.028
COV (%)		37.633	41.963

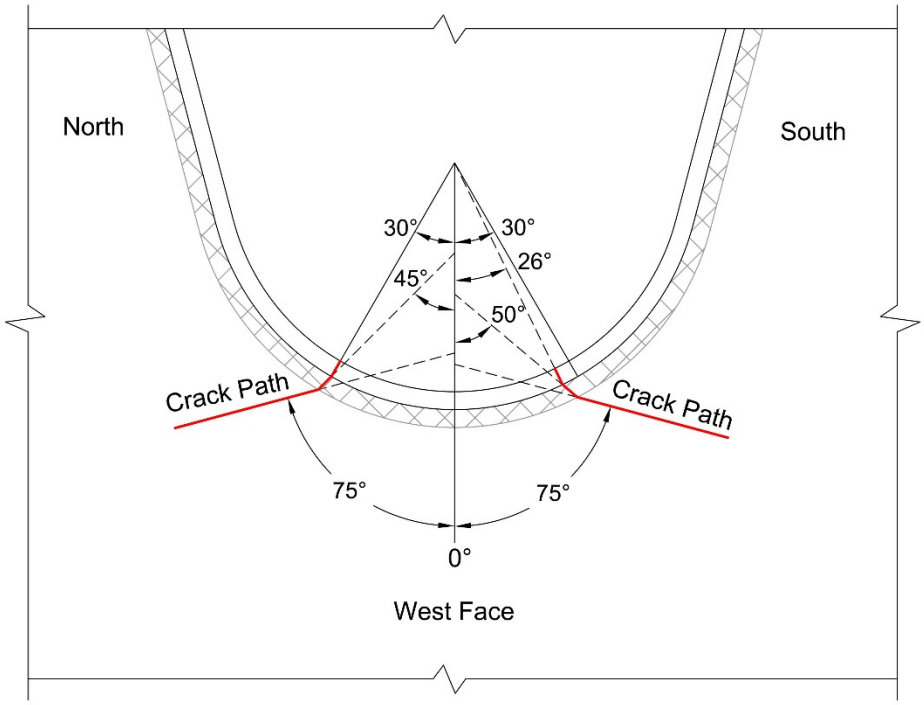

Figure 203. Schematics of cracks in mock-up specimen MU1

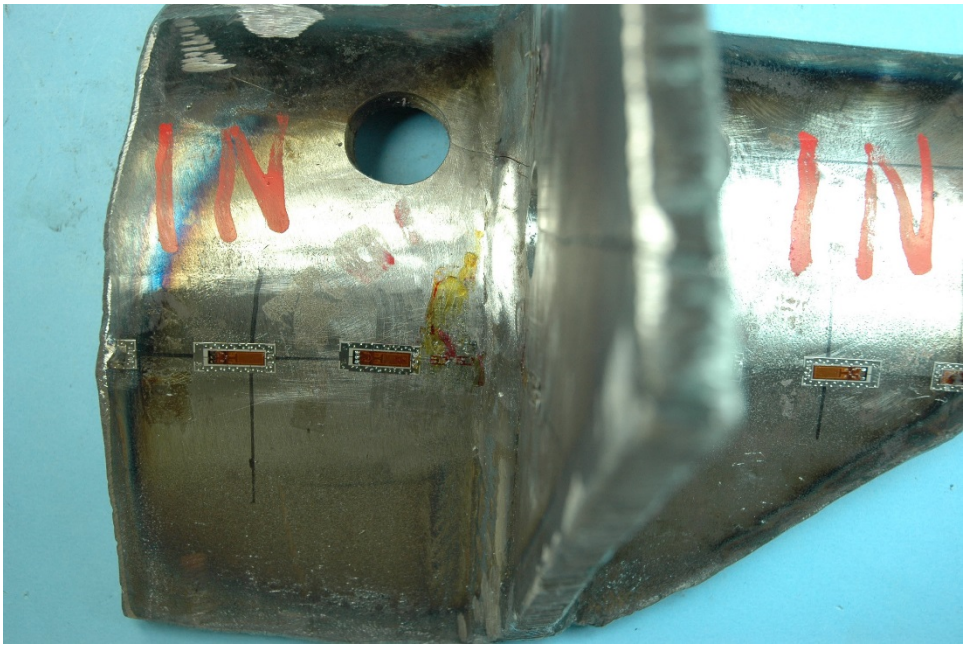

Figure 204. Portion of rib and floor beam containing the north side crack cut out of the mock-up specimen MU1

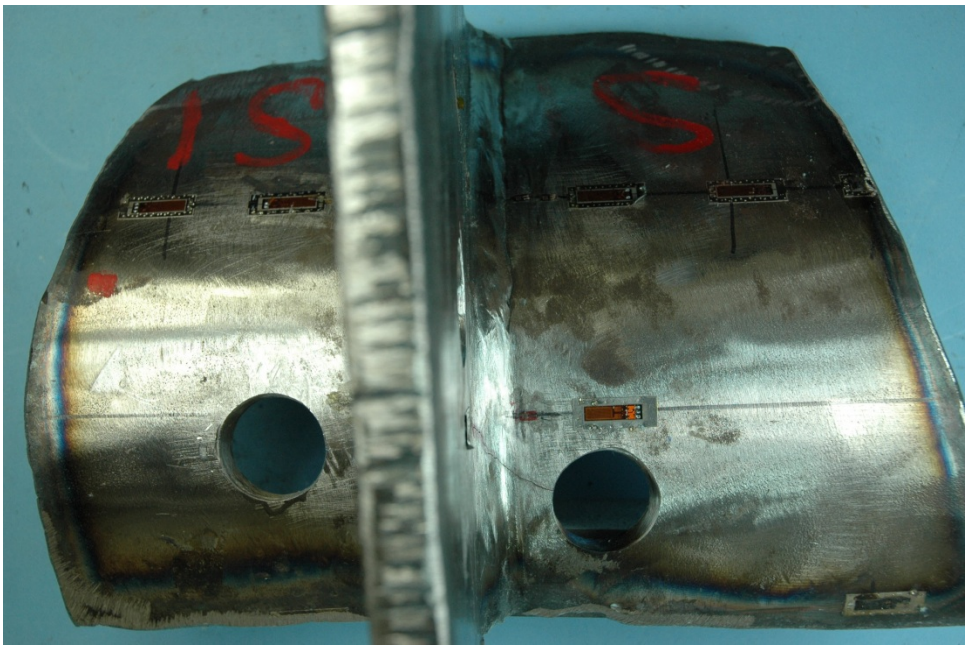

Figure 205. Portion of rib and floor beam containing the south side crack cut out of the mock-up specimen MU1

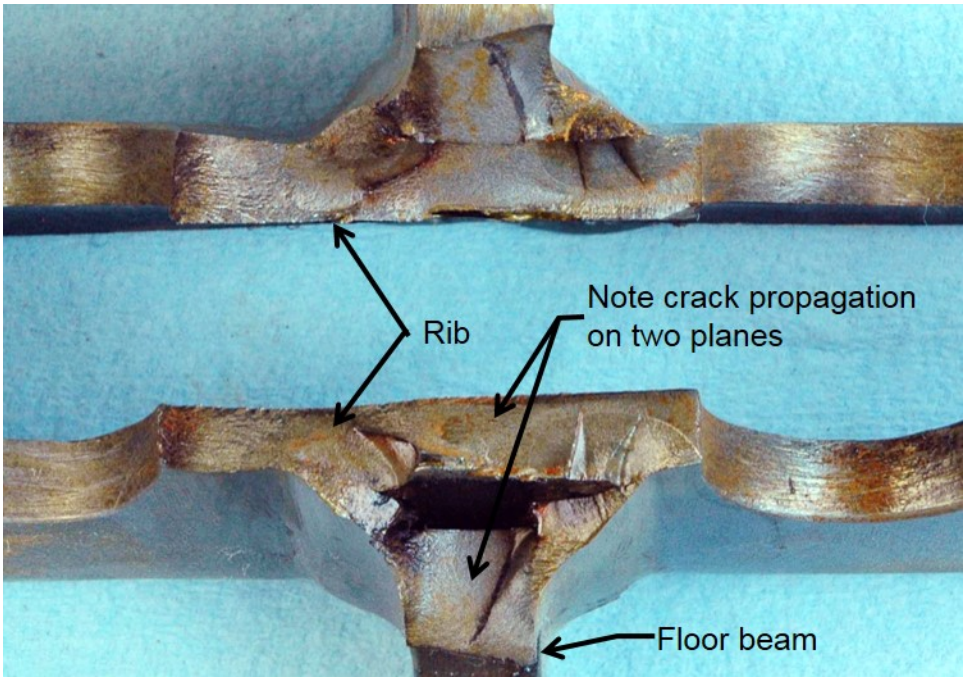

Figure 206. Mating fatigue fracture surfaces for the crack to the north of rib in MU1

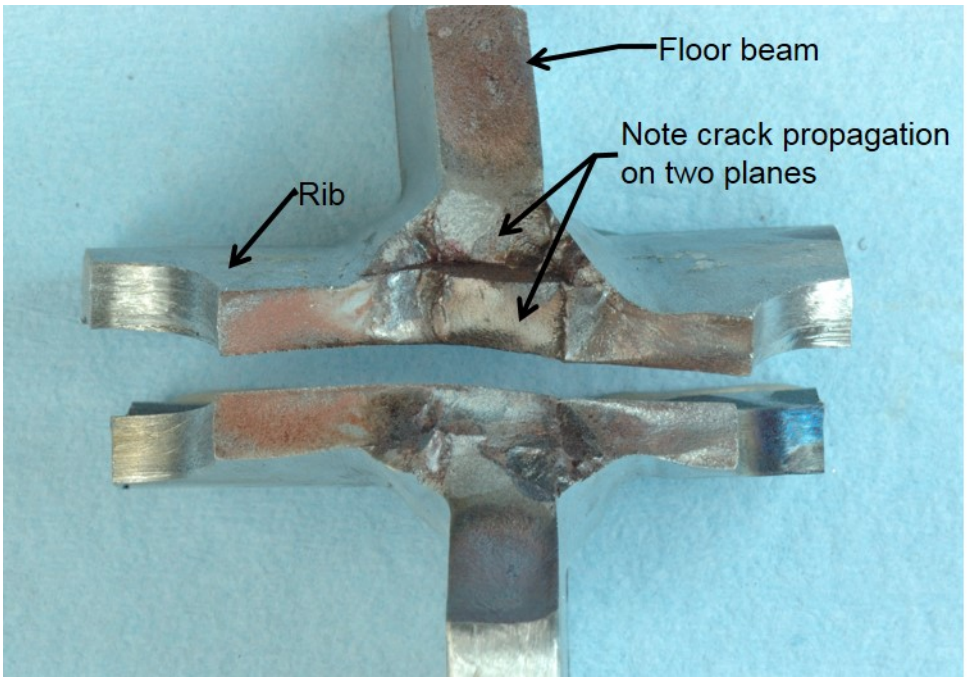

Figure 207. Mating fatigue fracture surfaces for the crack to the south of rib in MU1

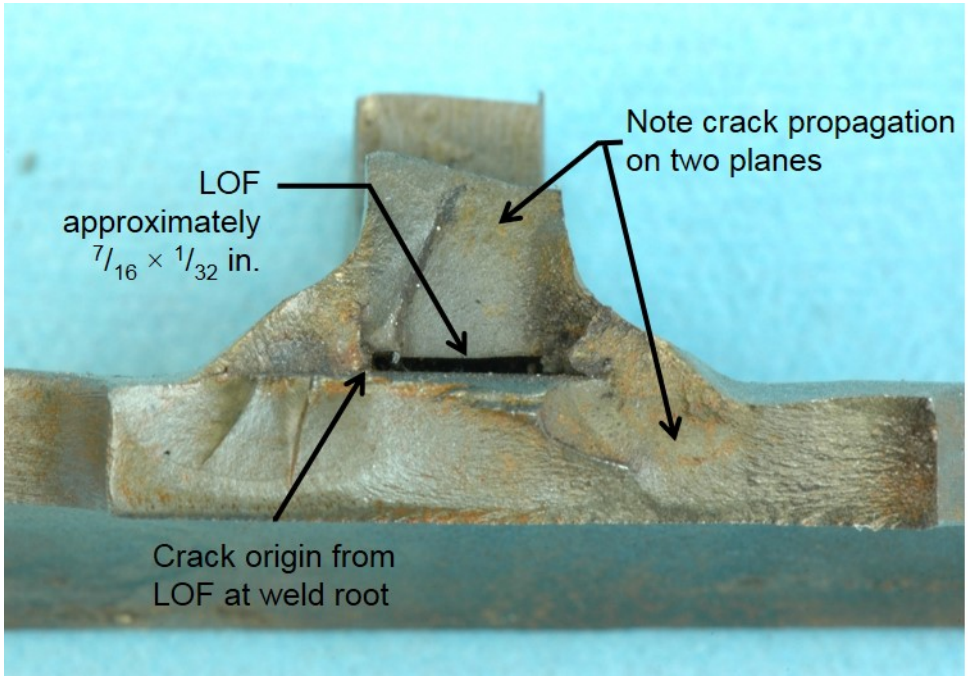

Figure 208. Fracture surface photographed perpendicular to the camera to clarify the LOF — crack to the north of rib

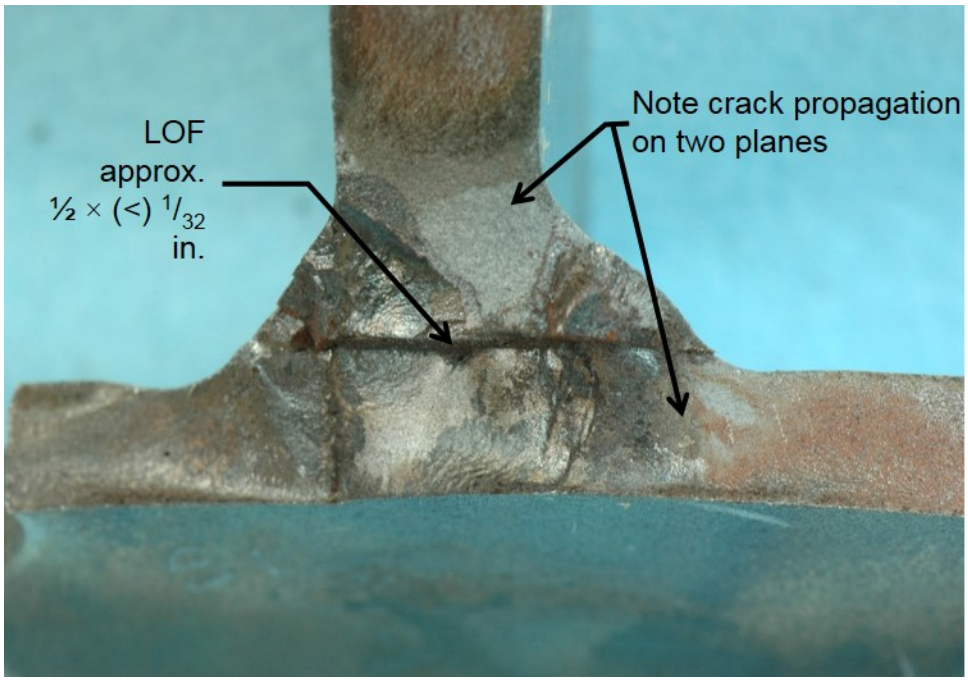

Figure 209. Fracture surface photographed perpendicular to the camera to clarify the LOF — crack to the south of rib

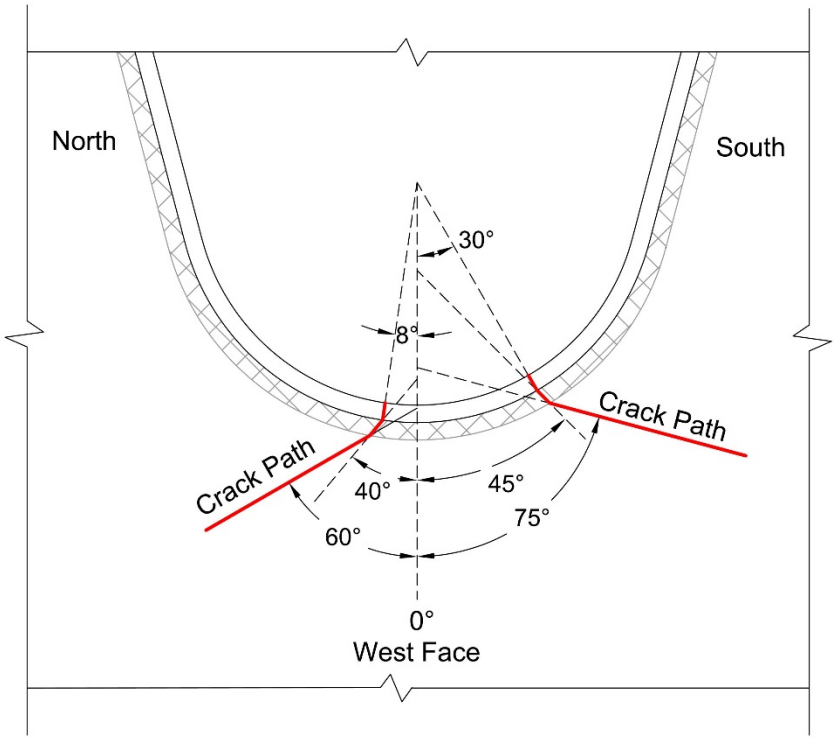

Figure 210. Schematics of cracks in mock-up specimen MU2

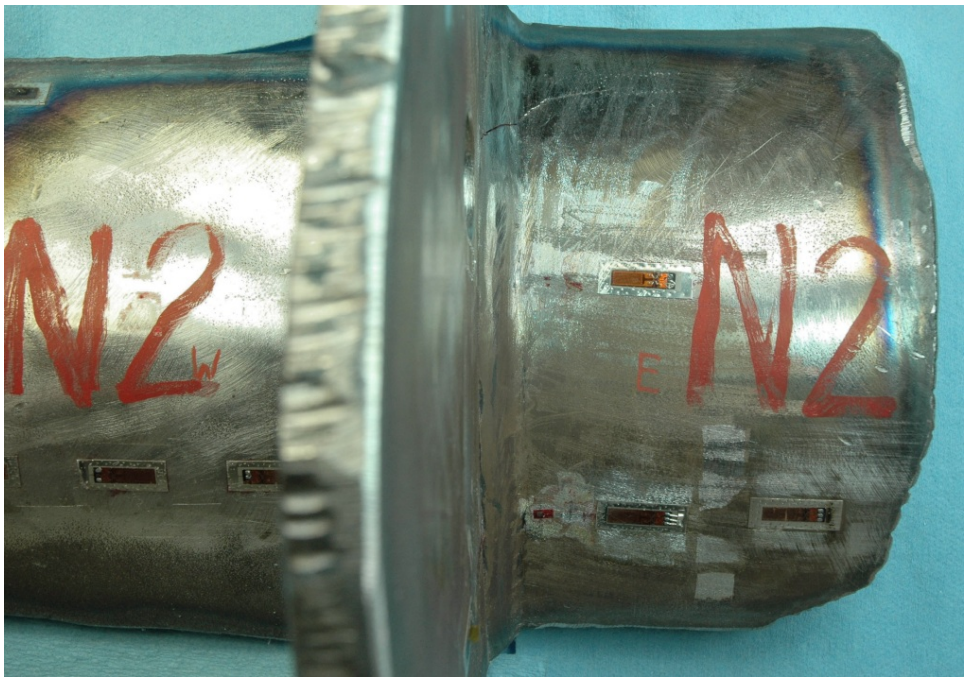

Figure 211. Portion of rib and floor beam containing the north side crack cut out of the mock-up specimen MU2

Figure 212. Portion of rib and floor beam containing the south side crack cut out of the mock-up specimen MU2

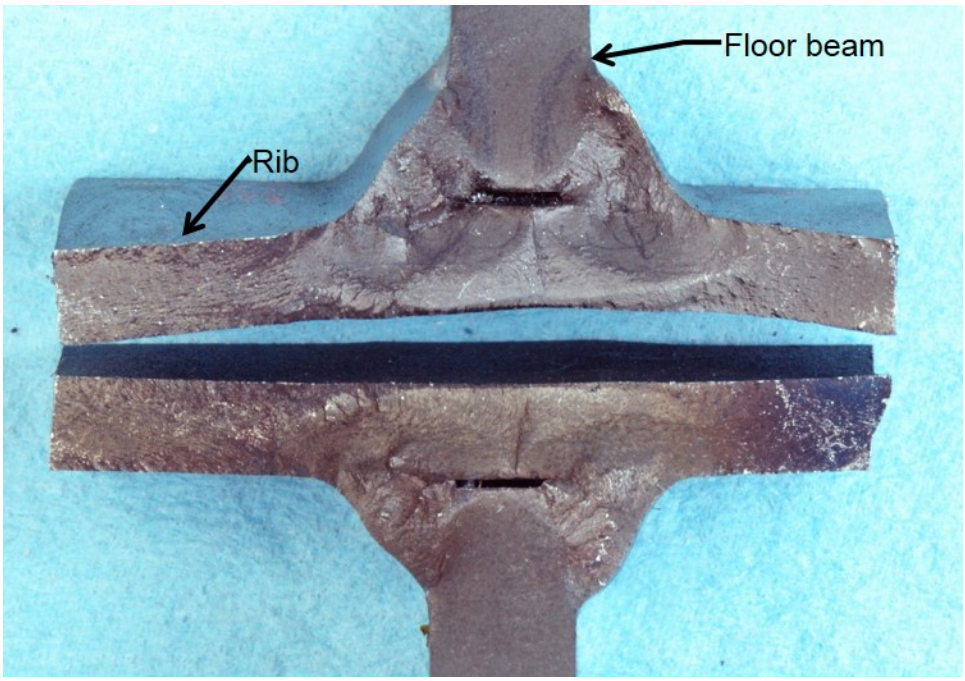

Figure 213. Mating fatigue fracture surfaces for the crack to the north of rib in MU2

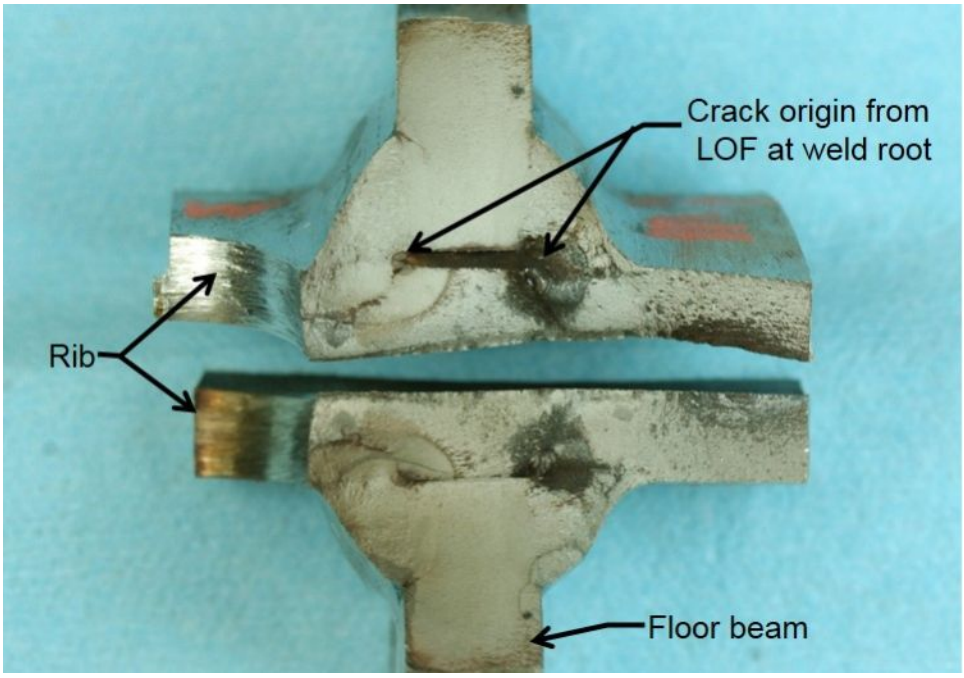

Figure 214. Mating fatigue fracture surfaces for the crack to the south of rib in MU2

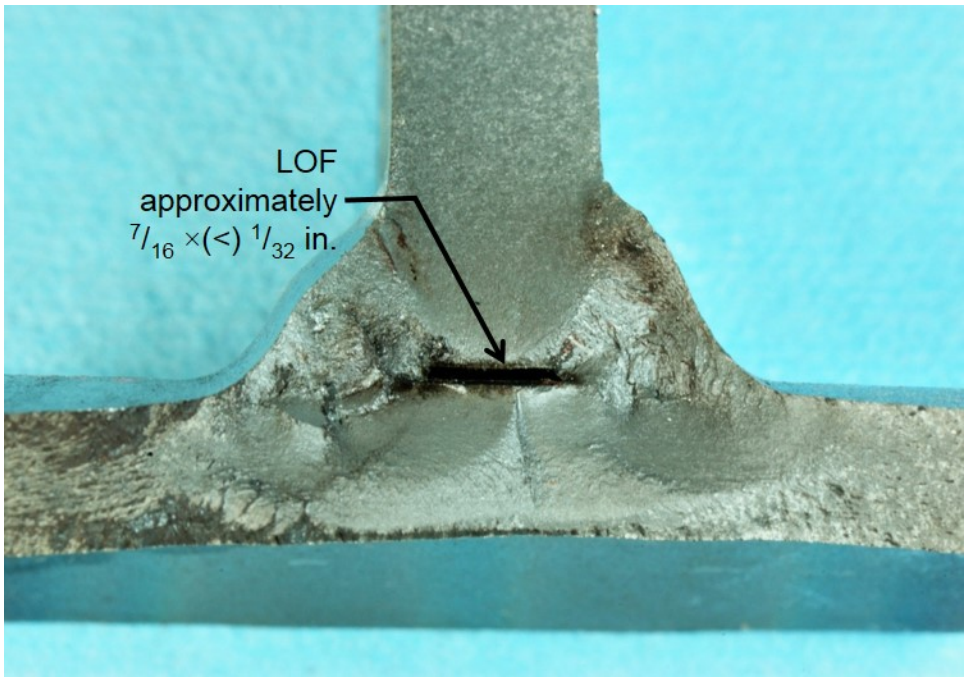

Figure 215. Fracture surface photographed perpendicular to the camera to clarify the LOF — crack to the north of rib in MU2

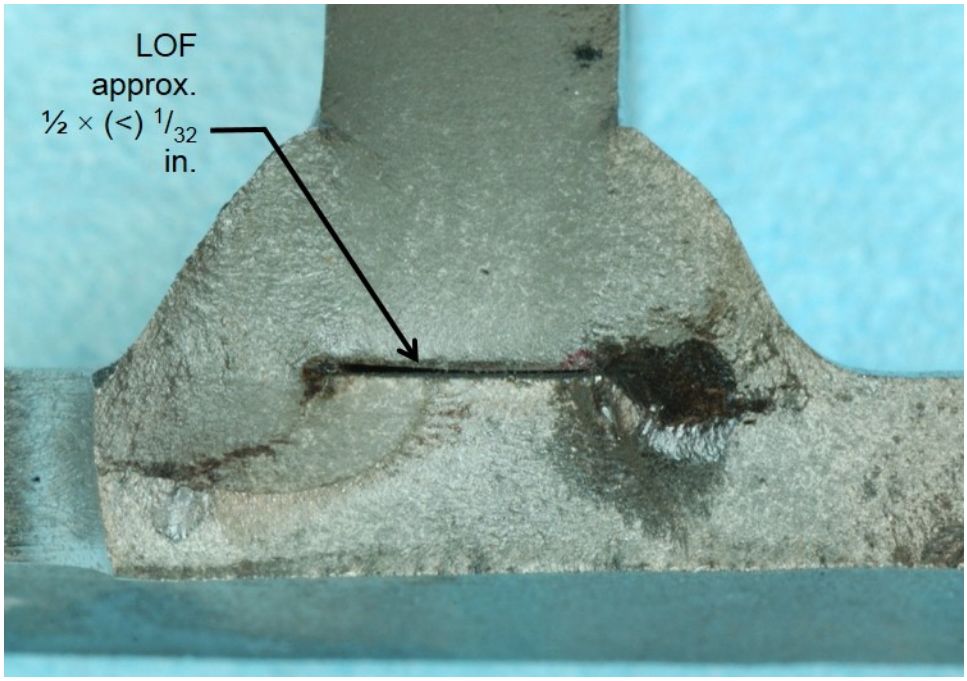

Figure 216. Fracture surface photographed perpendicular to the camera to clarify the LOF — crack to the south of rib in MU2

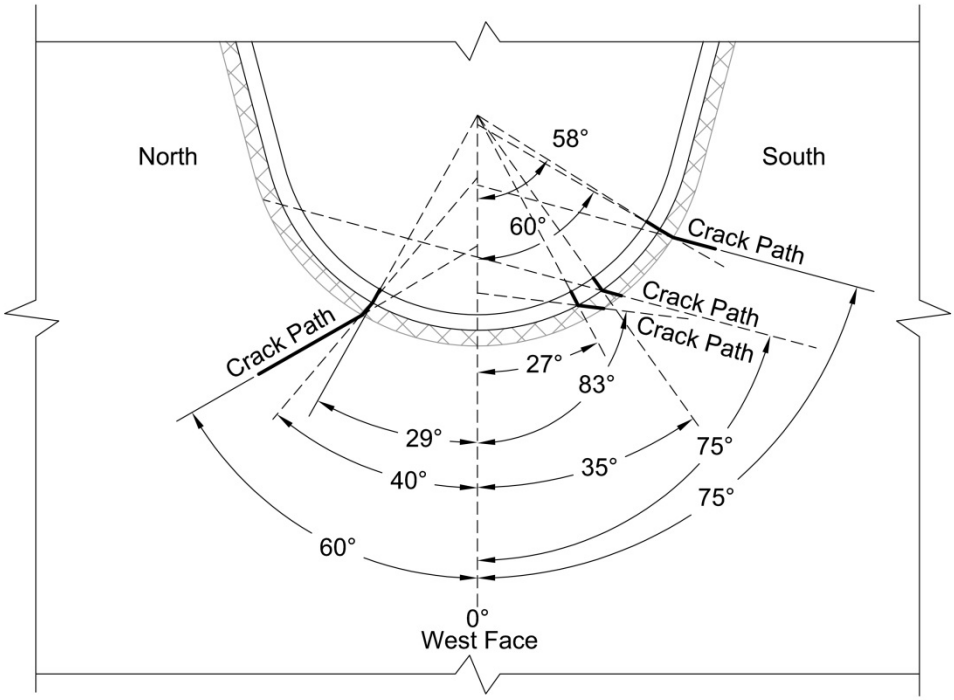

Figure 217. Schematics of cracks in mock-up specimen MU3

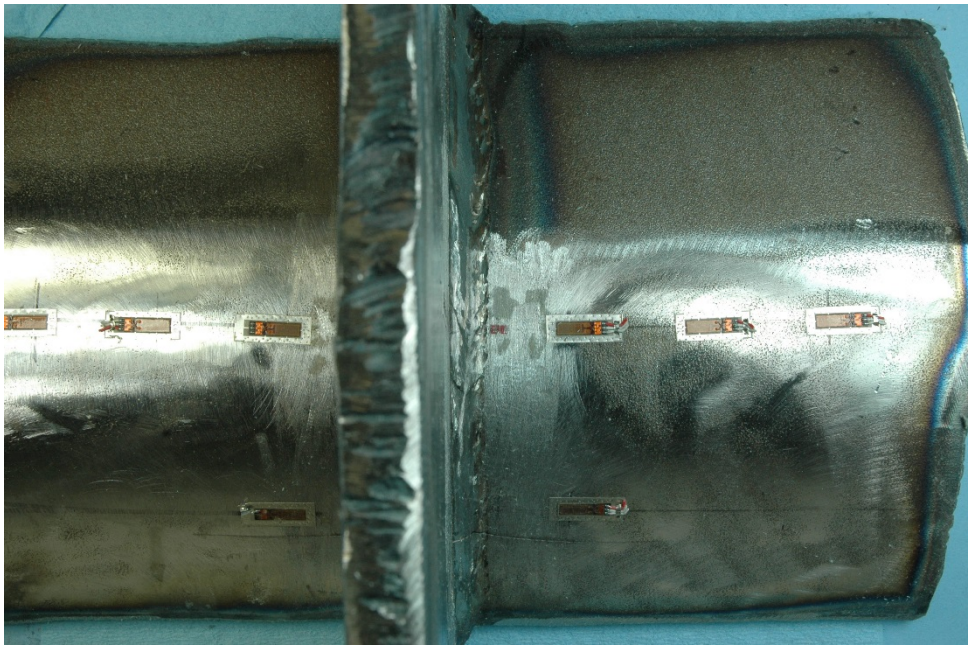

Figure 218. Portion of rib and floor beam containing the north side crack cut out of the mock-up specimen MU3

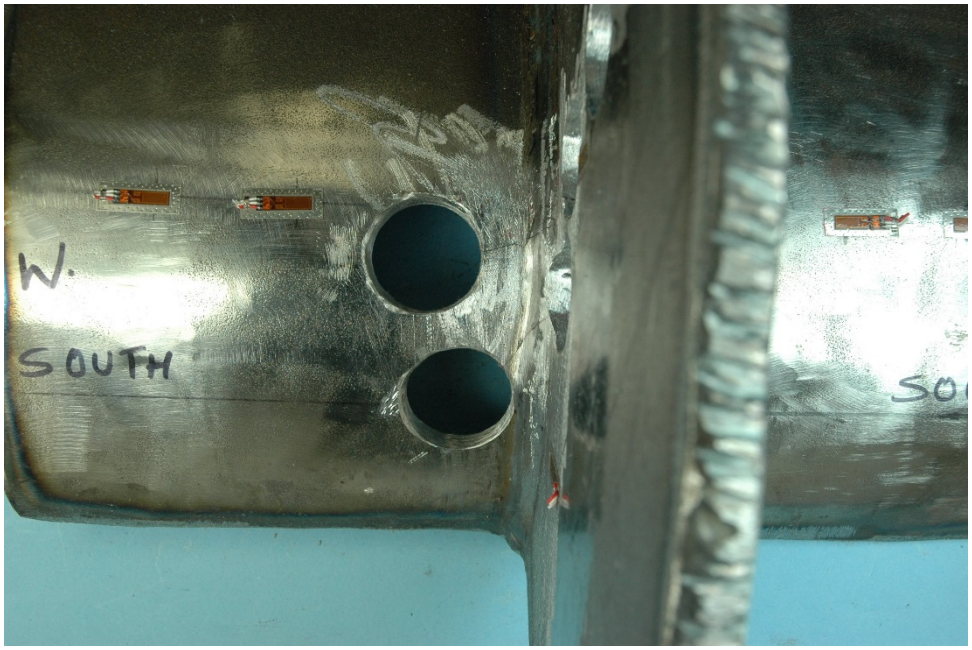

Figure 219. Portion of rib and floor beam containing the south side crack cut out of the mock-up specimen MU3

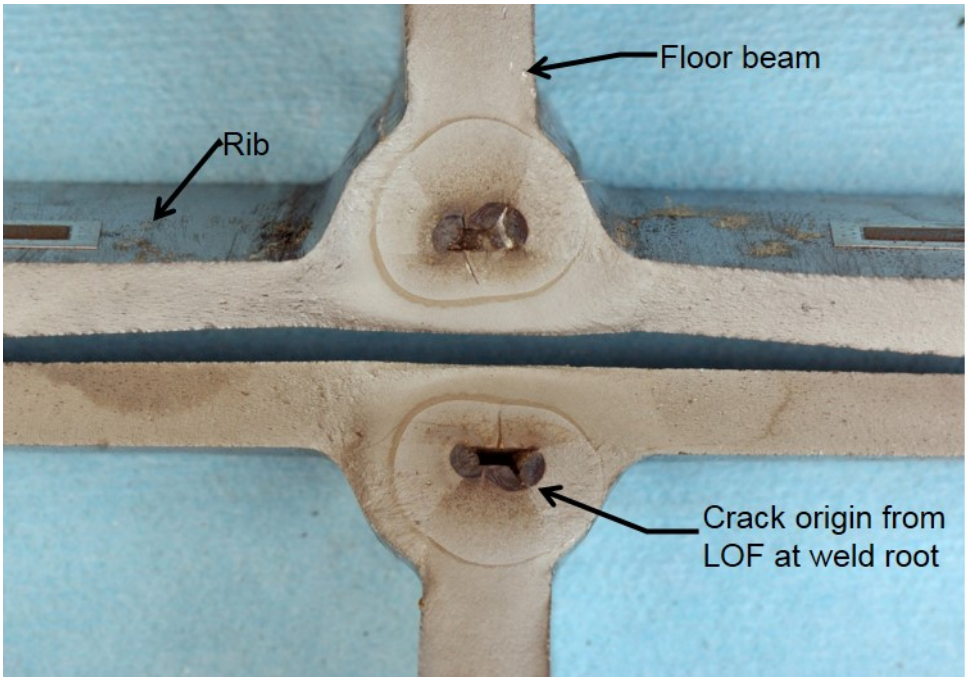

Figure 220. Mating fatigue fracture surfaces for the crack to the north of rib in MU3

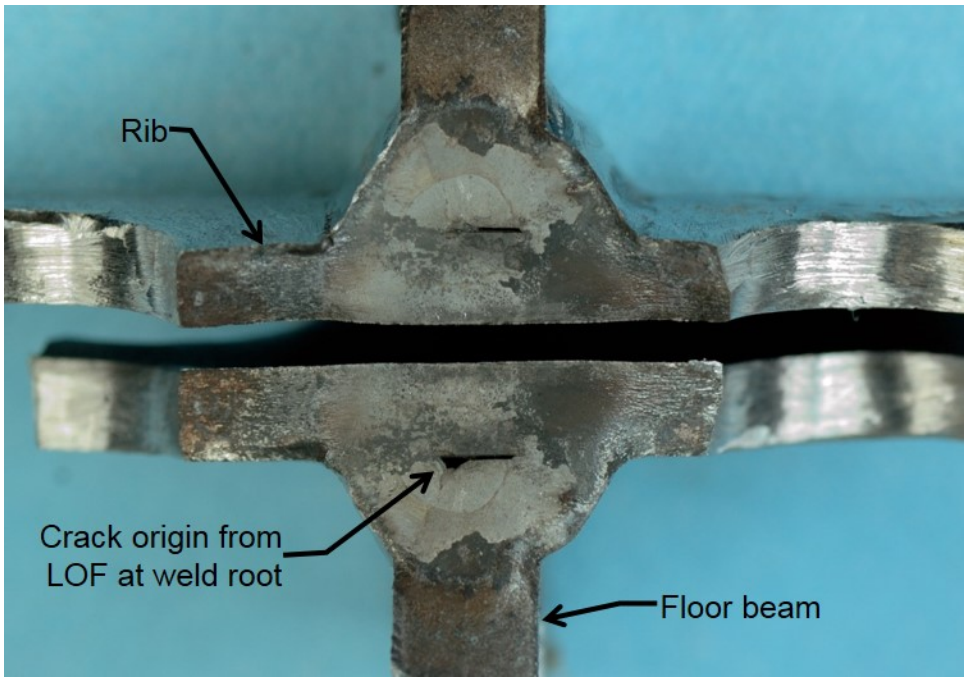

Figure 221. Mating fatigue fracture surfaces for the crack to the south of rib at 55 degrees from rib soffit in MU3

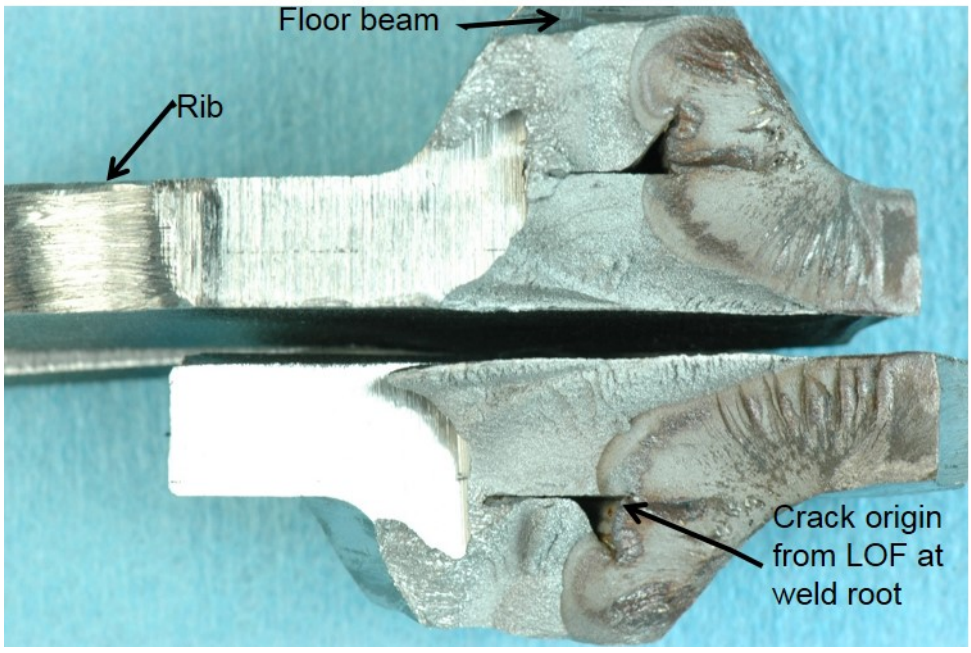

Figure 222. Mating fatigue fracture surfaces for the crack to the south of rib at 35 degrees from rib soffit in MU3

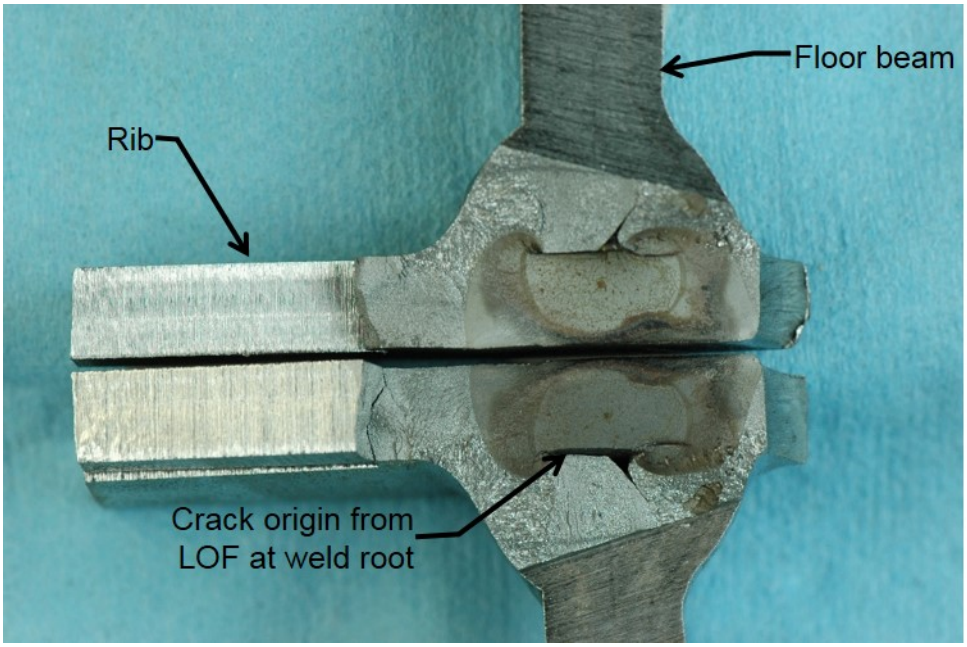

Figure 223. Mating fatigue fracture surfaces for the crack to the south of rib at 27 degrees from rib soffit in MU3

Figure 224. View of fracture surface to the south at about 35 degrees from the rib soffit in MU3 showing the deviation of fracture plane through the weld

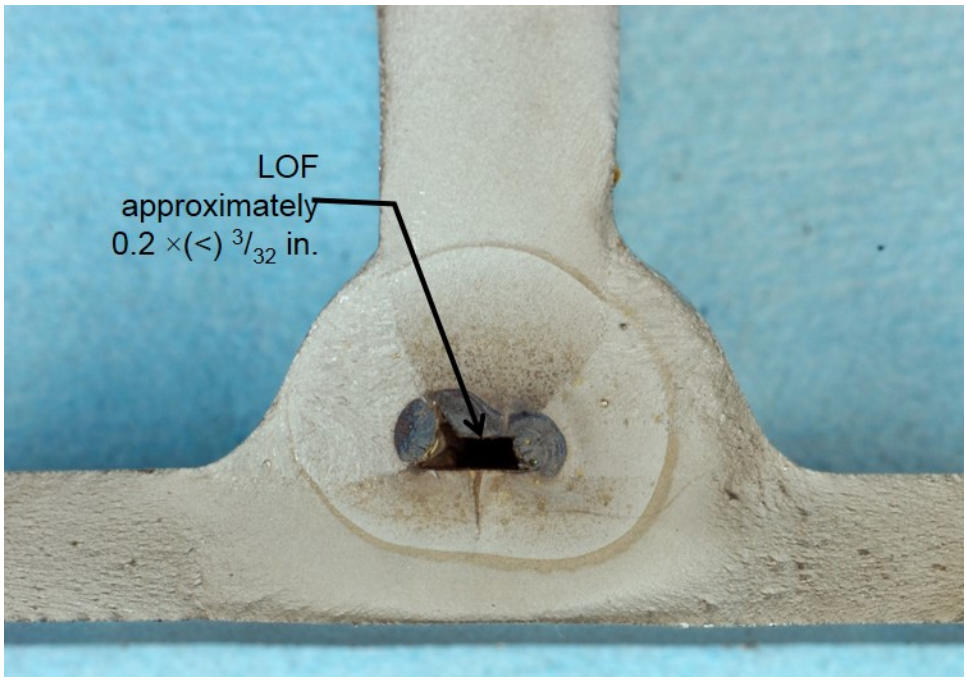

Figure 225. Fracture surface photographed perpendicular to the camera to clarify the LOF — crack to the north of rib in MU3

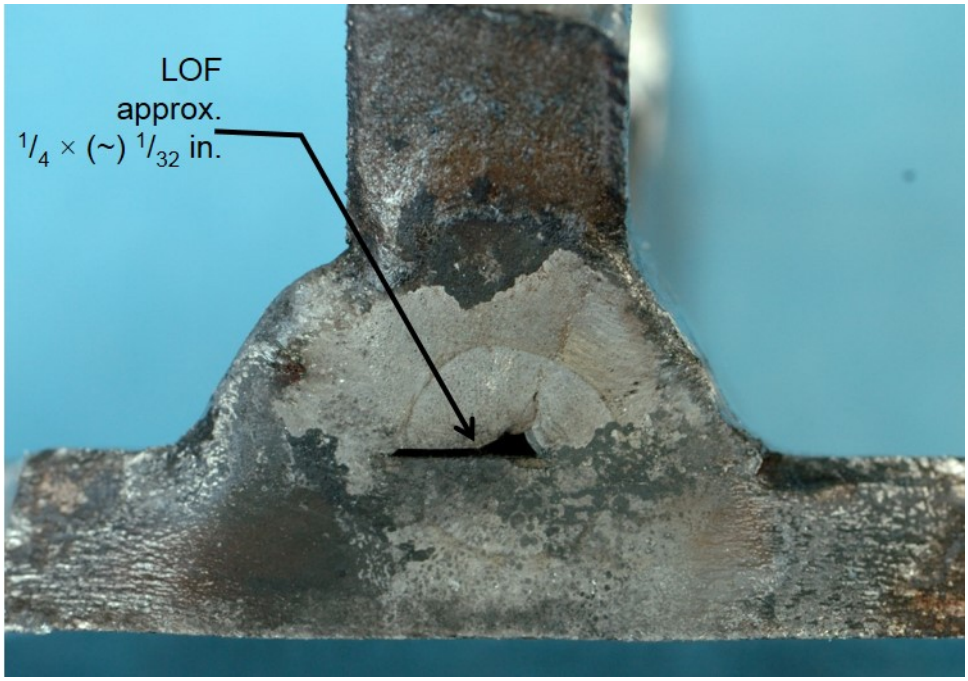

Figure 226. Fracture surface photographed perpendicular to the camera to clarify the LOF — crack to the south of rib in MU3 at 55 degrees from the rib soffit

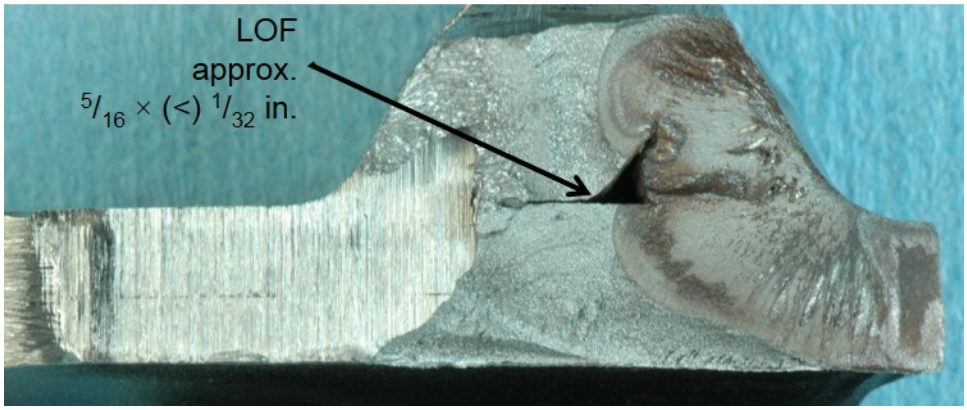

Figure 227. Fracture surface photographed perpendicular to the camera to clarify the LOF — crack to the south of rib in MU3 at 35 degrees from the rib soffit

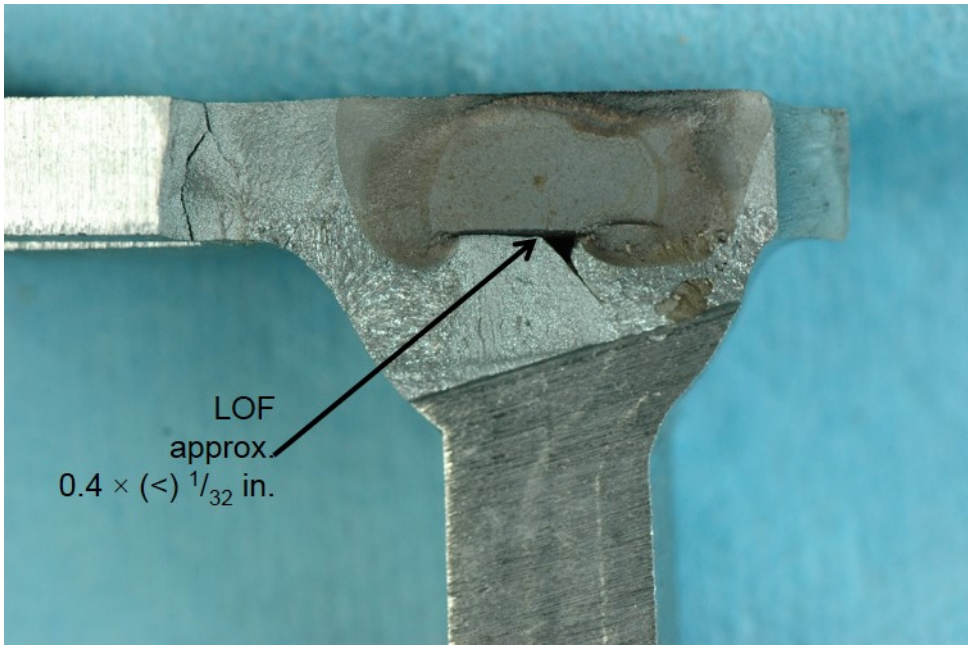

Figure 228. Fracture surface photographed perpendicular to the camera to clarify the LOF — crack to the south of rib in MU3 at 35 degrees from the rib soffit

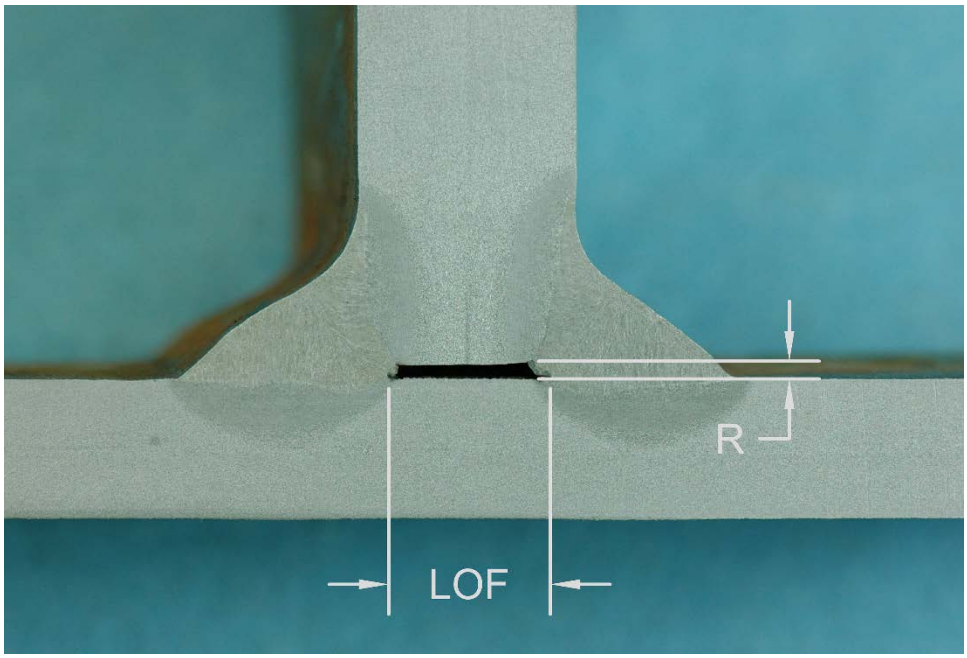

Figure 229. Identification of parameters for rib-to-floor beam weld

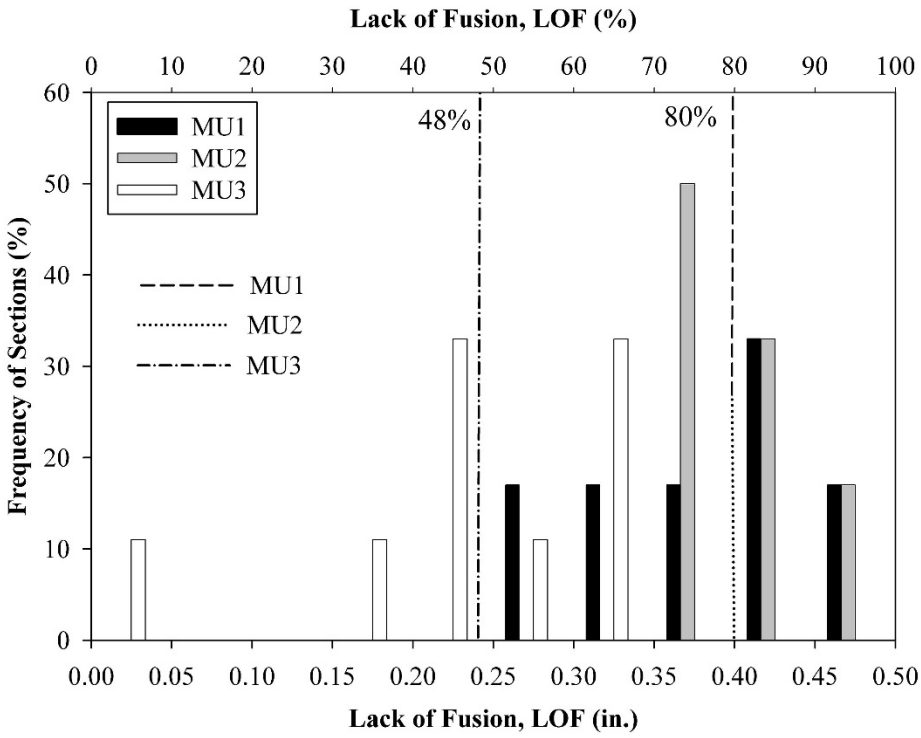

Figure 230. Distribution of LOF for rib-to-floor beam weld

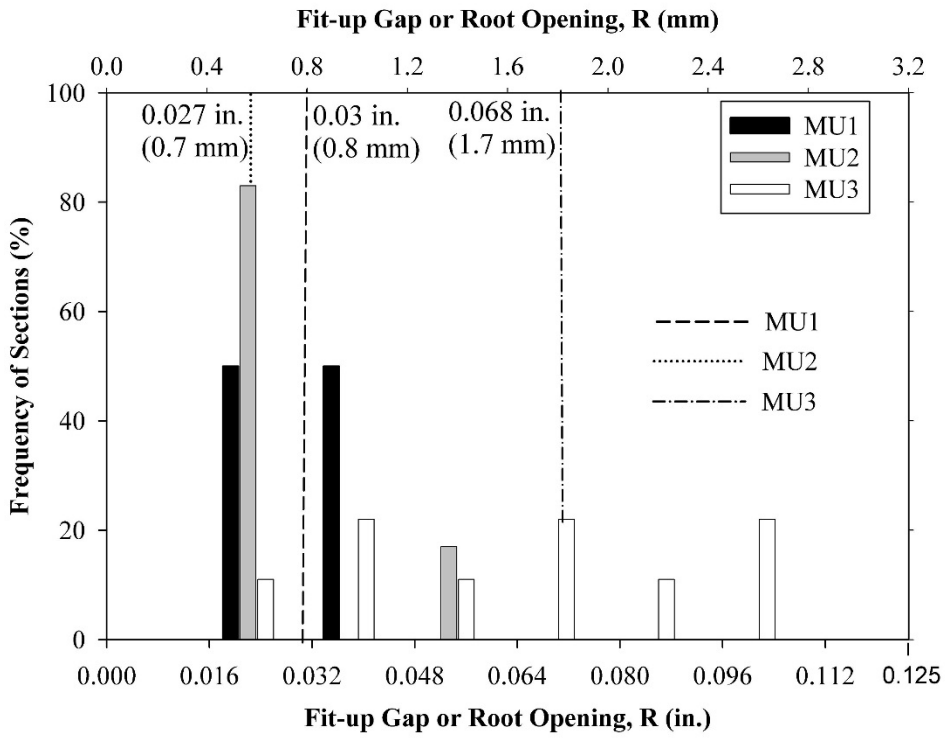

Figure 231. Distribution of R for rib-to-floor beam weld

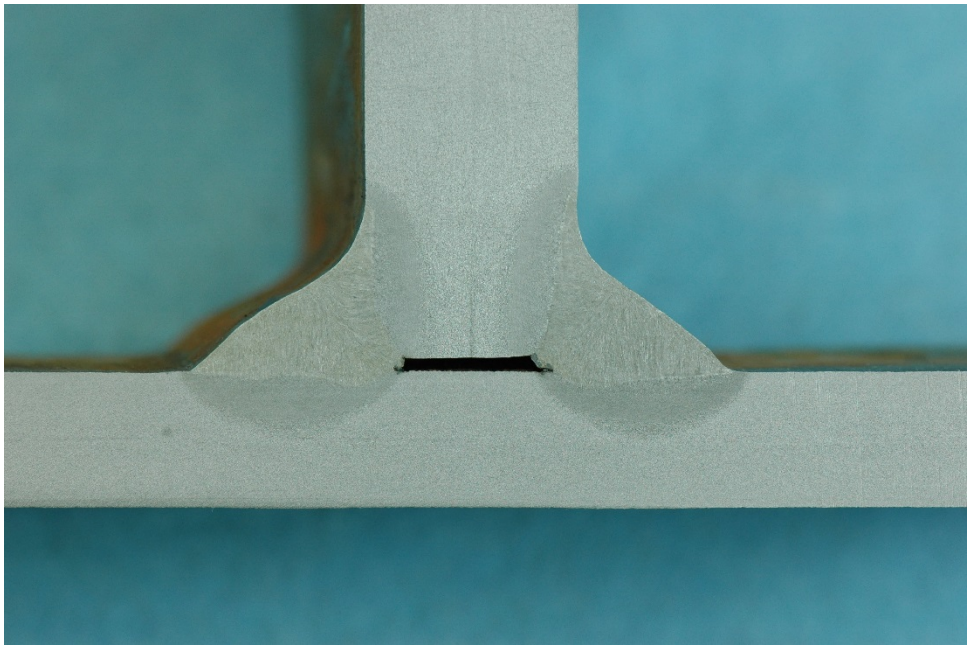

Figure 232. A typical macro-etched section of rib-to-floor beam weld in MU1

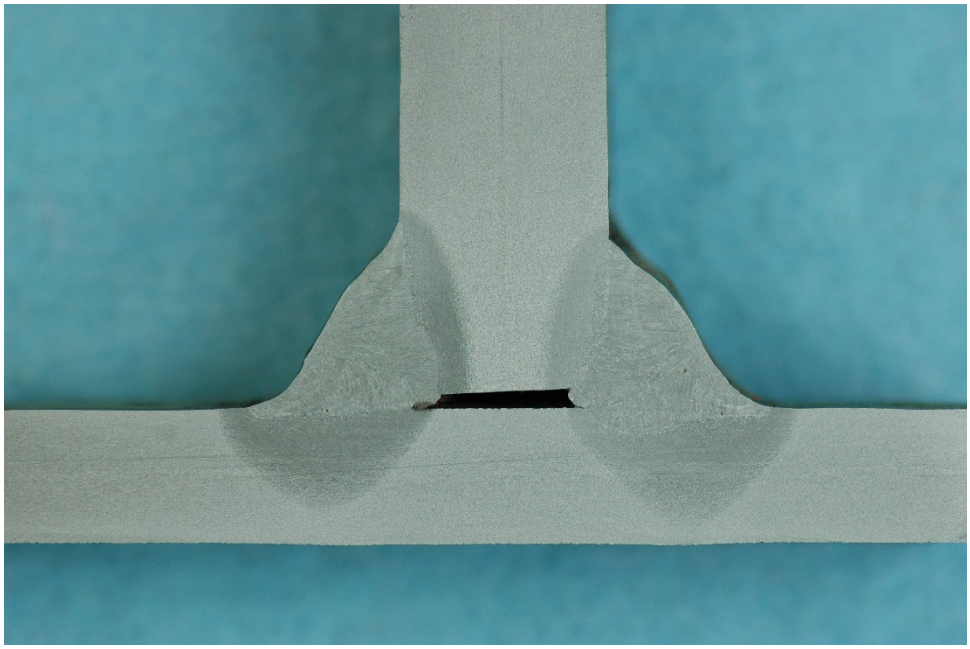

Figure 233. A typical macro-etched section of rib-to-floor beam weld in MU2

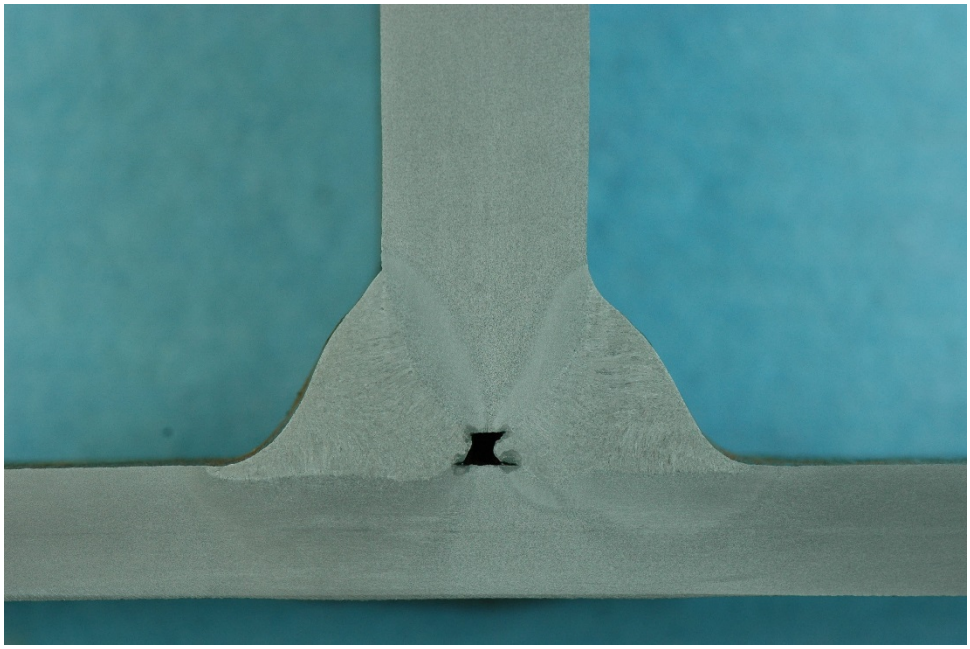

Figure 234. A typical macro-etched section of rib-to-floor beam weld in MU3

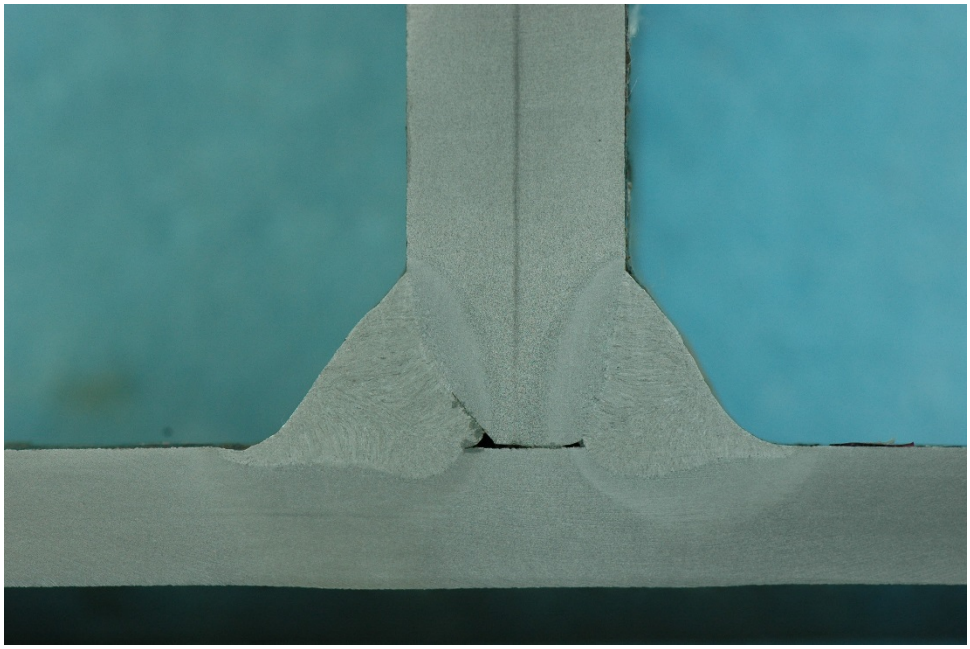

Figure 235. Macro-etched section MU3_N_60

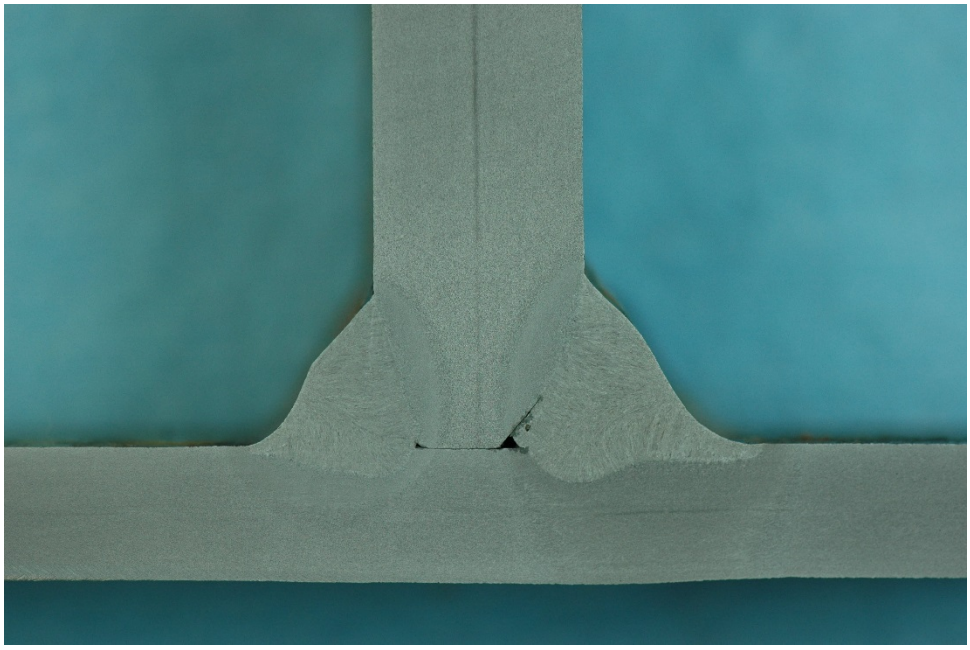

Figure 236. Macro-etched section MU3_N_75